Strain Engineering of InGaN/GaN Nanopillars for Optoelectronic Applications

by

Chu-Hsiang Teng

A dissertation submitted in partial fulfillment
of the requirements for the degree of
Doctor of Philosophy
(Electrical Engineering)
in the University of Michigan
2016

Doctoral Committee:

Associate Professor Pei-Cheng Ku, Co-chair
Associate Professor Hui Deng, Co-chair
Professor Joanna Millunchick
Professor Euisik Yoon

To my family.

Acknowledgements

I would like to thank my research advisor Prof. Pei-Cheng Ku for giving me the opportunity to pursue my PhD degree five years ago and his guidance and support throughout these years. He taught me the right way to conduct research and to think critically. He always tried to push me out of my comfort zone. It made me grow and learn. We had countless discussions and sometimes argument. In the end, I believe we have achieved a lot, and what I learned during my PhD career is going to be my valuable asset for my future career.

I also want to thank the faculty members I worked with. I thank Prof. Hui Deng for helping me scrutinizing my research results and providing valuable insight. I also thank her for providing the resources on optical measurements. I also want to thank Prof. Euisik Yoon and Prof. Joanna Millunchick for the collaboration opportunities and being on the committee board providing valuable suggestions.

In addition, I am also grateful to my co-workers. I would like to thank people in my group, Luke Lee, Michael Kuo, Brandon Demory, and Chih-Wei Chien, for their help and support. Especially I thank the senior students, Luke Lee and Michael Kuo, for helping me get on my feet in my early days. Furthermore, I appreciate the help from our collaborators: Lei Zhang, Tyler Hill, Adam Katcher, Nick Tsai, Yu-Hsun Chou, and

Lifan Yan. I would like to give special thanks to Lei Zhang for his important fundamental work on our InGaN QDs and his efforts in optical measurements. Besides, I also want to give special thanks to Che-Hung Liu and Cheng Zhang for their company during my PhD career.

Finally, I want to thank my parents and my girlfriend, Hsin-Ting Yeh. It is their constant support and trust that allowed me to pursue knowledge abroad and made me get through all these tough times.

Table of Contents

List of Figures

List of Tables

List of Abbreviations

LED	light emitting diode
LD	laser diode
QW	quantum well
MQW	multiple quantum well
EQE	external quantum efficiency
IQE	internal quantum efficiency
uid-GaN	unintentionally dopped GaN
RGB	red, green, and blue
MOCVD	metal-organic chemical vapor deposition
QD	quantum dot
QCSE	quantum confined Stark effect
MV	megavolt
KOH	potassium hydroxide
ICP	inductively coupled plasma
MHz	megaherz
CCD	charged coupled device
SEM	scanning electron microscope
APD	avalanche photo diode

TC	time correlator
PL	photoluminescence
YL	yellow band luminescence
MBE	molecular beam epitaxy
PECVD	plasma-enhanced chemical vapor deposition
SOG	spin-on-glass
FWHM	full width at half maximum
EL	electroluminescence
DLP	degree of linear polarization
PR	photoresist
PMMA	polymethyl methacrylat
RIE	reactive ion etching
μ-PL	micro-photoluminescence
HBT	Hanbury Brown-Twiss
TRPL	time-resolved photoluminescence
QKD	quantum key distribution
APT	Atom probe tomogaphy
RA	random alloy
WWF	well-width fluctuation

DF diameter fluctuation

ML monolayer

Abstract

The indium gallium nitride (InGaN)/gallium nitride (GaN) material system is critical for optoelectronic applications in LEDs and lasers because it has direct band gap and large oscillator strength. In addition, the bandgap can be tuned by the alloy composition, and the emission wavelength covers the entire visible spectrum and extends into ultraviolet and near infrared regions. Due to the large lattice mismatch between InGaN and GaN, a large built-in strain exists in the InGaN quantum well layer and induces a piezoelectric field across the quantum well. The piezoelectric field leads to the quantum-confined Stark effect, which red-shifts the emission wavelength and degrades the recombination efficiency. It is known that nanostructures have large surface-to-volume ratio and can help relax strain via free surfaces. In this work, we present top-down InGaN/GaN nanostructures as an effective way to manipulate the strain and serve as a building block to engineer the strain effect for novel optoelectronic functionalities. First, we demonstrate that the emission colors from top-down nanopillars can be tuned from blue to red by changing the nanopillar diameter. The wavelength shift is well-described by an analytical model. We also demonstrate electrical nanoLED devices based on the nanopillars. It provides a simple solution to monolithic integration of multiple color pixels on a single chip. Second, we discuss the

benefits of strain engineering for quantum light source applications. We focus on the intrinsic control of photon polarization states via asymmetric strain. Experimental data is provided to show that pre-defined polarization states can be achieved by engineering quantum dot geometry and strain. Single photon emission with orthogonal polarization states and high degree of linear polarization are recorded. It suggests the potential of top-down InGaN quantum dots for quantum information applications. Finally, the non-ideal factors, in our top-down quantum dots, including random alloy fluctuation and well-width fluctuation, are discussed. These effects modify the potential landscape and impose a fundamental limit to the quantum dot inhomogeneity, especially for ternary alloys. A methodology to model random alloy distribution and random well-width fluctuation is developed. The modeling results suggest that the strain-relaxation-induced potential is the dominant effect of lateral confinement even with the presence of random indium fluctuation and well-width fluctuation. The results are also compared to experimental data and show very good agreement.

Chapter 1

Introduction

Indium gallium nitride (InGaN) compound semiconductors exhibit a large energy bandgap and have important applications in optoelectronic and electronic devices because of their superb optical and electrical properties. In optoelectronics, because of the direct bandgap and efficient electron-hole recombination, they are extensively used for light emitting devices in the ultraviolet and visible wavelength range. In electronics, the large bandgap, high heat capacity, high thermal conductivity, and robust material properties make them suitable for high power applications. Heterostructures comprising of InGaN and GaN typically exhibit a large strain due to lattice mismatch. The strain

has a huge impact on both electronic and optical properties of the InGaN based devices. This thesis focuses on studying the strain in InGaN/GaN light emitting structures, utilizing top-down nanostructures as an effective way to manipulate strain, and create new device functionalities, including monolithic multi-color integration and emission polarization control. In this Chapter, we will review the important technology development of relevant InGaN light emitting devices and introduce the physics underlying the strain and piezoelectric effects in InGaN/GaN heterostructures, which plays a key role throughout the thesis.

1.1 InGaN/GaN for Optoelectronic Applications

Group III-nitride semiconductors including AlN, GaN, InN and their alloys have attracted a lot of attentions in the past few decades, especially since the breakthrough of GaN blue light emitting diodes (LEDs) in 1994 [1]. III-nitride semiconductors have been widely used in optoelectronic devices because: 1) they are chemically stable and thus provide good device reliability and long lifetime; 2) they have direct bandgap and strong oscillator strength, which enables high photon emission efficiency; 3) the combination of AlN-GaN-InN covers a huge wavelength range, from ultraviolet, through visible, to infrared, and, therefore, is a great platform for various sorts of optoelectronic light emitting devices, including LEDs and laser diodes (LDs) [2,3]. The

lattice constant, band gap, and the corresponding wavelength of AlN, GaN, and InN is summarized in Table 1-1. III-nitride-based optoelectronic devices have found widespread of applications including lighting, data storage, communications, displays, biological assays, and quantum information technologies.

Table 1-1: Lattice constant, band gap, and the corresponding wavelength of wurtzite AlN, GaN, and InN [4,5,6,7,8].

	AlN	GaN	InN
Lattice constant, a (Å)	3.110	3.190	3.544
Lattice constant, c (Å)	4.980	5.189	5.718
Bandgap (eV)	6.28	3.44	0.7
Wavelength (nm)	197.45	364.71	1771.43

1.1.1 Classical Light Sources

Figure 1-1(a) shows a typical LED device structure. The active region consists of InGaN multiple quantum wells (MQWs) sandwiched between GaN quantum barriers. Because of the smaller bandgap of InGaN compared to GaN, the QW structure confines carriers and enhances radiative recombination. The GaN p-n junction allows high current density into the MQWs for high light output intensity. An example of MQW

band structure is illustrated in Figure 1-1(b).

The capability of generating visible light makes III-nitride LEDs very valuable for commercial applications. In order to make better products, higher output power, higher efficiency (EQE and IQE), and a wider range of emission colors have become the main focuses of LED research. A lot of different techniques have been reported, aiming to improve the output power and efficiency. For example, surface texturing, substrate lift-off, and patterned substrates have been shown to result in higher light extraction efficiency [9,10,11]. It is also possible to obtain more directional emission by designing special photonic structures [12]. Different epitaxial structures have also been proposed to improve the current injection efficiency and carrier recombination efficiency, such as the introduction of electron blocking layer [13]. Growing QWs on different crystal facets is also a burgeoning area recently because it can potentially eliminate the quantum-confined Stark effect in conventional c-plane QWs [14,15].

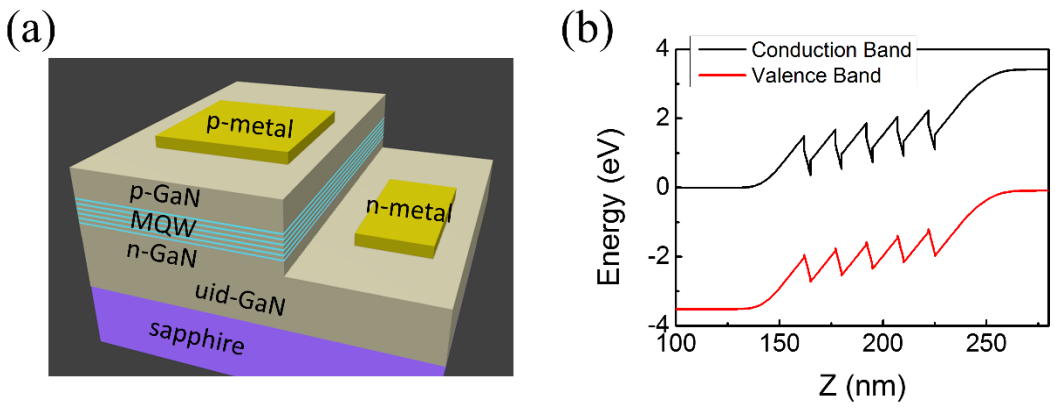

Figure 1-1. (a) A typical LED device structure. (b) Band structure of a p-i-n LED epi-

structure that contains five InGaN QWs.

A lot of efforts have been made to push the limit of LED emission wavelength. Although in theory the InGaN alloy can emit wavelength covering the entire visible spectrum, the progress of yellow- and red-emitting LEDs has been hindered by the difficulties in epitaxial growth as the lattice mismatch increases with the indium composition, as shown in Table 1-1. Therefore, commercial yellow and red LEDs today are still dominantly based on III-phosphide materials. Because it is difficult to grow III-nitride and III-phosphide materials on the same substrate, monolithic integration of R-G-B emitters on the same chip has been challenging. Up to date, the integration heavily relies on pick-and-place method [16], which is usually more costly and undesirable for mass production. For easier integration, red-emitting InGaN-based LEDs are necessary to achieve a fully III-nitride-based full color device. Researchers have been advancing the metal-organic chemical vapor deposition (MOCVD) technique, trying to achieve higher indium composition while keeping good epitaxial quality [17]. An alternative is to carry out InGaN epitaxy on nanostructures since nanostructures are known to be able to relax strain and alleviate the lattice mismatch issue. Successful red InGaN LEDs based on nanostructures have been reported by several research groups [18,19,20]. Monolithic integration of multi-color nanostructural III-nitride LEDs is thus expected to be a likely candidate to achieve full-color light-emitting chips.

1.1.2 Non-classical Light Sources

Non-classical light generates output that cannot be described by classical electromagnetics, and the particle nature of photons needs to be considered because it usually involves only few number of photons. Because of the quantum nature of light, non-classical light sources have important applications in quantum cryptography [21], quantum information technologies [22], precision measurements [23], random number generation [24], and so on.

Common non-classical or quantum light sources include single atoms [25], organic molecules [26], material defect centers [27,28], colloidal quantum dots (QDs) [29], and semiconductor epitaxial QDs [30]. The critical feature they all share is the atom-like discretized energy levels. The discretized energy levels make the electron-hole recombination events associated with different energy levels easily distinguishable. Furthermore, the optical selection rule, $\Delta l = \pm 1$ and $\Delta m = \pm 1$, ensures that the two excitons of an excited state to emit two photons in radiative cascade. The aforementioned characteristics allow these non-classical light sources to generate single photon streams.

Among various types of quantum emitters, semiconductor QDs possesses important advantages, such as electrical operation by embedding QDs in a

semiconductor p-n junctions [31], easy integration with photonic structures [32,33,34], potential for on-chip photonic devices [35 , 36], potential to operate at telecommunication wavelengths, and better scalability. III-As QDs are the most studied semiconductor QD system and have been used to demonstrate single photon emission [37], entangled photon pairs [38], and single photon spin qubit [39]. However, due to the small exciton binding energy (1.0 meV in InAs and 4.1 meV in GaAs), III-As QD devices require a cryogenic operating temperature, and, as a result, the applications are limited. On the other hand, III-nitride materials have larger exciton binding energy (27 meV in bulk GaN), making high temperature operations possible [40,41,42].

1.2 Strain and Piezoelectric Field in InGaN/GaN Quantum Well Structures

InGaN MQWs grown on c-plane wurtzite GaN are the most common active layer structure for blue and green LEDs and LDs. According to Table 1-1, the large lattice mismatch between InGaN and GaN generates an in-plane compressive strain, which is defined by the following equation:

$$\varepsilon_{\parallel} = \frac{a_{GaN} - a_{InGaN}}{a_{InGaN}} \quad . \tag{1-1}$$

The perpendicular strain component, $\varepsilon_{\perp}$, can be calculated by the elastic constants c_{13} and c_{33}:

$$\varepsilon_{\perp} = -2\frac{c_{13}}{c_{33}}\varepsilon_{\parallel} \quad . \tag{1-2}$$

The piezoelectric field is then obtained from:

$$P_{piezo} = e_{33}\varepsilon_{\perp} + 2e_{31}\varepsilon_{\parallel} \quad (1\text{-}3)$$

where e_{33} and e_{31} are the piezoelectric constants. Figure 1-2(a) illustrates the compressive strain in InGaN and the piezoelectric field along [0001] axis. The piezoelectric field is typically on the order of MV/cm and can cause hundreds of meV shift in transition energy. Using Equation 1-3 and parameters in Table 1-2, the in-plane strain and the induced piezoelectric field across the QW are calculated and summarized in Figure 1-1 for various indium compositions. The piezoelectric field leads to a large band tilting in the QW band structure, as shown in Figure 1-1(b), and some undesirable consequences to device performance. For example, it results in the quantum-confined Stark effect (QCSE): red-shift of transition energy and degradation of wavefunction overlap integral [43]. Furthermore, it increases the local carrier concentration and enhances carrier overflow [44] and Auger recombination [45].

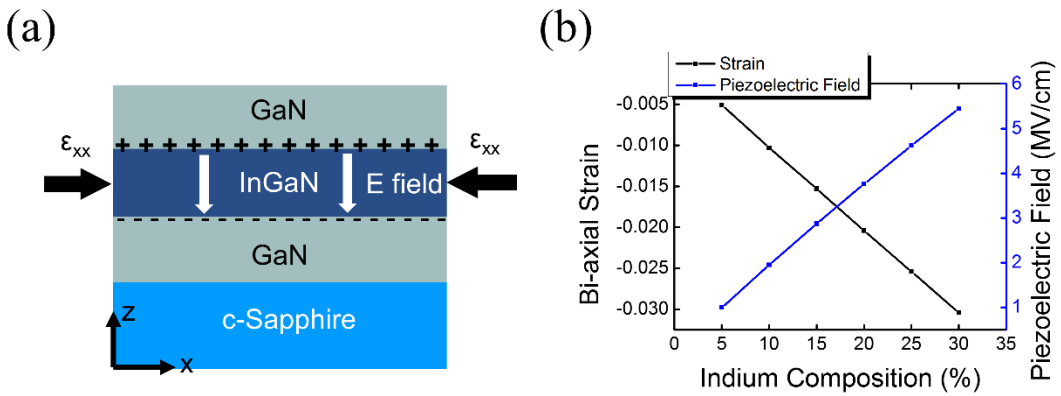

Figure 1-2. (a) Schematic illustration of the compressive strain in InGaN QW, the

corresponding piezoelectric field and piezoelectric charges at the interface. (b) In-plane biaxial strain and piezoelectric field in InGaN QW for various indium composition. The strain is negative because it is compressive strain.

Table 1-2. Important elastic constants and piezoelectric constants of III-nitride materials [46].

	AlN	GaN	InN
C_{13} (N/m^2)	12×10^{11}	10.9×10^{11}	9.4×10^{11}
C_{33} (N/m^2)	39.5×10^{11}	35.5×10^{11}	20×10^{11}
e_{31} (C/m^2)	-0.6	-0.49	-0.57
e_{33} (C/m^2)	1.46	0.73	0.97

1.3 Strain Engineering by Nanostructures

Given the strong modification of band structure due to strain and piezoelectric effect, strain in InGaN can serve as an additional parameter to engineer the optical properties, such as emission wavelength and polarization, if the strain profile can be controlled. It can be achieved by applying a mechanical force but requires external mechanical parts or actuators [47,48,49]. Another way to engineer the strain is to take advantage of the large surface-to-volume ratio in nanostructures. Owing to the large surface-to-volume ratio, the intrinsic strain can be relaxed via the free surface. Since there is no lattice constrain at the free surface, the strained material can deform

elastically in order to reduce the total strain energy. Such phenomena have been studied extensively [50,51], and have been leveraged to grow InGaN with a very high indium content [52, 53]. While most of the work involved bottom-up self-assembled nanostructures, strain relaxation is also possible by top-down processes.

1.4 Thesis Overview

This thesis focuses on utilizing nanostructures to manipulate the strain profile in the InGaN/GaN QW structure and tailor the optical properties for classical LED and non-classical quantum light sources. The thesis is organized as follows: Chapter 2 provides detailed description of our top-down nanostructure fabrication, demonstrating the emission wavelength tuning capability by strain engineering, and monolithic integration of full-color LED arrays; Chapter 3 investigates the electrical nanopillar LED structure and presents the electroluminescence and electrical properties. Chapter 4 investigates the emission polarization via asymmetric strain and the application for polarization-controlled single photon emission; Chapter 5 discusses the random indium fluctuation in atomic scale in InGaN and the influence on QD inhomogeneity; Chapter 6 concludes the thesis and proposes ideas for future studies.

Chapter 2

Monolithically Integrated RGB Full Color Pixels by InGaN Nanopillar Arrays

In this chapter we focus on InGaN nanopillar structures and show the tuning of the emission color by engineering the strain profile. As mentioned in Chapter 1, a lot of work has been done to explore the possibility of integrating emitters of different colors on the same chip. Indeed, independently addressable active color pixels that are integrated on the same chip can have applications in wearable micro-display [54,55,56], color-tunable lighting [57], optogenetics [58], and biomedical sensing [59]. Organic and colloidal quantum dot (QD) emitters of different colors have been assembled onto the same chip using the pick-and-place method [60]. However, the same approach is

difficult to be applied to group-III nitride semiconductor emitters which have the advantages of high power density [61] and long life time [62]. The pick-and-place method is also considerably less scalable compared to standard semiconductor processing technologies, such as lithography and etching. In this chapter, we showed the possibility of integrating blue, green, and red nitride semiconductor emitter materials on the same chip, relying only on standard thin-film epitaxy and patterning techniques commonly used in the light-emitting diode (LED) industry without resorting to multiple or special epitaxial steps [63,64]. The physics underlying the wavelength tuning across the entire color space was investigated and compared to experiments. To our best knowledge, this is the first time wavelength tuning covering all three primary colors has been shown to be possible in InGaN materials without changing the composition or thickness of the quantum wells (QWs).

2.1 Strain and Emission Wavelength

The emission wavelength of an InGaN LED comprising of a multiple-quantum-well (MQW) active region is determined by the structure of the QW including the alloy compositions in both the QW and barrier and the QW thickness as well as the amount of strain in the QW. For MQWs grown on c-plane GaN, the strain in the QW can drastically shift the emission wavelength from the bulk bandgap due to the quantum-

confined Stark effect (QCSE) [43]. The larger the strain, the smaller the photon energy, as illustrated in Figure 2-1. To enable multiple emission wavelengths on the same chip, one must be able to locally control one or more of the following three parameters: the alloy composition of the QW, the thickness of the QW, and the strain in the QW grown on a polar plane. Changing the QW/barrier composition or thickness requires either multiple epitaxial steps or using selective-area epitaxy [63,64]. These changes are limited in their spatial frequency and contrast, and therefore are difficult to be used in applications that require ultra- small and -dense color pixels such as in displays. Changing the strain in the QW, on the other hand, can be achieved by patterning the QW into nanopillars [50]. Strain relaxation in InGaN/GaN nanopillars and its effects on optical properties have been extensively studied in the past [65,66,67,68]. Wavelength shift was accompanied by an increase of the oscillator strength when the nanopillar diameter decreases [68]. The effect becomes most pronounced when the nanopillar diameter is around 100 nm [68,51]. As a result, a rapidly changing strain profile across a small length scale can be easily achieved. Previously, a wavelength shift as much as 50 nm has been observed [68]. In this work, we show that by carefully engineering the strain profile, a wavelength shift as much as 178 nm is possible, which is sufficient for one to tune across the RGB color space.

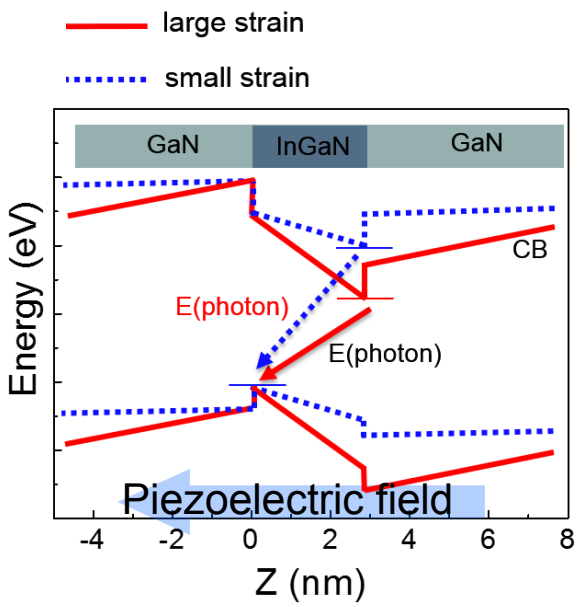

Figure 2-1. Illustration of QW band structures with different strain levels and, as a results, different photon energies. The photon energy roughly corresponds to the energy difference between the bottom of conduction band and the top of valance band.

2.2 Strain Engineering by Nanopillar Structure

As mentioned in the previous section, many studies have shown that nanostructures allow strain relaxation because they have large surface-to-volume ratio, and the strain can be relaxed via the free surface. Among different nanostructures, nanopillar or nanocolumn structure is one of the most effective [65]. It has a higher surface-to-volume ratio compared to nanostripes and nanoholes and allows strain relaxation along all radial directions. To explore the wavelength tuning capability by a nanopillar structure, we employed numerical simulations using nextnano to calculate the strain profile in the nanopillars. The simulated structure was a GaN nanopillar that contains a 3-nm InGaN embedded 10 nm below the top surface. The nanopillar was

surrounded by air. The simulation considered all strain components. There are six strain components (ε), three hydrostatic terms and three shear strain terms:

$$\begin{pmatrix} \varepsilon_1 \\ \varepsilon_2 \\ \varepsilon_3 \\ \varepsilon_4 \\ \varepsilon_5 \\ \varepsilon_6 \end{pmatrix} = \begin{pmatrix} \varepsilon_{xx} \\ \varepsilon_{yy} \\ \varepsilon_{zz} \\ \varepsilon_{yz} \\ \varepsilon_{zx} \\ \varepsilon_{xy} \end{pmatrix}. \tag{2-1}$$

Strain is correlated to stress (σ) by the Hooke's law:

$$\sigma_I = C_{IJ}\varepsilon_J, \tag{2-2}$$

where C_{IJ} corresponds to the elastic constant tensor. For the wurtzite structure, the crystal symmetry allows the elastic tensor to have the following symmetry [69]:

$$\begin{pmatrix} \sigma_1 \\ \sigma_2 \\ \sigma_3 \\ \sigma_4 \\ \sigma_5 \\ \sigma_6 \end{pmatrix} = \begin{pmatrix} C_{11} & C_{12} & C_{13} & 0 & 0 & 0 \\ C_{12} & C_{11} & C_{13} & 0 & 0 & 0 \\ C_{13} & C_{13} & C_{33} & 0 & 0 & 0 \\ 0 & 0 & 0 & C_{44} & 0 & 0 \\ 0 & 0 & 0 & 0 & C_{44} & 0 \\ 0 & 0 & 0 & 0 & 0 & (C_{11}-C_{12})/2 \end{pmatrix} \begin{pmatrix} \varepsilon_1 \\ \varepsilon_2 \\ \varepsilon_3 \\ \varepsilon_4 \\ \varepsilon_5 \\ \varepsilon_6 \end{pmatrix}. \tag{2-3}$$

When there is no external force in the z direction ($\sigma_3 = 0$), and the biaxial strain (ε_1 and ε_2) from lattice mismatch is symmetric, the strain in the z direction is reduced to Equation 1-2. Based on the continuum elastic theory, the strain relaxation in nanopillars was calculated by minimizing the total strain energy *E*

$$E = \frac{1}{2}\int_V \sigma_I \varepsilon_J dV. \tag{2-4}$$

Figure 2-2(a) shows the calculated strain profile of a 20-nm diameter nanopillar. The strain occurs mostly in InGaN and the interface between InGaN and GaN. Due to the larger lattice constant compared to GaN, InGaN layer experienced a compressive strain

(negative strain value), and the GaN near the interface has a tensile strain. What's worth noticing is that the strain profile is not uniform across the in-plane direction. There is no strain at the sidewall because there is no constraint at the sidewall, and the material is able to deform itself at the edge to lower the total strain energy. The strain relaxation can extend into the core of the nanopillar and reduces the strain there. Figure 2-2(b) shows the in-plane strain distribution along the radial direction and elucidates the strain relaxation at the core as the diameter is decreased. For a diameter smaller than 100 nm, the strain relaxation length reaches the center of the nanopillar and causes relaxation at the core. Based on this calculation, strong modification of optical properties is expected when the nanopillar diameter is less than 100 nm. It implies that by properly designing the diameter, the strain profile can be tailored to produce desired optical properties, such as emission color.

Furthermore, the piezoelectric field was calculated as well, based on the strain profile. The piezoelectric polarization is determined by the piezoelectric constant tensor and strain components [69] by

$$\begin{pmatrix} P_{pz,x} \\ P_{pz,y} \\ P_{pz,z} \end{pmatrix} = \begin{pmatrix} 0 & 0 & 0 & 0 & e_{15} & 0 \\ 0 & 0 & 0 & e_{15} & 0 & 0 \\ e_{31} & e_{31} & e_{33} & 0 & 0 & 0 \end{pmatrix} \begin{pmatrix} \varepsilon_1 \\ \varepsilon_2 \\ \varepsilon_3 \\ 2\varepsilon_4 \\ 2\varepsilon_5 \\ 2\varepsilon_6 \end{pmatrix}. \tag{2-5}$$

There are only three independent and five non-zero piezoelectric constants by virtue of

the symmetry of wurtzite structure, and the only nonzero piezoelectric field component is $P_{pz,z}$. The piezoelectric field at the center of InGaN for various nanopillar diameters is shown in Figure 2-3. Although the nanopillar is still partially strained even when the diameter is 10 nm, the reduced QCSE leads to a huge change of photon energy and emission wavelength. Using $\Delta E = \Delta F \times l$, where F is piezoelectric field and $l = 3nm$ is the thickness of InGaN layer, the change of photon energy is estimated be ~ 0.75 eV when the nanopillar diameter is reduced to 10 nm. Such energy change is sufficient to cover the entire visible spectrum and indicates that strain engineering by designing the nanopillar dimension can be a viable approach to manipulate the emission color. In the following sections, we will employ nextnano to solve the strain-involved band structure and energy states in order to obtain more accurate emission wavelength, using parameters in Table 2-1.

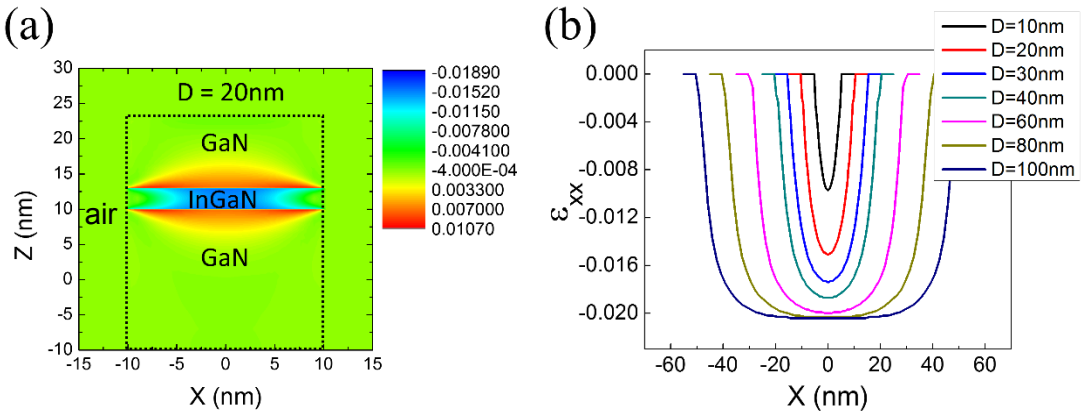

Figure 2-2. (a) Distribution of in-plane strain component, ε_{xx}, in a 20-nm $In_{0.12}Ga_{0.88}N$/GaN nanopillar showing zero strain at the sidewall and partial strain at the center. (b) ε_{xx} along x axis for different nanopillar diameters.

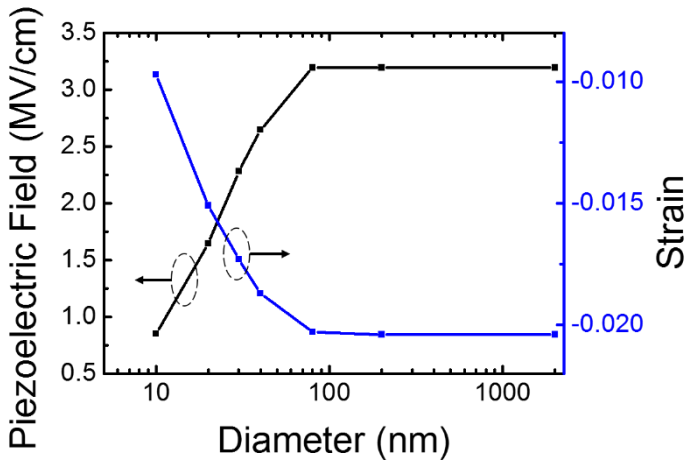

Figure 2-3. Biaxial strain and piezoelectric field at the center of $In_{0.12}Ga_{0.88}N$/GaN nanopillars for various diameters from nextnano simulations (Figure 2-2), showing strain relaxation and strong reduction of piezoelectric field for small diameters.

2.3 Nanopillar Fabrication

Experimentally, we fabricated InGaN/GaN nanopillars by a top-down approach. The samples used in this work consisted of a single InGaN QW to avoid complexity from nonuniform emission from different QWs. The sample was grown by metal-organic chemical vapor deposition (MOCVD) on a c-plane sapphire substrate. Typical GaN and InGaN thin-film growth conditions were used. Two samples with nominal indium compositions of 15% and 32% in the QW were grown. In the following, we will refer to the high-indium composition sample as sample A and the low-indium composition sample as sample B. To fabricate nanopillars, electron-beam lithography and reactive ion etching were used followed by wet etching in 2% KOH solutions (using

AZ400K photoresist developer). The wet etch helped remove surface damages due to plasma etching and achieve a vertical sidewall profile [70]. The fabrication processes are summarized in Figure 2-4. The scanning electron micrograph of the as-fabricated nanopillars are shown in Figure 2-5.

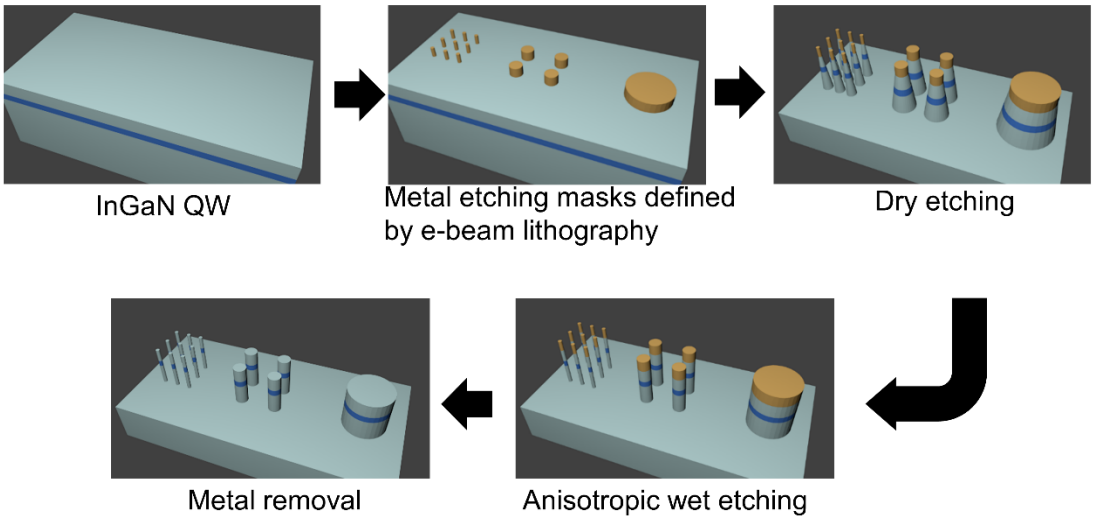

Figure 2-4. Schematic illustration of the nanopillar process flow. Nanopillars with different diameter and thus different emission color can be easily integrated on a single chip by one lithography and etching step.

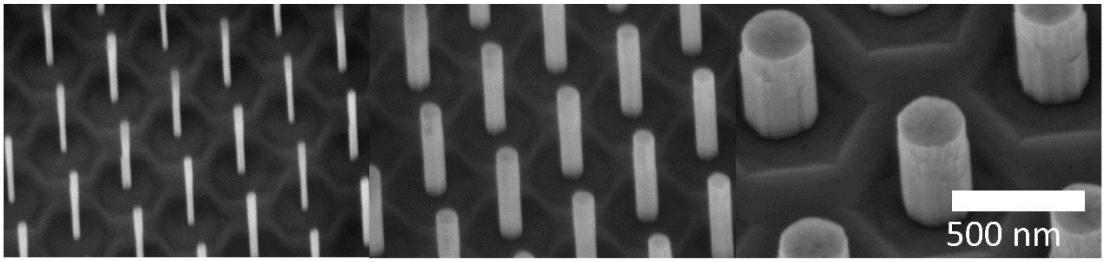

Figure 2-5. Top-down InGaN/GaN nanopillars of various diameters (35 nm, 90 nm, and 250 nm from left to right). The nanopillar diameters and positions were defined by the e-beam lithography. The height (300 nm) was determined by the ICP dry etching, and the subsequent anisotropic KOH wet etching made the sidewall vertical and left

hexagonal marks at the base of each nanopillar.

2.4 Optical Properties of InGaN Nanopillars

Photoluminescence (PL) measurements were performed at 10 K to characterize the emission properties of InGaN/GaN nanopillars. The measurement setup is illustrated in Figure 2-6. Low temperature was used to enhance the signal-to-noise ratio of long-wavelength emission from sample A. A 390-nm wavelength femtosecond mode-locked laser with 80-MHz repetition rate and 150-fs pulse duration was used as the excitation source. The incident angle was 50° from the normal direction of sample surface, and the spot size was ~40 μm in diameter. The emission spectra were acquired by a monochromator and a cryogenically cooled charged coupled device (CCD) with a spectral resolution of 0.1 meV at 400-nm wavelength. The real-time images of nanopillar emission were taken by a color CCD.

Figure 2-7 shows the emission spectra for sample A at various nanopillar diameters. The blue-shift of wavelength as diameter reduced is clearly seen. Figure 2-8(a) shows the letters “MICHIGAN” composed of nanopillars of different diameters. The SEM images of the nanopillar pixels are in Figure 2-8(b). It can be seen that the wavelength tuning spans the RGB color space and the emission color can be varied rapidly within a sub-micron length scale.

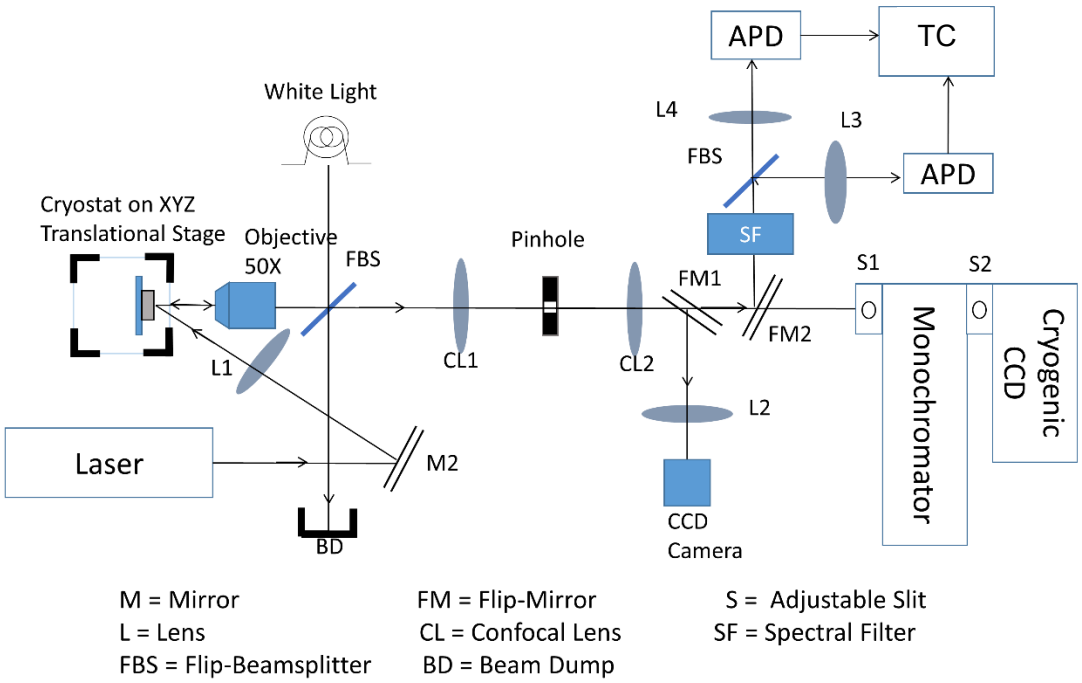

Figure 2-6. Schematic of the PL measurement setup.

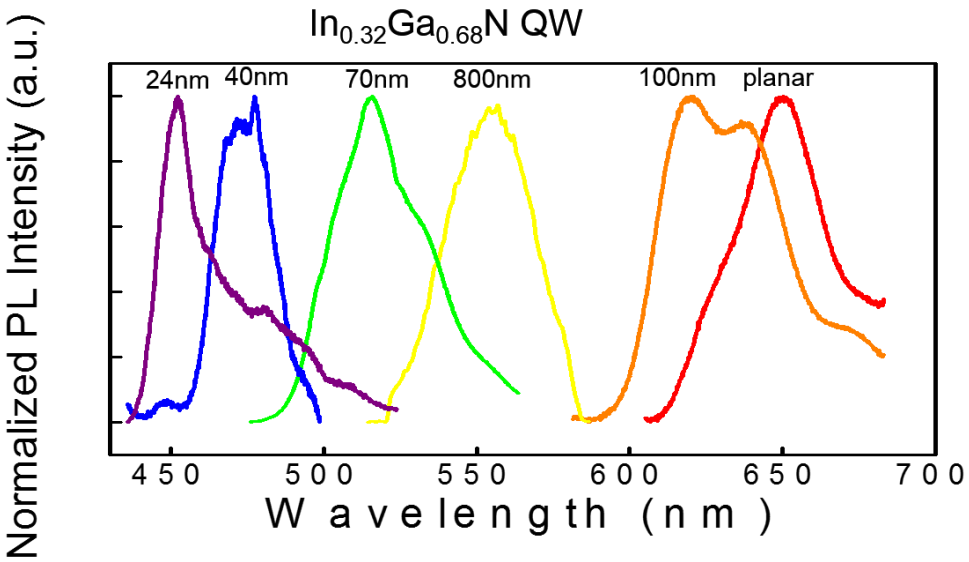

Figure 2-7. PL spectra acquired from nanopillar arrays with different diameter. The blue-shift as the diameter reduced was clearly seen.

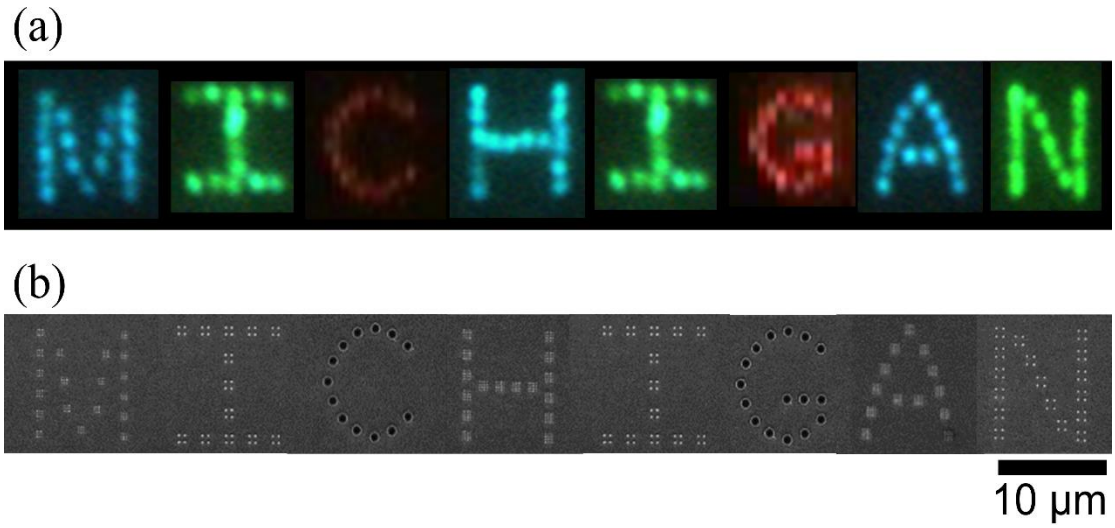

Figure 2-8. (a) Real-time image of full-color emission from nanopillars acquired by color CCD. (b) The SEM images of nanopillar pixels composing the “MICHIGAN”.

Figure 2-9 shows the emission wavelength versus the nanopillar diameter and the comparison to the theoretical calculations. In our theoretical model, the emission wavelength was calculated based a strain profile that minimizes the total strain energy in the nanopillar under the continuum elasticity approximation. After the strain profile in the InGaN QW was obtained, the band structure was calculated based on a six-band k-dot-p model using nextnano, that is the interaction between the conduction band and the valence bands was ignored. The emission wavelength was then determined by solving the Schroedinger’s equation under the effective mass approximation. No screening of the piezoelectric field was considered which would be important when the carrier concentration in the InGaN region becomes very high. To elucidate the physics of strain relaxation, the numerical results were fitted with an analytical equation below

that was obtained under the same continuum elasticity approximation but considered only one radial direction of the InGaN QW [68].

$$E_{ph} = E_0 - B_m(1 - \mathrm{sech}(\kappa R)) \quad (2\text{-}6)$$

In equation (1), E_{ph} is the photon energy, E_0 is the bulk InGaN bandgap without any strain, B_m is the amount of red shift in photon energy in a fully strained InGaN/GaN QW due to the quantum-confined Stark effect, and *R* is the radius of the nanopillar. The good agreement between equation (1) and numerical results suggests the dominant role of strain relaxation in the radial direction on the emission wavelength of the QW. The fitting parameter $1/\kappa$ can be interpreted as a characteristic length for strain relaxation. Physically, $1/\kappa$ corresponds to the depth of strain relaxed region from the circumference of the nanopillar. κ depends on the elastic properties of InGaN [68]. Comparing theoretical result to the measurements, sample B shows a good agreement. However, sample A shows a significant deviation between the calculated emission wavelength from the measurement. In order to obtain a good fit, a larger $1/\kappa$ than predicted from continuum elasticity model is needed, assuming the same elasticity constants for both samples. This suggests that either 1) the elasticity constants depend on the indium composition or 2) more relaxation than the theoretical value occurred. More strain relaxation was also confirmed by the fact that the emission wavelength did

not blue-shift further for QD diameter below 40 nm from sample A. It manifested that the nanopillars were already fully strain relaxed.

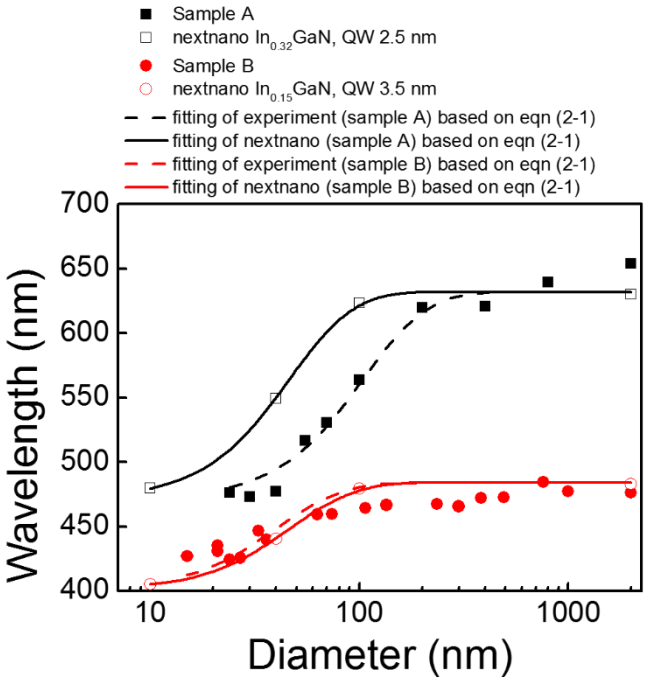

Figure 2-9. Diameter-dependent wavelength of sample A and B and the theoretical modeling by nextnano. For sample A, the nextnano predicted $\frac{1}{\kappa}$ = 13.6 nm while the experimental data suggested 31.3 nm. For sample B, $\frac{1}{\kappa}$ = 12.4 and 14.5 nm based on nextnano and experimental data respectively.

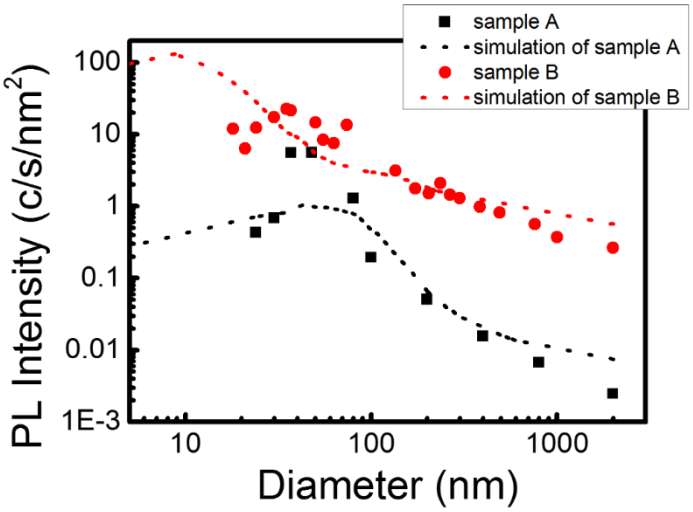

Figure 2-10. Diameter-dependent PL intensity and the theoretical curves based on the 1-D strain model.

Figure 2-10 shows the emission intensity as a function of the nanopillar diameter, both from experiments and numerical calculations. Overall, sample A emitted much lower intensity because of more defects generated during InGaN epitaxy growth of such high indium composition. To investigate the diameter-dependent behavior, we combined the aforementioned 1-D strain model and 1-D wavefunctions to calculate the wavefunction overlap integral for various diameters, aiming to provide a simple and accurate model to theoretically estimate emission intensity from nanopillars. The $1/\kappa$ obtained from Figure 2-9 was employed to calculate the strain in the QW for various nanopillar diameters based on the 1-D strain model, using the equation below [68]:

$$\varepsilon = \varepsilon_0(1 - \mathrm{sech}(\kappa R)) \quad . \tag{2-7}$$

The calculated strain was then used as the input parameter to construct the 1-D band structure of the QW structure that allows us to solve for the wavefunction of the 1st electron and hole state and the corresponding wavefunction overlap intergral. As the nanopillar diameter decreases, the strain relaxation becomes more prominent, and the wavefunction overlap integral increases, which leads to larger oscillator strength and higher emission intensity. The optical effect due to nanopillar geometry was also taken into account at this point. The diameter-dependent optical efficiency included the absorption efficiency, Purcell effect, and collection efficiency, as discussed in Reference 68. The relative values of emission intensity was subsequently obtained from multiplying the wavefunction overlap integral by the optical efficiency for various diameter. The results are shown in Figure 4. Despite the simplified model, the theoretical results fit the measured emission intensity qualitatively well. The larger $1/\kappa$ of sample A implied more effective strain relaxation, and, therefore, the emission intensity began to increase rapidly at a larger diameter compared to sample B, which had a smaller $1/\kappa$. As can be seen from both theoretical curve and experimental intensity, sample A showed stronger intensity enhancement as the diameter approached 100 nm and below. The intensity peaked at 40 nm because nonradiative recombination at nanopillar sidewall began to dominate for smaller diameters [68]. As for sample B, the model predicted that the intensity would benefit from strain relaxation at ~ 50 nm.

However, it can hardly be seen in the experimental data. It is likely due to the fact that nonradiative recombination also occurred for such small diameters and decreased the emission intensity.

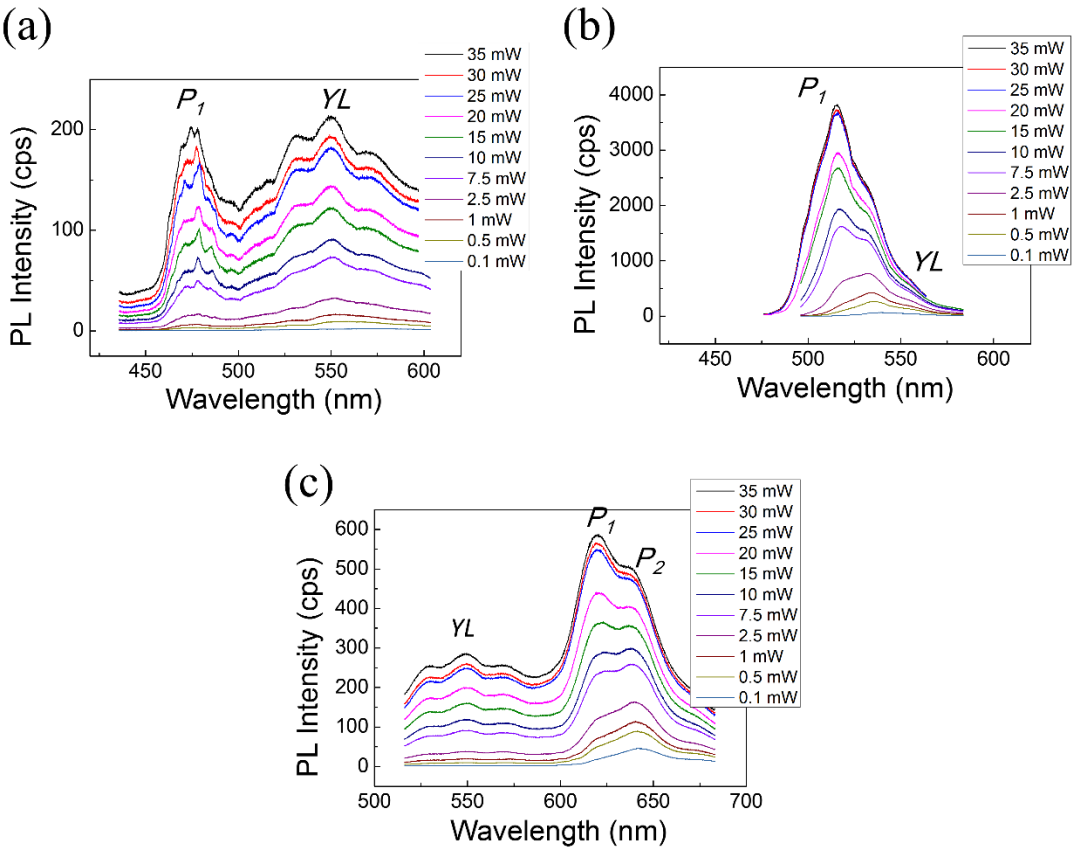

Figure 2-11. Power-dependent PL spectra of 40-nm, 70-nm, and 800-nm nanopillar arrays. PL emission originated from the center region of nanopillars, localized states, and defects (yellow band) is labeled.

Lastly, in Figure 2-11, we compared the emission spectra for the RGB pixels shown in Figure 2-8. Multiple peaks were observed in each spectrum. The peaks corresponding to around 550 nm wavelength are common for all three colors and were

assigned to the yellow luminescence (YL) commonly observed in nitride semiconductors. Peaks P_1 are emission from the center of the nanopillar. Peaks P_2 are likely emission from localized states (e.g. due to indium composition or well width fluctuation) because their linewidths remain nearly constant with an increasing excitation intensity and intensity saturated quickly. No emission from the edge seemed to be observable from our samples as opposed to what was reported previously [71].

2.5 Conclusion

In summary, we designed the diameters of InGaN GaN nanopillars to generate desired strain profile and emission wavelength and achieved full-color emission from monolithically integrated arrays fabricated by a top-down approach. The diameter, height, and position of the nanopillars were precisely controlled by the top-down approach, which also allowed effective strain relaxation, reduced piezoelectric field, and wavelength tuning from red to blue. Photoluminescence measurements were carried out at 10 K. The PL spectra and real-time CCD images proved that nanopillar arrays indeed emitted red, green, and blue colors. We also applied our previously developed 1-D strain model to analyze the diameter-dependent wavelength and emission intensity. The characteristic length, $1/\kappa$, was proved to be a useful parameter to describe the degree of strain relaxation and predict the optical properties.

Table 2-1. Parameters used throughout the dissertation for semiconductor modeling.

	GaN	InN		GaN	InN
a (nm)	0.3189	0.3545	D_2 (eV)	4.5	4.5
c (nm)	0.5185	0.5703	D_3 (eV)	8.2	8.2
E_g (eV)	3.51	077	D_4 (eV)	-4.1	-4.1
Δ_{cr} (eV)	0.01	0.04	D_5 (eV)	-4.0	-4.0
Δ_{so} (eV)	0.017	0.005	D_6 (eV)	-5.5	-5.5
$m_e^{\parallel}$	0.206	0.07	C_{11} (GPa)	390	223
$m_e^{\perp}$	0.202	0.07	C_{12} (GPa)	140	115
$m_{hh}^{\parallel}$	1.1	1.63	C_{13} (GPa)	106	92
$m_{hh}^{\perp}$	1.6	1.63	C_{33} (GPa)	398	224
A_1	-7.21	-8.21	C_{44} (GPa)	105	48
A_2	-0.44	-0.68	e_{15} (C/m^2)	-0.30	-0.48
A_3	6.68	7.57	e_{31} (C/m^2)	-0.35	-0.57
A_4	-3.46	-5.23	e_{33} (C/m^2)	1.27	0.97
A_5	-3.4	-5.11	P_{sp} (C/m^2)	-0.034	-0.042
A_6	-4.9	-5.96	E_g bowing factor	1.4	
D_1 (eV)	-3.7	-3.7			

Chapter 3

Pixelated Multi-Color LED Array via Strain Engineering in InGaN

One common challenge of nanostructure-based LEDs is proper metal contact formation for electrical operation. The non-planar nature of nanostructures can make uniform metal deposition difficult. Moreover, a lot of self-assembled nanostructures are grown randomly on the sample surface without well-defined positions and heights. It makes device integration even more challenging. In this Chapter, we will present a metallization scheme that can be applied to the nanopillar LEDs and demonstrate pixelated multi-color nanopillar-based LEDs. Some successful multiple color devices have been reported, using bottom-up MBE InGaN/GaN nanowires and colloidal II-VI

QD arrays [53,60,63]. However, these materials either lack the scalability for pixelated LED arrays or require complicated manufacturing processes that can not be easily adopted for commercial products. In this work, we showed that via strain engineering in InGaN quantum wells grown by standard epitaxy, one can develop a scalable fabrication scheme to make monolithically integrated and electrically driven multi-color LED arrays. Each LED consists of an array of InGaN/GaN nanopillars that are formed by lithography and etching. The emission color of each LED device can be controlled by the diameter of the constituent InGaN nanopillars.

3.1 Fabrication of Electrically-Driven Nanopillar LEDs

The proposed electrical contact fabrication scheme is illustrated in Figure 3-1. After defining nanopillars following the approach shown in Figure 2-4, we deposited 50-nm Si_3N_4 by PECVD at 200ºC as the insulating layer. In order to planarize the sample, we spin-coated spin-on-glass (SOG 500F, Filmtronics Inc.) and annealed it at 400 ℃ for one hour in N_2 ambient to get rid of the solvent and harden the SOG. The resultant thickness of SOG was ~ 600 nm. A plasma etching was subsequently performed to expose the p-GaN region. The plasma etching species were mainly fluorine radicals and etched both SOG and Si_3N_4. Typically ~ 50 nm of p-GaN was exposed as a result of slight over-etch in order to ensure that all nanopillars were

exposed. Figure 3-2 shows the SEM image of a nanopillar array after the plasma etch-back.

To form the p-GaN/metal contact, we deposited Ni/Au (8 nm / 8 nm) by e-beam evaporator (Cooke evaporator). The sample was mounted at a 60º angle and rotated during the deposition for better coverage on the sidewall of nanopillars. The Ni/Au was annealed at 500 ℃ for five minutes in an ambient consisting of an O_2/N_2 mixture (1:4). The oxygen preferentially oxidized the Ni and formed NiO_x which is a p-type semiconductor with a lot of nitrogen vacancies. Also, as nickel atoms diffused toward the top, the gold layer became gold islands in direct contact with p-GaN, and gallium atoms out-diffused from p-GaN, leaving Ga vacancies that were p-type dopants and increasing the p-doping level at p-GaN surface [72]. In addition, the Ni/Au film became semi-transparent after the oxidation [72,73] improving light extraction from the top surface. To form the n-GaN/metal contact, we carried out buffered HF wet etching to remove SOG and Si_3N_4 to open a window on n-GaN surface and deposited Ti/Au (10 nm / 250 nm) as n-type electrode by e-beam evaporator (Enerjet evaporator). The final device structure is shown in Figure 3-3.

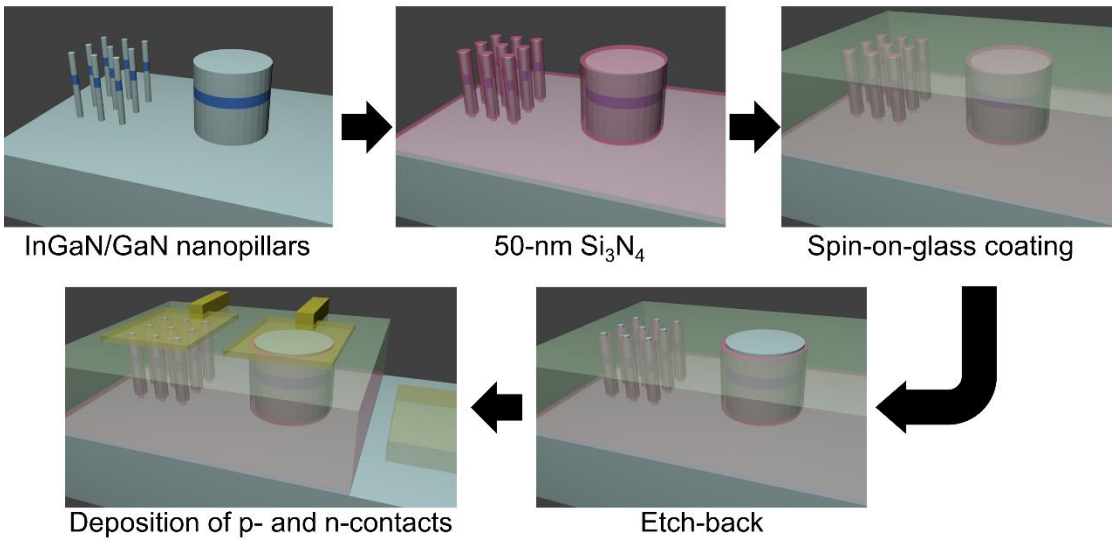

Figure 3-1. Process flow of nanopillar LED arrays.

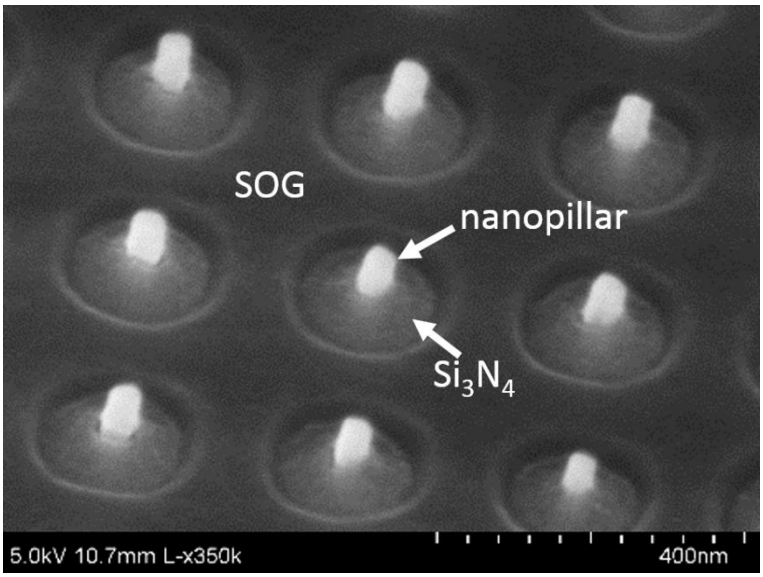

Figure 3-2. SEM image of a nanopillar array after plasma etch-back showing the p-GaN tips, Si_3N_4 insulating layer, and SOG planarization layer.

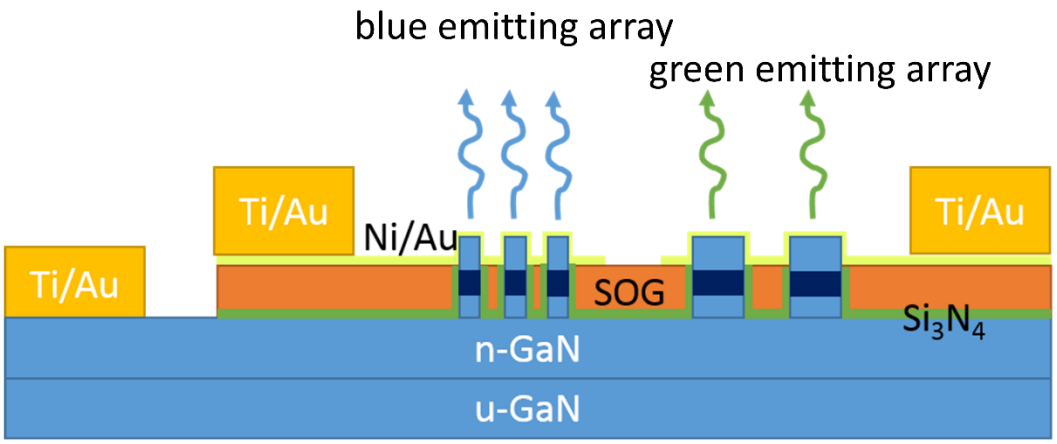

Figure 3-3. Schematic of the nanopillar LED structure.

3.2 Electroluminescence of Nanopillar LEDs

In our experiment, we used a green-emitting c-plane InGaN MQW sample comprising of a standard LED epistructure with six InGaN MQWs sandwiched between p-GaN and n-GaN. Electroluminescence was observed at room temperature under current injection. The real-time images of electroluminescence of 65-nm, 100-nm, and 1-μm nanopillar arrays are summarized in Figure 3-4. The blueshift of emission wavelength was clearly observed in these images. The 1-μm nanopillars resembled the planar QW and emitted green light, while the 65-nm nanopillars were strain-relaxed and emitted blue light. The emission spectra at different current density were measured by a spectrometer (Ocean Optics USB2000+) in an integration sphere at room temperature, as shown in Figure 3-5. The current density was calculated based on the total cross-sectional area of the nanopillars. The peak wavelengths of 1-μm and 65-nm

nanopillars were 510 nm and 478 nm, respectively. Together with the CCD images, multiple color emission from a single LED chip was demonstrated.

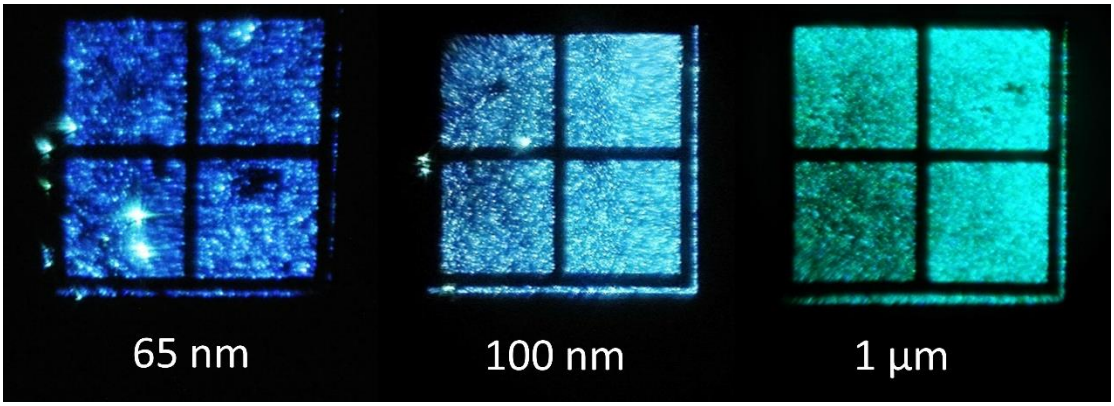

Figure 3-4. Real-time images of the electroluminescence from nanopillar LED arrays. The nanopillar diameter from left to right is 65 nm, 100 nm, and 1 μm respectively. The size of each array is 100 μm × 100 μm. The pitch between nanopillars was 300 nm for 65-nm and 100-nm arrays and 3 μm for 1-μm pillars.

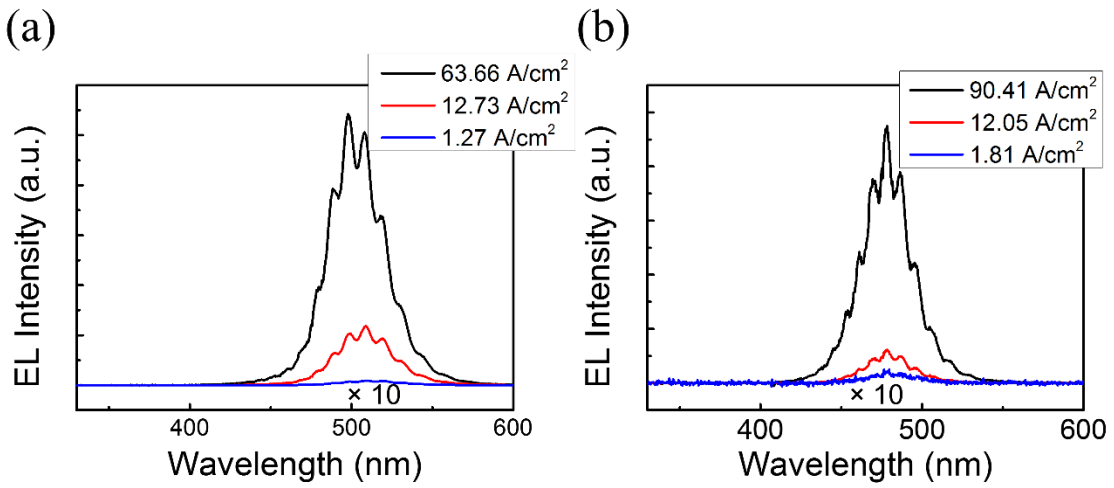

Figure 3-5. The emission spectra of (a) 1-μm and (b) 65-nm nanopillar arrays under different current injection level. The spectra showed multiple peaks as a result of interference fringes caused by reflection at air/GaN and GaN/sapphire interfaces. The EL intensity at very low current density was magnified by 10X for clarity.

The wavelengths at different current densities were obtained by fitting the spectra with Gaussian functions and summarized in Figure 3-6(a). For the 1-μm nanopillar array, the wavelength was 515 nm at the low current density and showed an obvious blueshift as the current density increased. This is because the free carriers screen the piezoelectric field and reduce the QCSE [66]. The results suggest that there is a large strain in 1-μm nanopillars. In contrast, the 65-nm nanopillars only showed 3-nm wavelength shift, from 482 nm to 479 nm, as the current density was initially increased to 6 A/cm^2, and the wavelength remained the same at a larger current density. It proved that 65-nm nanopillars were already partially strain-relaxed, and a small amount of free carriers was sufficient to screen the piezoelectric field completely.

The strain and piezoelectric effect also affected the spectral linewidth. The full width at half maxium (FWHM) of the electroluminescence spectra was recorded at various current densities. In Figure 3-6(b), we observed very different power dependent behaviors of FWHM from 1-μm and 65-nm nanopillar arrays. For the 1-μm nanopillars, the FWHM decreased as the current density increased. This is again due to the screening of the piezoelectric field which is known to increase the emission linewidth [74,75]. For the 65-nm nanopillars, the FWHM had huge error bars at low current density because the intensity was weak and the fitting was more difficult. Regardless, the FWHM first decreased and reached a minimum at 6 A/cm^2, which was the current

density required to fully screen the piezoelectric field (Figure 3-6(a)). Therefore, this FWHM narrowing was attributed to the screening of piezoelectric field. As the current density increased further, the FWHM of 65-nm nanopillars broadened because of the band filling effect.

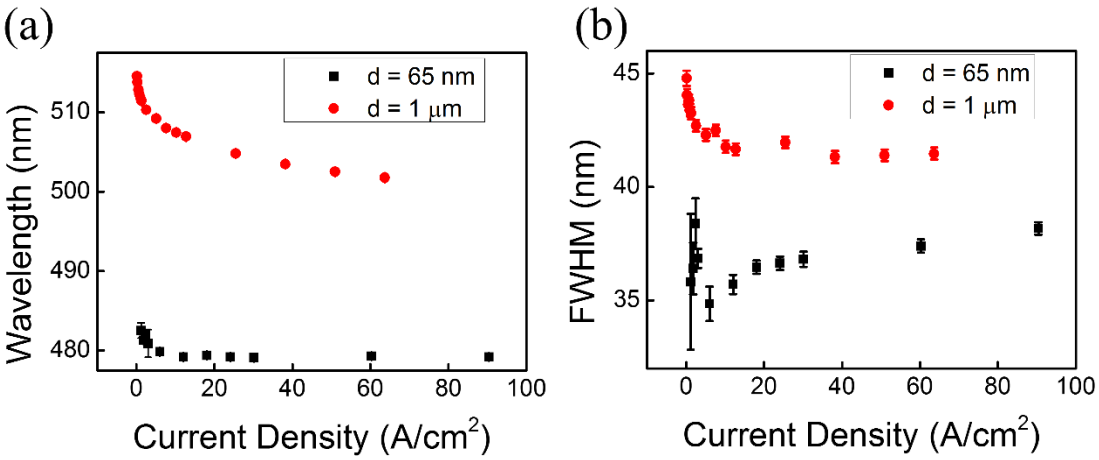

Figure 3-6. (a) Peak wavelength of 1-μm and 65-nm nanopillar LEDs at various current density. Because of the interference fringes, we fitted the spectra with Gaussian functions in order to obtain accurate peak wavelength. The error bars correspond to the fitting errors. (b) The FWHM of electroluminescence spectra from fitted data.

In Figure 3-7, we show the integrated intensity at various current density. In Figure 3-7(a), the integrated intensity is observed to be linear at low injection level for 1-μm nanopillars and shows a slight degradation of efficiency as the current density increases. This is attributed to strain-related efficiency degradation, such as electron leakage [44,76]. As for 65-nm nanopillars, the light output is almost linearly proportional to the injection level and shows no efficiency degradation in the current range used in the

measurement. The results echoed previous studied based on bottom-up nanowires [77,78]. In addition, we observed much lower light output from 65nm nanopillars. The ratio of areal emission intensity, $I_{1\mu m}/I_{65nm}$, is shown in **Error! Reference source not found.**(c), representing the ratio of QE, $\eta_{1\mu m}/\eta_{65nm}$, at various current densities. At low current injection level, $\eta_{1\mu m}$ was higher than η_{65nm} by two orders of magnitude. As the injection level increased, $\eta_{1\mu m}$ degraded, and the QE ratio dropped. To simplify the discussion, we focus on low injection level for the following discussion. The large QE difference at low injection suggested that 65-nm nanopillars had very low QE, and 1-μm had very high QE. Based on previously developed model [79], at room temperature the dominant nonradiative recombination mechanism in 65-nm nanopillars is carrier thermalization and recombination at sidewall traps. Following Reference 79, the thermalization rate, γ_{thm}, can be derived using $\frac{c_2}{D}V_B e^{-c_3\phi_B/kT}$, where V_B is the thermal velocity, and ϕ_B is the potential barrier from the center of the nanopillar to the sidewall. ϕ_B is caused by strain relaxation in the radial direction and was determined by fitting the diameter-dependent wavelengths to be 151.5 meV in this study. c_2 and c_3 values were obtained from Reference 79 to be 0.002 and 0.33 respectively. The derived γ_{thm} is 0.94 GHz and much faster than the radiative decay rate, which is estimated to be 0.012 GHz according to the calculated wavefunction overlap and Fermi's golden rule. The resultant QE, η_{65nm}, was 1.26% for 65-nm nanopillars, and

it would be even lower if the bulk nonradiative decay is also considered. To estimate $\eta_{1\mu m}$, we have to take into account the carrier diffusion length. When the carriers are within the diffusion length from the sidewall, the above thermalization model can be applied, and γ_{thm} is calculated by replacing the diameter term, *D*, with two times of the diffusion length, *L,* and the equation becomes $\frac{c_2}{2L}V_B e^{-c_3\phi_B/kT}$. The overall $\eta_{1\mu m}$ was calculated by averaging the QEs in the areas where carriers can diffuse to the sidewall and areas close to the core where carriers suffer from only bulk nonradiative recombination. Assuming 100-nm diffusion length [80], $\eta_{1\mu m}$ was derived to be 66%, assuming no bulk nonradiative recombination. Comparing the derived η_{65nm} and $\eta_{1\mu m}$, obviously $\eta_{65nm}$was overestimated. It implied that the junction temperature of 65-nm nanopillars was higher than the room temperature. Our calculation revealed that the junction temperature of 65-nm nanopillars was 433K. Another possibility was that the interface quality with InGaN and PECVD Si_3N_4 was poor, and, therefore, c_2 was high. The impact of surface passivation on c_2 requires further investigations.

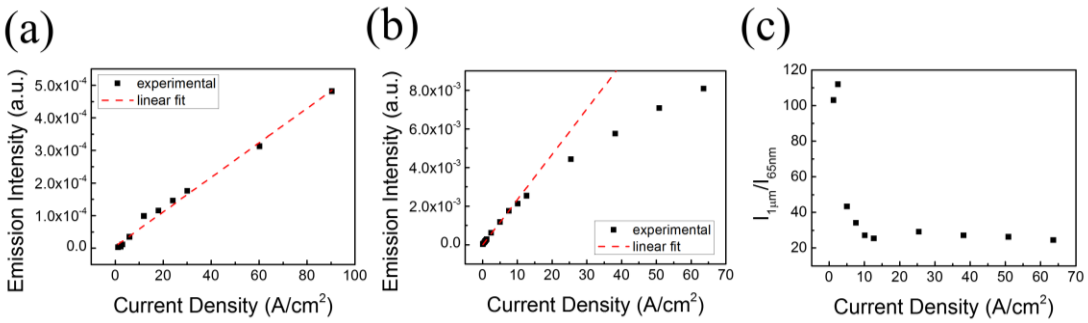

Figure 3-7. Emission intensity of (a) 1-μm and (b) 65-nm nanopillars at various current density. (c) The ratio of emission intensity, $I_{1\mu m}/I_{65nm}$, which represents the ratio of QE at various current density.

3.3 Electrical Characteristics of Nanopillar LEDs

I-V measurements were performed at room temperature using the Keithley 4200 semiconductor characterization system. Nanopillars LEDs exhibited diode behaviors as shown in Figure 3-8(a) and (b). The I-V characteristics can be well explained by the equivalent circuit in the inset of Figure 3-8 (c). The p-contact is modelled by a reversed Schottky junction. At reverse applied bias, the Schottky p-contact diode was turned on and allowed large current. The current was limited by the trap-assisted tunneling leakage current through the MQW using the following equation [81,82]:

$$I_{rev} = A(V + V_b)^{3/2} \exp\left(\frac{-B}{(V+V_b)^{1/2}}\right), \quad (3\text{-}1)$$

where V is the magnitude of reverse bias; V_b is the tunneling barrier height in voltage and equal to the band gap energy at reverse bias; A and B are fitting parameters. For 1-μm nanopillars, we obtained A = 0.037 $A{\cdot}V^{-3/2}{\cdot}cm^{-2}$ and B = 10.85 $V^{1/2}$, while A = 0.469 $A{\cdot}V^{-3/2}{\cdot}cm^{-2}$ and B = 14.98 $V^{1/2}$ for 65-nm nanopillars. Such trap-assisted leakage

current at reverse bias was commonly observed from GaN LEDs and was attributed to the high defect density in GaN material [83,84]. At around 0 V, the I-V characteristics was symmetric, indicating that the current was dominated by the leakage current through the shunt resistance. It can be simply fitted to the $I = V/R_s$ equation. The fitting results suggested that $R_s = 5.68\times10^3$ and 6.03×10^3 $\Omega\cdot cm^2$ for 1-μm and 65-nm nanopillars respectively. The most likely shunt leakage path was the interface between nanopillar surface and Si_3N_4 and/or dislocations that extended from n-GaN to p-GaN. Although 65-nm nanopillars had larger sidewall area, the 1-μm nanopillar array showed larger shunt leakage current. It indicated that the shunt leakage was mainly via the dislocations, as the 1-μm nanopillar array indeed had larger total cross-section area and, thus, more dislocations. Nonetheless, the shunt leakage current became negligible as the voltage was increased, and it implied effective insulation by Si_3N_4. At forward bias, the following diode equation was applied:

$$I_{for} = I_0 \exp\left(\frac{qV}{nkT}\right). \quad (3\text{-}2)$$

Note that even at 8 V, the current was still exponential to the voltage with the same quality factor, showing no sign of series resistance. Hence we omitted the series resistance in the model. The fitting rendered quality factors of 33.4 and 31.6 for 1-μm and 65-nm nanopillar arrays. These values are much larger than typical InGaN LEDs. It was mainly attributed to the Schottky contact at the p-GaN surface because the p-

GaN region was damaged by plasma during SOG etch-back, and Fermi level pinning occurred, leading to a large Schottky barrier. When the LED was forward biased, the Schottky junction was at reverse bias. For reverse-biased Schottky junction, the current is mainly tunneling current and can be described by the equation [85]:

$$I_1 = I_0 \cdot \exp\left(\frac{qV_1}{\varepsilon'}\right) = I_0 \cdot \exp\left(\frac{qV_1}{n_1 kT}\right), \quad (3\text{-}3)$$

where $\varepsilon' = \frac{\varepsilon_0}{\frac{\varepsilon_0}{kT}-\tanh(\frac{\varepsilon_0}{kT})}$ and $\varepsilon_0 = \frac{q\hbar}{2}\sqrt{\frac{N_A}{m^*\epsilon}}$. ε' is a characteristic energy of the tunneling current. It is related to the tunneling barrier thickness and, therefore, governed by the band bending and doping concentration, N_A. By assuming that the hole concentration, N_A, in p-GaN was 8×10^{17} cm^{-3} and hole effective mass equals m_0, the ideality factor n_1 is 27. In addition, we have also characterized a planar LED structure made from the same MQW wafer and found n_2 to be ~ 8. It agreed with the typical ideality factor of InGaN MQW LEDs and was attributed trap-assisted tunneling. Based on the equation, $\sum V = \frac{\mathrm{kT}}{q} \cdot \ln\frac{I}{I_0} \cdot \sum n$, the overall ideality factor (n) was then the summation of the ideality factor of the reverse-biased Schottky contact (n_1) and that of the forward-biased p-i-n junction in nanopillars (n_2). The summation of n_1 and n_2 was then in good agreement with the overall ideality factor, n, obtained from the fitting of nanopillar LEDs. Furthermore, the turn-on voltage of nanopillar LEDs was around 5.5 ~ 6 V. The turn-on voltage was defined as the voltage at which the current was 20 mA per mm^2 or 2 A/cm^2 according to conventional LED standard. The turn-on voltage was

slightly higher than planar MQW LEDs because of the Schottky contact. Possible strategies to heal the plasma damage should be explored in the future to reduce the turn-on voltage and contact resistance.

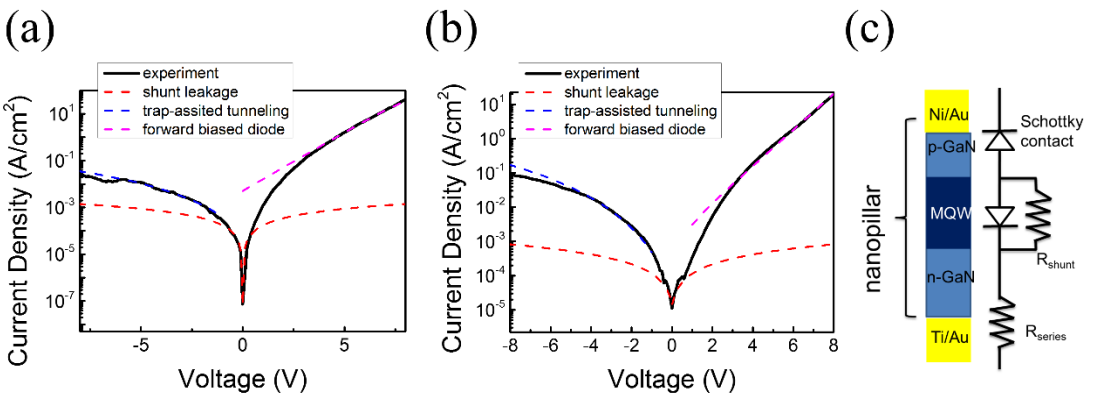

Figure 3-8. (a) and I-V of 1-μm and 65-nm nanopillar arrays and the fitting results of different current components. (c) The equivalent circuit model for nanopillar LEDs.

3.4 Conclusion

In summary, we successfully demonstrated electrically driven multi-color nanoLEDs that were monolithically integrated on one single chip and fabricated by a scalable top-down approach. The emission wavelength of was blue-shifted from 515 nm to 480 nm as a result of diameter reduction. Note although electron-beam lithography was used in this study to facilitate the sample fabrication, the nanopillar dimensions shown in this study can be readily produced by photolithography techniques used in current semiconductor industry. The electrical characteristics were also analyzed and revealed a turn-on voltage about 5.5 ~ 6 V and effective sidewall

insulation. The turn-on voltage can be further improved if the plasma damage issue and the resultant Schottky p-contact are properly addressed.

Chapter 4

Polarization-Controlled Single Photons from Elliptical QDs

In this chapter, we present top-down InGaN QDs based on the same nanopillar process described in Chapter 2. When the nanopillar diameter is below 40 nm, the confinement in the InGaN nanodisk is strong enough to make it behaving like a QD, which exhibits discrete energy states and can generate single photon emission. While most of the QD fabrication methods are bottom-up, the top-down fabrication approach endows us certain advantages that are important for QD applications. The top-down approach guarantees optimal controllability of QD positions and geometries, which is essential for device integration and quality control. In this chapter we will focus on engineering QD geometry in order to intentionally generate anisotropic strain profile

and manipulate the polarization state of single photons.

4.1 Strain Relaxation and Quantum Confinement of the Top-Down InGaN QD

Before jumping into the polarization properties, we review the important basic knowledge of our top-down InGaN QDs in this section. Following the nanopillar fabrication processes as described in Chapter 2, we were able to fabricate InGaN nanodisks with diameter as small as 20 nm. It resembled the bottom-up axial quantum-dot-in-wire structures. The QD-like PL was first observed in 2011 from our top-down InGaN QDs [86]. Later on, the QD nature and the single photon emission were verified [87]. Such results were rather surprising because 1) the lateral dimension of our QDs was much larger than the exciton Bohr radius of GaN which is 3 nm, and 2) the QDs were optically active in spite of the etched sidewall. Based on the Bohr model for a hydrogen atom, the Bohr radius, a_B, describes the size of the electron-hole pair that forms an exciton and can be calculated based on:

$$a_B = \frac{4\pi\varepsilon_0\varepsilon\hbar^2}{\mu e^2}, \tag{4-1}$$

where $\mu = \frac{m_e m_h}{m_e + m_h}$ is the reduced mass, and ε is the relative permittivity of the QD material. The bulk Bohr radii of some common QD materials are listed in Table 1-1Table 4-1. Usually the Bohr radius is deemed as an indicator of the QD size required to strongly confine an electron and a hole to form an exciton. Apparently, our top-down

QDs had physical diameters much larger than the Bohr radius yet still exhibited the QD-like behavior. This is because the real confinement came from the nonuniform piezoelectric field in the radial direction as a result of the strain relaxation. The strong piezoelectric field at the center and weak piezoelectric field at the edge created a potential valley at the QD center that greatly enhanced the confinement. The potential can be expressed analytically by the following equation [68]:

$$\phi(r) = B_m\big(1 - \mathrm{sech}(\kappa r)\big), \tag{4-2}$$

where B_m corresponds to the exciton energy difference between fully strained and fully relaxed InGaN, and $1/\kappa$ is the characteristic length of strain relaxation. The potential can also be mapped out numerically by solving eigenstates in QWs under specific strain conditions that corresponded to the strain at various radial positions. Both the analytical and numerical results are shown in Figure 4-1 and found to be in good agreement with each other. Such potential profile resulted in an effective diameter that was much smaller than the physical diameter. The effective diameter can be estimated by a particle-in-a-circular-box model, where the energy increase due to quantization is:

$$\Delta E = \Delta E_z + \Delta E_r. \tag{4-3}$$

In the above equation, ΔE_z corresponds to the quantization in the growth direction. Because of the piezoelectric field, ΔE_z was obtained by solving energy states in a 1-D triangular well. Similarly, ΔE_r was derived by solving energy states in a circular well.

Circular potential well and eigenstates can be readily solved analytically. Assuming zero potential in the well, the first energy state can be determined to be [88]:

$$\Delta E_r = \Delta E_e + \Delta E_h = \frac{(2.405)^2 \hbar^2}{2R^{*2}} \left(\frac{1}{m_e} + \frac{1}{m_h}\right), \quad (4\text{-}4)$$

where R^* represents the effective radius. The derived effective diameters, $D^* = 2R^*$, for various physical QD diameters are shown in Figure 4-2. The results revealed that the strain-relaxation-induced potential valley, as illustrated in the upper panel of Figure 4-2, enhanced the lateral confinement. For physical QD diameters larger than 10 nm, the effective diameters are always smaller than the physical diameters. Higher indium composition leads to smaller effective diameter because the potential valley is deeper. Moreover, it can be clearly seen that 20 ~ 30-nm QD diameters are the most ideal because they can be reliably patterned by the e-beam lithography and maintain small effective diameters. Moreover, the carriers can be kept away from the etched sidewall, and the probability of nonradiative recombination can therefore be reduced. As the physical diameter is decreased to 10 nm or even smaller, there is only a small amount of strain remaining in the QDs, and the physical diameters start to dominate. Meanwhile, strong nonradiative recombination is expected to occur for sub-10-nm diameters since there is no potential barriers between the carriers and surface states.

In addition to the confinement due to strain-induced potential, strong Coulomb repulsion between electron-electron and hole-hole increases the energy of multi-exciton

states and makes them less favorable. The anomalous negative biexciton binding energy, $E_{xx}^{b} = E_x - E_{xx}$ has been investigated and attributed to the piezoelectric field [89], which forces electrons (holes) to pile up at one side of the InGaN/GaN interfaces and enhances the Coulomb repulsion energy. The negative biexciton binding energy has also been observed from our top-down QDs [68]. Furthermore, since the multi-exciton states possess higher energy, they can hop to surface states more easily and exhibited lower QE compared to excitons. Such behavior can favor single photon emission from the exciton state and has been discussed in detail previously [90].

Table 4-1. Bulk Bohr radii of common III-V semiconductor materials.

	AlN	GaN	InN	InAs	GaAs
a_B (nm)	1.2	2.1	7.1	34	15

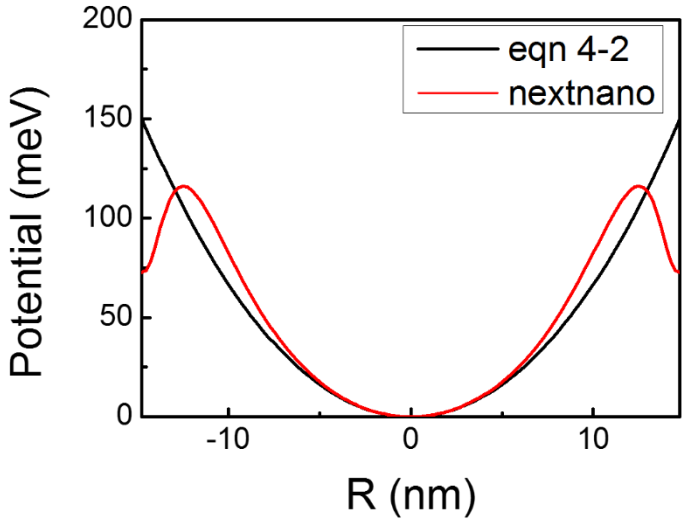

Figure 4-1. Strain-relaxation-induced potential profile of a 30-nm $In_{0.15}Ga_{0.85}N$ QD along the radial direction. The nextnano modeling results (red curve) indicates a decrease of potential energy at the edge owing to the decrease of InGaN band gap (deformation potential) as the compressive strain was relaxed at the edge. It was not considered in the analytical model.

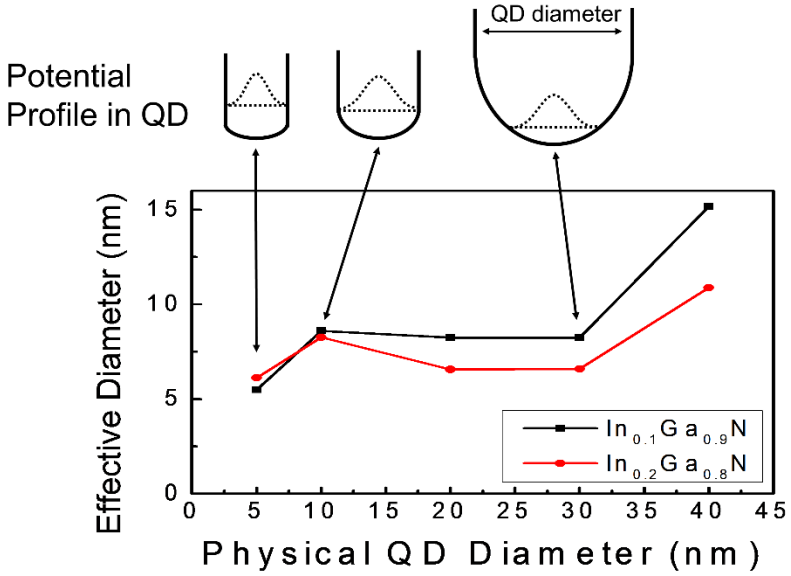

Figure 4-2. Effective diameters derived from ΔE_r, using the particle-in-a-circular-box model. The schematic illustration of lateral potential profiles in QDs of different sizes is also shown in the upper panel. The dotted lines represent the 1st energy states and the wavefunctions. The left schematic shows that the confinement is due to the infinite barrier at the QD sidewall when D < 10 nm; the middle schematic represents the case when the effective diameter was equal to the physical diameter when D ~ 10 nm; the

right schematic shows the confinement by the strain-induced potential valley when D > 10 nm. Please note that the effective diameter was larger than the physical diameter at D = 5 nm because the concave potential profile lowered the ΔE_r and lead to D^* slightly larger than D.

4.2 Polarized Single Photons by Semiconductor QDs

On-demand single photon sources play a key role in quantum science and technologies [91]. Advances in materials synthesis in recent years have led to a variety of potential candidates for single photon sources with properties suitable for practical applications including room temperature operation [92,93,42], high repetition rate [42,94,95,96], low time jittering [96,97], electrical operation [31,92,94,96,98], and chip-scale platform [35]. In these applications, the ability to control and modulate the polarization of each output photon from single photon sources is crucial to be able to encode information [91,99,100]. Moreover, the control of the single photon polarization will be beneficial for photonic circuit optimization and useful for single photon sources coupled to external structures such as photonic crystal cavities and plasmonic waveguides in which the coupling is often polarization-sensitive [99,101,102,103,104,105]. A single photon source with a programmable polarization state can eliminate the need of external polarization optics to reduce the system complexity and preserve the brightness of the single photon output.

The polarization properties of QD emission are determined by the symmetry of

the electron and hole wavefunctions in the excitonic state. For QDs grown along the [001] or [0001] direction of the zinc-blend or wurtzite lattice as in most cases, the heavy-hole wavefunction possesses an axial symmetry around the growth direction [106]. As a result, excitonic emission involving the pure heavy-hole state, e.g. in a compressively strained QD with symmetric in-plane strain field, generates un-polarized photons. The polarization control from self-assembled QDs is generally difficult due to the complex interaction of the substrate, growth conditions, and growth mechanisms although a limited degree of control has been shown utilizing the underlying crystal symmetry of the substrate [107,108,109]. To generate a deterministic polarization state, one can break the symmetry by modifying the photon local density of states (LDOS) [99,101,110,111] or introducing deterministically asymmetric strain fields to the QDs [48,112,113]. However, the number of polarization states that can be generated by LDOS engineering can be very limited and the effectiveness highly depends on the underlying crystal symmetry, QD geometry, and the quality of complicated cavity structures. The use of asymmetric strain fields can alleviate some of these constraints. The strain field can be modified by a mechanical force such as from a piezoelectric actuator [48] or by changing the QD geometry [112,113]. Quantum dots have previously been fabricated at the tips of pyramidal structures that were pre-strained along a specific direction to intrinsically control the photon polarization [112]. But the

large pyramidal structure can potentially make it difficult to integrate with other photonic structures such as optical cavities. Moreover, the degree of control for the polarization direction is still limited by the crystal symmetry with this approach. For example, QDs grown on hexagonal pyramids will not be able to generate both 0 and 45º polarizations on the same chip.

The other consideration for the polarization property of QD emission is the degree of linear polarization (DLP) which measures how pure the photon polarization state is. When the strain field and/or the quantum confinement become asymmetric, valence band mixing occurs. The strength of valance band mixing is determined by the degree of anisotropy and the energy differences between different valance bands. The energy differences between valance bands are governed by material properties, such as deformation potential, spin-orbit interaction, and crystal-field splitting if it is wurtzite structure [106]. For strained wurtzite crystals, such as group III-nitride semiconductors, the weak spin-orbital interaction, E_{so}, leads to a small energy splitting between heavy-hole and light-hole bands (or A and B valance bands) and strong valance band mixing [114,115]. As a result, single photon emission with a high DLP has been reported in group-III nitride QDs [114,115,116,117,118,119].

4.3 Elliptical InGaN QDs by Top-Down Approach

In this work, we overcame the limitations on polarization control described above by using a top-down approach, which enabled us to precisely control the QD geometry and the symmetry of the strain field. Using elliptical group-III nitride QDs, we were able to show single photon generation in an arbitrarily pre-programmed polarization state. The elliptical geometry allowed asymmetric lateral quantum confinement and asymmetric strain relaxation via free surface at the sidewall. Both anisotropy in quantum confinement and strain resulted in mixing between valance band states and changing the composition of hole states [114]. As a result, the 1st hole state generates emission polarization along the elongated axis. In our experiment, we attributed anisotropic strain relaxation as the dominant cause given the relatively large size of the QDs and hence weak in-plane quantum confinement. In other words, the anisotropy of in-plane strain, $\varepsilon_{xx} - \varepsilon_{yy}$, affected the degree of polarization as it appears in the off-diagonal term of valance band Hamiltonian [114], and $\varepsilon_{xx} + \varepsilon_{yy}$ determined the emission wavelength as it leads to piezoelectric field and QCSE. One example of the elliptical QD and its anisotropic strain distribution is shown in Figure 4-3. The degree of linear polarization was also influenced by the energy separation between the valance bands because it determined the strength of valance band mixing and was closely related to the spin-orbit interaction energy E_{so} for a wurtzite lattice structure [114]. The

E_{so} was estimated to be 15.7 meV in the $In_{0.11}Ga_{0.89}N$ material, and such small E_{so} compared to other semiconductor QD systems implied more effective valance band mixing and superior degree of polarization. In our experiments, the measured DLP exceeded 0.9 for QDs exhibiting high lateral aspect ratios, making these photons a suitable candidate for qubits without the need for external polarization optics. Compared to QDs fabricated from a bottom-up approach, the top-down approach adopted in this work offered unprecedented control over the QD properties including positions and emission wavelengths. The lack of wetting layers for the top-down QDs can also reduce the background noise in single-photon emission [113].

Disk-shaped InGaN QDs with GaN barriers were used in this study. Compared to binary GaN QDs, the use of InGaN alloys shifts the emission wavelength from ultraviolet to visible and improves the sensitivity of single photon detection with silicon based avalanche photodiodes. Elliptical QD geometry was achieved using a lithography and etching process [120]. A sample consisting of a single unintentionally-doped (uid) $In_{0.11}Ga_{0.89}N$ quantum well and a uid 10-nm GaN barrier layer was epitaxially grown on a 3-µm thick GaN template on c-plane sapphire using metal-organic chemical vapor deposition. The sample was then patterned by electron-beam lithography (JEOL JBX-6300FS) using the 950-PMMA A2 photoresist (PR). After PR development, chromium was deposited by e-beam evaporator (Enerjet Evaporator) and lifted off. Inductively-

coupled plasma reactive ion etching (ICP-RIE) using LAM9400 with Cl_2 and Ar was employed to form GaN nanopillars with one InGaN QD embedded in each nanopillar. No indium clustering was found in the InGaN region from the atom-probe tomography [121]. The optical properties of the top-down QDs have been studied before and reported elsewhere [87, 90]. Single photon emission has been observed up to 90 K in as-etched and unpassivated InGaN/GaN QDs fabricated using the same method thanks to the large exciton binding energy and low surface recombination velocity [122].

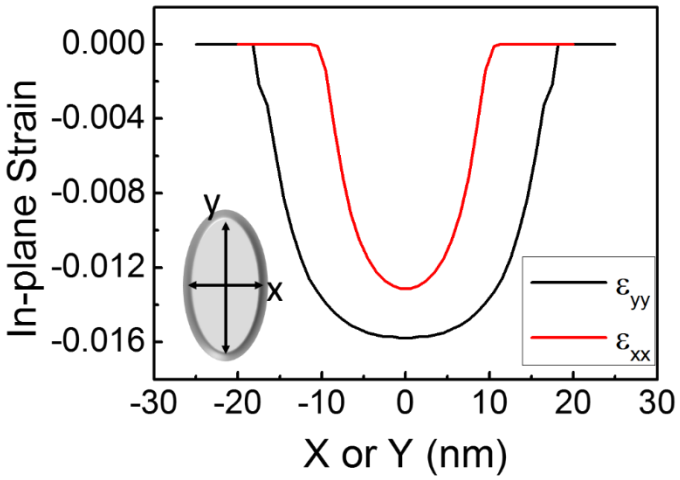

Figure 4-3. ε_{xx} and ε_{yy} along the x and y axis for a 22-nm × 36-nm elliptical InGaN QD. The strain was anisotropic ($\varepsilon_{yy} < \varepsilon_{xx}$) because the strain was more relaxed along the short axis. The difference in ε_{xx} and ε_{yy} lead to valence band mixing and preferential emission polarization.

4.4 Valence Band Mixing by Anisotropic Strain

As the QD structure is etched, strain relaxation is expected and an elliptical QD shape leads to an asymmetric strain field inside the QD. To compare the optical

properties of elliptical InGaN QDs among different materials, numerical simulations were performed using nextnano [123] software and parameters in Table 2-1. The valence band and conduction band states were simulated based on the 6×6 k·p model and the single-band Schrödinger equation, respectively. The strain-involved Hamiltonian was solved in p_x, p_y, and p_z basis, denoted as |X>, |Y>, and |Z>. After the envelope functions associated with |X>, |Y>, |Z>, and the electron state |S> were solved, the matrix elements associated with x, y, and z polarizations were derived using the following equations [124]:

$$\text{x-polarized: } |M_x|^2 = |\langle \Psi_e | p_x | \Psi_h \rangle|^2 \cong |\langle \mathrm{S} | p_x | X \rangle|^2 \left| \langle \varphi_e | \varphi_{h,x} \rangle \right|^2$$

$$\text{y-polarized: } \left|M_y\right|^2 = \left| \langle \Psi_e | p_y | \Psi_h \rangle \right|^2 \cong \left| \langle \mathrm{S} | p_y | Y \rangle \right|^2 \left| \langle \varphi_e | \varphi_{h,y} \rangle \right|^2$$

$$\text{z-polarized: } |M_z|^2 = |\langle \Psi_e | p_z | \Psi_h \rangle|^2 \cong |\langle \mathrm{S} | p_z | Z \rangle|^2 \left| \langle \varphi_e | \varphi_{h,z} \rangle \right|^2$$

where p_x, p_y, and p_z are momentum operators, $\mathrm{S}, \mathrm{X}, \mathrm{Y}, \text{and } \mathrm{Z}$ are the Bloch bases, φ_e and φ_h are the envelope functions of the electron and hole states respectively, and $\Psi_e = \varphi_e \cdot S$ and $\Psi_h = \varphi_{h,x} \cdot \mathrm{X} + \varphi_{h,y} \cdot \mathrm{Y} + \varphi_{h,z} \cdot \mathrm{Z}$. Spin degeneracy and Coulomb interaction were not included in our simulations. The z axes were assumed to be the [0001] and [001] directions for wurtzite and zinc-blende QD materials, respectively. Material parameters were taken from Refs. 125, 126, 127, and 128. The DLP was determined by:

$$\mathrm{DLP} = \frac{\left|M_y\right|^2 - |M_x|^2}{\left|M_y\right|^2 + |M_x|^2}$$

Figure 4-4 compares the calculated DLP for different QD materials. As expected, InGaN/GaN exhibits higher DLP than other QD materials because of small energy splitting between heavy-hole and light-hole bands. For the simulated QD structure, the energy splitting is 18 meV for InGaN at the Γ point while it is 71 meV for InP and even larger for others. A near unity DLP is possible for elliptical InGaN/GaN QDs with a high lateral aspect ratio.

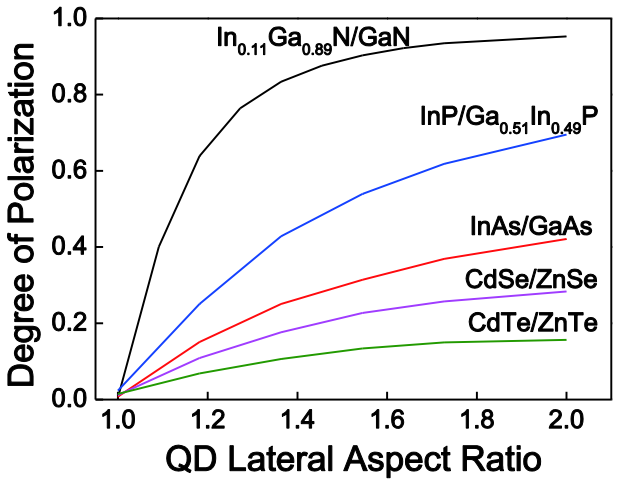

Figure 4-4. The calculated degree of polarization (DLP) of elliptical QDs for a variety of different semiconductors as a function of QD lateral aspect ratio which is defined as the length ratio between the long and short axes. The short axis is fixed at a constant 22 nm which is the same as the short axis length of QDs used in experiments in this work. The QD and barrier materials are given in the graph.

4.5 Polarization Properties of Elliptical InGaN QDs

To study the relationship between the QD geometry and emission polarization in experiments, elliptical QDs with different dimensions, lateral aspect ratios, and

orientations were patterned. Two QD-QD spacing, 300 nm and 5 μm, were used to enable ensemble and single-dot measurements, respectively. The top-view scanning electron micrograph of as-fabricated elliptical InGaN QDs embedded in GaN nanopillars is shown in Figure 4-5 for four different QD orientations, 45º apart. The dimensions of the InGaN QDs were inferred from the diameters at the top of the GaN nanopillars and the sidewall slanting angle as illustrated in Figure 4-5(a).

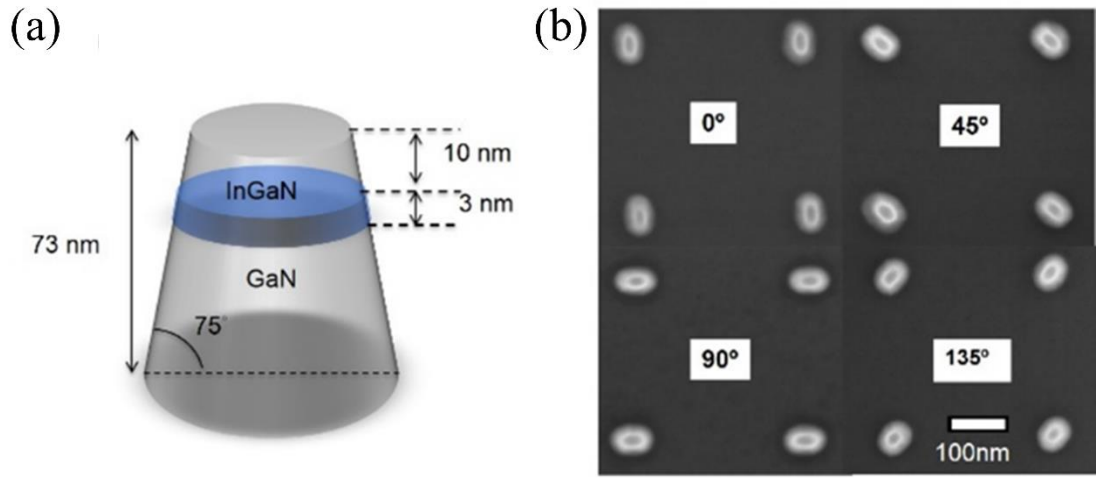

Figure 4-5. (a) The schematic of the elliptical QD synthesized by a top-down process. The disk-shaped InGaN QD is sandwiched by GaN barrier materials. (b) The top-view scanning electron micrographs of four different QD orientations: 0º, 45º, 90º, and 135º.

The polarization properties of QD emission were measured by polarization-resolved micro-photoluminescence (μ-PL). A 390-nm wavelength femtosecond mode-locked laser with 80-MHz repetition rate and 150-fs pulse duration was used as the excitation source. It had an incident angle ~ 50° from the normal direction of sample surface, and the spot size was ~ 40 μm in diameter. A pair of confocal lenses and a

pinhole were inserted when single QD measurement was carried out. The pinhole allowed spatial selection of a circular area with a 0.8-μm diameter. The spectral resolution was 0.1 nm at 400-nm wavelength. The combination of a rotating half wave plate and a fixed linear polarizer was used to resolve the spectra at different polarization angles. The second-order photon correlation ($g^{(2)}$) was measured using a Hanbury Brown-Twiss interferometer. All measurements were performed at 10 K. The detailed description of μ-PL setup and the numerical fitting model for $g^{(2)}$ can be found in Ref. 68.

Figure 4-6(a) and (b) show the polarization-resolved emission spectra of two QDs (QD A and QD B) at different polarization angles and the polar plots of normalized integrated PL intensity. The two QDs were designed to have orientations orthogonal to each other. The zero-degree, orientation of QD A, was chosen arbitrarily and not aligned to any particular crystal plane. The excitation intensity was 102 W/cm^2. The designed dimensions of both QDs were 22 nm by 36 nm for their short and long axes, respectively with a lateral aspect ratio of 1.64. The spectra revealed a highly polarized exciton emission peak at 2.979 and 2.958 eV for QD A and B respectively and an optical-phonon peak of which the energy was ~ 90 meV lower than the exciton peak [129]. The exciton emission peak was selected for polarization analysis. The photon polarization and DLPs from QD A and B were obtained using the fitted polar plots. With a 95%

confidence interval, the photon polarizations were determined to be -0.8° ± 1.9° and 98.7° ± 4.5° for QD A and B respectively; the DLP ranges were determined to be from 0.83 to 0.98 and 0.80 to 1.00 for QD A and B, respectively. The polarized intensity of QD B showed more deviation from the fitting curve because the emission intensity from QD B fluctuated during the measurement. Photon antibunching was confirmed from both QDs as shown in Figure 4-6(c). While the measurement was done with pulsed laser excitation, the long carrier lifetime due to built-in polarization field lead to significant overlap between neighboring peaks in $g^{(2)}$ plots [68]. In addition, the bi-exciton emission peaks can not be well resolved and separated from exciton peaks given that the linewidth was comparable to the energy difference between exciton and bi-exciton [130]. The peak overlap and possible bi-exciton emission were accounted for in the $g^{(2)}$ fitting model attributed to the dark current of the detector [68]. The fitting rendered $g^{(2)}(0) = 0.26$ for QD A and 0.32 for QD B without subtracting any background. The non-zero $g^{(2)}(0)$ values were accounted by coincidence counts involving detector's dark noise and bi-exciton emission [68].

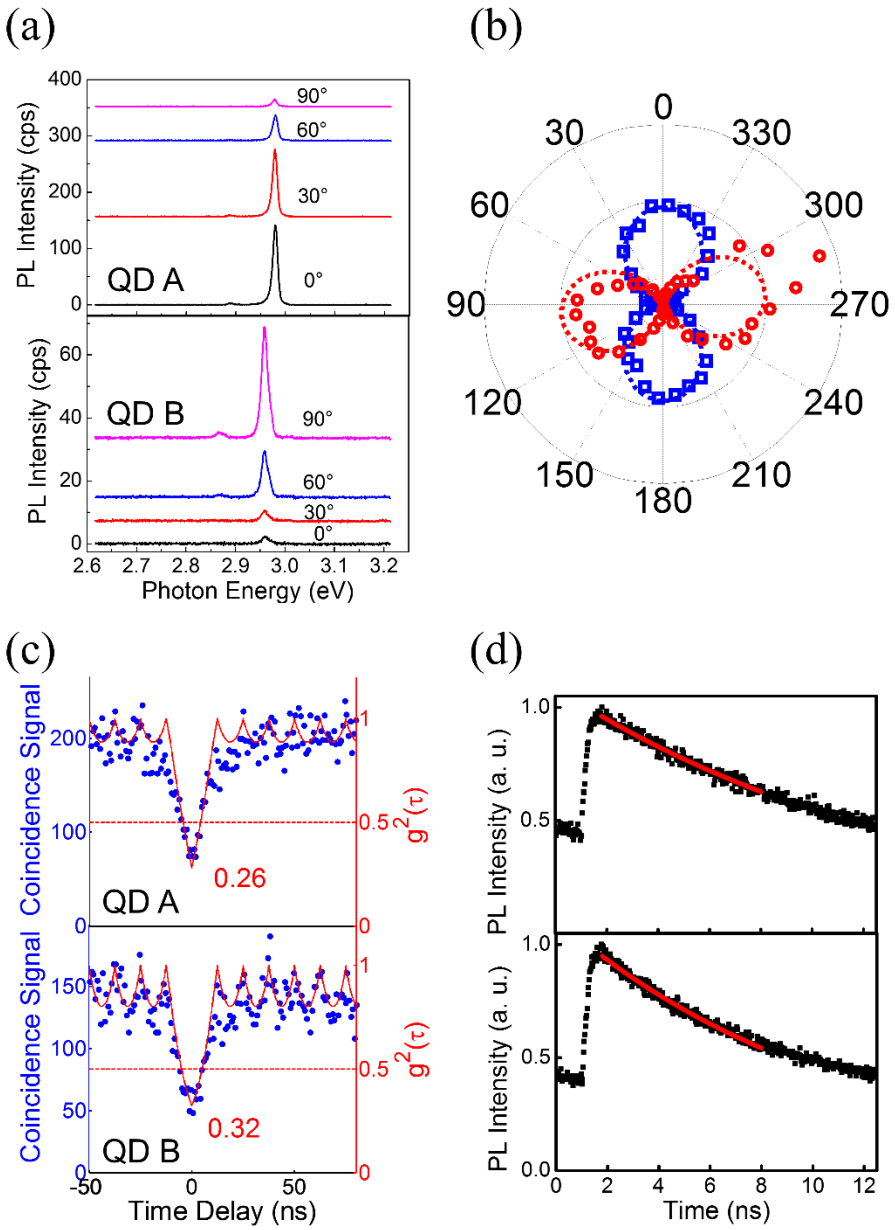

Figure 4-6. (a) Polarized PL spectra from QD A and B at various polarization angles. (b) Polar plots of normalized PL intensity of QD A (blue) and B (red) and the corresponding fitting curves (dotted lines) using $I_{min}+(I_{max}-I_{min})\cos^2(\theta-\theta_{ref})$ where θ_{ref} was the fitted polarization angle. The degree of polarization (DLP) was calculated based on $(I_{max}-I_{min})/(I_{max}+I_{min})$ from the fitting curves. (c) $g^{(2)}(\tau)$ of QD A and B subjected to 102 W/cm^2 of excitation intensity. The peaks shown in the $g^{(2)}$ data are noisy due to the long QD lifetime which was comparable to the laser repetition time of 12.5 ns. The $g^{(2)}$ fitting rendered lifetime values 13.7 ± 3.45 ns and 9.3 ± 1.25 ns for QD A and B respectively. (d) Time-resolved PL and the fitting (red curves) resulted in 14.6 ± 0.46 ns and 11.1 ± 0.42 ns lifetime.

Figure 4-7 summarizes the polarization angle and DLP measured from both QD arrays (Figure 4-7(a)) and individual QDs (Figure 4-7(b)). In the QD array measurements, the laser excitation beam covered about 10^4 QDs. In the single-dot measurements, a total of 60 QDs were randomly selected from five different QD orientations. The results showed a good correlation between the polarization angle and the QD orientation although there was a 13º standard deviation in the polarization angle from the single-dot measurements. The measured polarization direction of QD ensembles showed good correlation with the designed QD orientation. The DLP is primarily determined by the QD lateral aspect ratio. All QDs were designed with the same lateral aspect ratio of 1.64 although processing variations can cause the aspect ratio to deviate from the design. The SEM measurements showed the resulting lateral aspect ratio had a standard deviation of 0.25. This, in combination with inhomogeneity of QD shape, resulted in a lower DLP (0.60 ± 0.05) observed for the QD arrays than the DLP for individual QDs (0.72 ± 0.17).

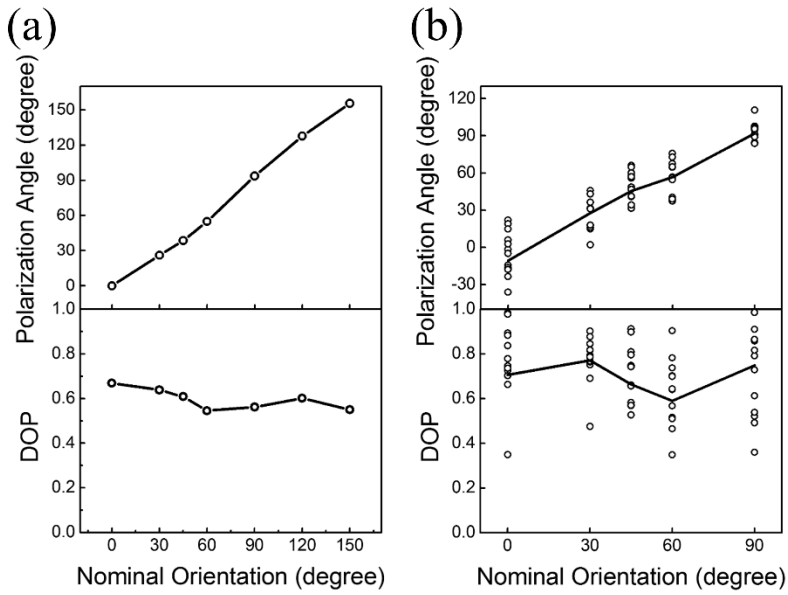

Figure 4-7. The measured polarization angle and DLP as a function of the designed QD orientation angle: (a) and (b) correspond to measurements of QD arrays and individual QDs, respectively. In (b), twelve QDs were randomly selected from each QD array of a specific orientation angle, and the solid curve corresponds to the median values of polarization angles and DLPs for each QD orientation angle. In calculating DLP of QD ensembles, we considered polarized intensity at photon energy higher than 2.85 eV to avoid contamination signals from unetched InGaN regions, which can be resulted from metal debris left on the sample surface after lift-off. For single QD calculation, we considered the intensity within the full-width-at-half-maximum of single QD emission peaks.

Another observation made throughout the measurements (e.g. the data shown in Figure 4-7) was that there was not a single orientation angle of the QD that showed a significantly higher DLP. Given that the orientations of elliptical QDs were not intentionally aligned to any crystal orientation, the similar DLP values for different orientations suggested that the polarization properties were not sensitive to the underlying crystal symmetry. If it were the case, QDs oriented along 45º and 135º would express slightly different properties than QDs oriented along 30º and 60º in Figure 4-7(a)

due to the six-fold symmetry of the wurtzite lattice on the c-plane. Furthermore, in comparison to another set of data points from a different sample, we did not observe a systematic dependence of the polarization angle fluctuation or DLP variation on the QD orientation. Since the polarization of InGaN QDs is highly sensitive to QD geometry, the variation of DLP and polarization angle can be easily generated by sample fabrication errors. In addition, from single-dot measurements (Figure 4-7(b)), the average photon energies and the standard deviation at different QD orientations were 2.979 ± 0.024, 2.968 ± 0.019, 2.971 ± 0.015, 2.971 ± 0.044, 2.968 ± 0.033 eV for 0º, 30º, 45º, 60º, 90º, respectively. The spectral linewidths were 17 ± 5, 22 ± 8, 18 ± 6, 19 ± 6, 21 ± 7 meV for 0º, 30º, 45º, 60º, 90º, respectively. There was no systematic dependence of the spectral properties of QDs on their orientations. Such result implied that the spectral and polarization properties of elliptical InGaN QDs are independent of QD orientation due to the highly symmetric nature of c-plane in the wurtzite lattice, and we can generate any arbitrary polarization angle with a high DLP from the top-down elliptical QDs on one single chip without any of the existing limitations in some of the bottom-up approaches [112]. Besides, we have not observed an obvious dependence of DLP on the excitation power up to 250 W/cm^2 nor any influence on the polarization properties of the QD emission from the linear polarization of 390-nm pump laser, which was along the 0° direction.

To further understand the correlation between QD geometry and DLP and the origin of variations, we carried out SEM to characterize the actual geometry of seven QDs for which we also did polarization measurements. In this way, we were able to precisely investigate the QD geometry and the resultant DLP and compare the experimental and theoretical DLP values, as shown in Figure 4-8. The seven QDs were from the same array, having the same nominal lateral aspect ratio of 1.64, but ended up with different geometry because of process variation. The measured DLP values agreed qualitatively with theoretical values, revealing that the theoretical model was accurate, and the polarization was caused by asymmetric strain and valence band mixing. For most experimental data points, the DLP values were lower than theoretical ones because of non-ideal strain relaxation and deviation of actual QD geometry from simulated elliptical shape. Moreover, to understand the QD geometry variation statistically, the true orientations and lateral aspect ratios of 80 QDs were analyzed by SEM. The 80 QDs were designed to have the same nominal lateral aspect ratio, 1.64, but ended up having slightly different geometry because of process variation. The standard deviation of QD lateral aspect ratio was found to be 0.25. This corresponds to 0.16 standard deviation in DLP according to Figure 4-8. Figure 4-9(a) shows an example of a QD exhibiting a near circular shape due to patterning errors. The variation in the DLP attributed to the variation in the QD lateral aspect ratio agreed well with the individual

QD measurement results shown in Figure 4-7(b). However, SEM images revealed 6° standard deviation in QD orientation, while the μ-PL measurement showed 13° standard deviation in the polarization angle. To further investigate the origin of this discrepancy, two QDs that showed obvious irregularity were singled out and measured for their optical properties. The SEM images of these two QDs are shown in Figure 4-9(b) and (c). It can be seen that these QDs exhibit orientations and shapes that deviate from the designed elliptical shape and direction. Compared to the QD in Figure 4-9(b), the QD in Figure 4-9(c) was oriented 17º clockwise. However, there was a 29º difference in the measured polarization angle between these two QDs. Therefore although the polarization angle mostly tracks the QD orientation, there are cases this tracking fails. It is likely that the QD geometry, when deviated from the ideal elliptical shape, plays a role in shifting the polarization angle which is determined by the strain field in the InGaN region.

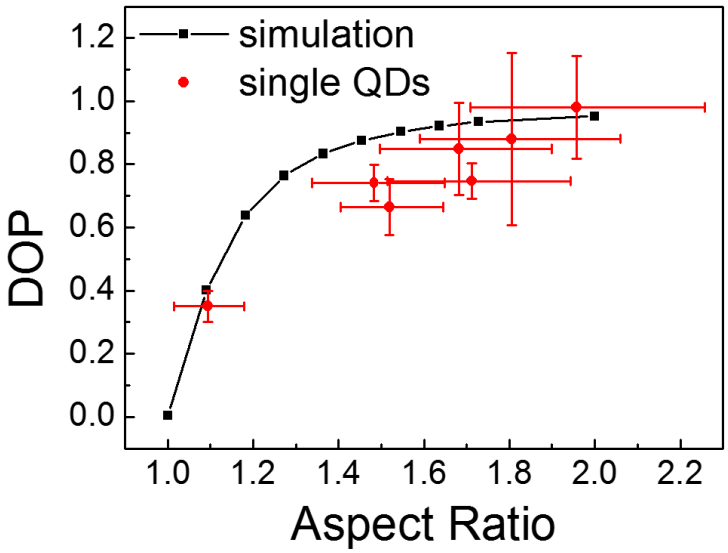

Figure 4-8. The comparison of the calculated and measured DLP as a function of the $In_{0.11}Ga_{0.89}N$/GaN QD lateral aspect ratio. The lateral aspect ratio of each QD was characterized by SEM, and the lateral error bars corresponded to the uncertainty in measuring the length of long and short axis in SEM image, which was ~ ± 1.5 nm. The vertical error bars correspond to the errors of DLP fitting.

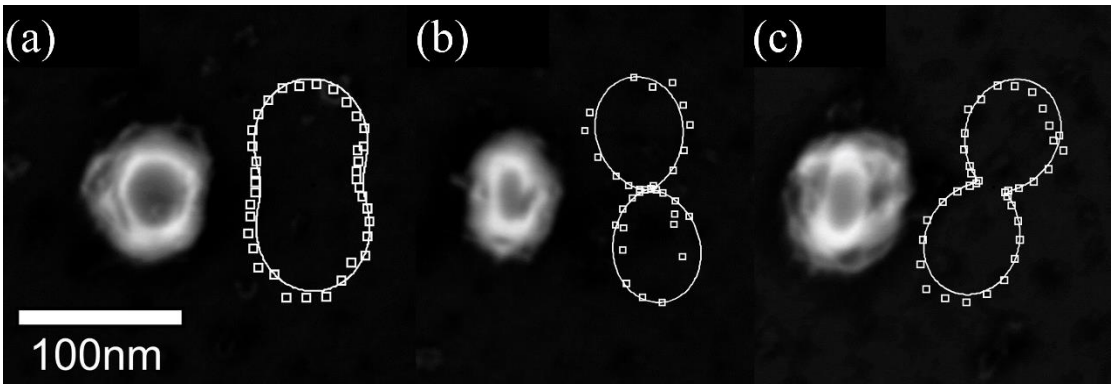

Figure 4-9. The top-view SEM images and the polar plots of the polarization properties of three QDs exhibiting irregular orientations or/and shapes compared to the designed parameters due to patterning variations. The SEM images are more blurry compared to those shown in Figure 2(b) because the chromium etch masks have been removed before imaging was performed in this figure in order to reveal the true shape of the top surface of the nanopillar. The contrast was hence very poor. (a) shows a QD whose shape has become almost circular and (b) and (c) show two QDs with orientations deviated from design. All three QDs were designed to be 22 nm (36 nm) for their short (long) axes and oriented along 0º, which corresponds to the vertical direction in the image. They ended up with different geometry because of process errors.

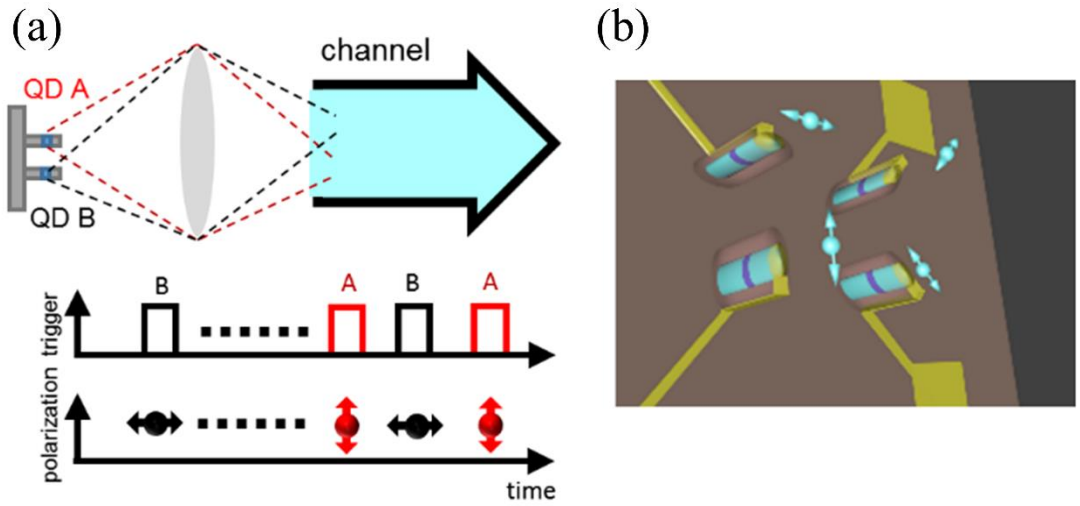

Figure 4-10. (a) Schematic illustration of a polarization control scheme that includes two elliptical QDs with orthogonal orientations. By controlling trigger signals of the two QDs individually, single photons with orthogonal polarizations can be generated and coupled to the communication channel by a lens. (b) Schematic illustration of 4 elliptical QD single photon emitters generating 4 different polarizations as 2 basis sets for polarization encoding. QDs are embedded in nanopillars that are coated with an insulating layer. The top surface of the nanopillars are in contact with top electrodes. Bottom electrodes are not shown in the graph.

4.6 Conclusion

In summary, site-controlled elliptical InGaN QDs were fabricated and polarized single photon emission was observed. The polarization direction is completely controlled by the orientation of the QD and is insensitive to the underlying crystal symmetry. The DLP is high and can approach unity when the QD lateral aspect ratio is close to two. Polarization properties from both QD arrays and individual QDs were analyzed. Excellent correlations between the QD geometry and the polarization property were found. The measured DLP agreed well with theoretical models. Deviation of the polarization direction from the nominal QD orientation has been

largely attributed to patterning errors originating from lithography and etching. The top-down approach offered an unprecedented degree of control over the QD position and emission wavelength not easily attainable from a bottom-up approach. Because the polarization control is an intrinsic property of the elliptical QD without the assistance of any external structures, multiple QDs of different polarizations can be placed in close proximity. Electrically driven single photon devices can also be readily made with proper planarization and metal contacts [131]. It allows each QD to be individually addressable and enables the control of output polarization. Figure 4-10(a) illustrates a simple scheme to produce a stream of single photons with orthogonal polarizations by individually triggering two elliptical QDs, such as QD A and B in Figure 3, and coupling the single photons into a single communication channel. Figure 4-10(b) shows a potential design for an electrically driven quantum-key-distribution (QKD) transmitter. It consists of four elliptical QDs generating 0º, 45º, 90º, and 135º polarizations as two orthogonal bases for the polarization encoding following the BB84 protocol [21]. The proximity of these QDs can also greatly simplify the coupling of the QD output to a single communication channel, and the output polarization can be programmed by individually operating each emitter. The security concern arising from wavelength inhomogeneity of these four QDs can be addressed by, for example, randomizing the emission wavelength slightly by applying electrical pulses or placing heating pads

nearby.

Chapter 5

Fundamental Limit of InGaN QD Inhomogeneity Caused by Random Alloy and Well-Width Fluctuations

In alloy systems, when there are multiple kinds of cation or anion atoms present in the system, the local alloy composition can fluctuate even if the material forms a perfect single crystal without any defect. This is because the distribution of different cation (anion) atoms is not uniform at the atomic scale. The probability of a particular type of cation (anion) atoms to occupy a lattice site is simply equal to its mean fraction in the material. This is called the random alloy fluctuation. Being a ternary alloy, InGaN material is no exception. Indium atoms occupy cation sites, but there is no restriction on which cation sites in the unit cell should be indium atoms. In this Chapter, we will

discuss the impact of random alloy effect on InGaN LED and QDs and our endeavor of random alloy simulation, aiming to shed light on the intrinsic inhomogeneity of ternary alloy QDs. In addition, we will also discuss well-width fluctuation, which is caused by the non-uniformity of QW epitaxy growth.

5.1 Random Alloy Fluctuation in InGaN

A lot of material characterizations have been done and revealed that epitaxially grown InGaN, as a ternary alloy, is nonuniform at the atomic scale, and the distribution of indium atoms follows the binomial distribution as a result of random indium atoms in group-III atom sites[132,133]. The binomial distribution is described by the equation below:

$$P(n, N, p) = \frac{N!}{n!(N-n)!} p^n (1-p)^{N-n}, \quad (5\text{-}1)$$

where n is the number of indium atoms, N is the total number of III-atom sites, and p is the probability of having indium atoms at a III-atom site. Aside from this random indium fluctuation caused by the nature of ternary alloys, there has been no evidence of indium clustering in InGaN epitaxy layers. However, the random alloy effect was often overlooked in theoretical analyses until recently. Theoretical modeling of random indium distributions in quantum wells suggested that the random alloy effect can lead to carrier localization [134] inhomogeneous broadening [135], efficiency droop

[136, 137], and reduced turn-on voltage [136,137] of LED devices. While the aforementioned reports were all about QW-based LED devices, in this study we focused the influence of random alloy effect on InGaN quantum dots (QDs). As InGaN QDs has been deemed as promising quantum light sources, understanding how random alloy effect impacts the optical properties of InGaN QDs is vital.

5.1.1 Atom Probe Tomography of InGaN

Among different material characterization techniques, atom probe tomography (APT) has been proven to be a powerful tool of analyzing material composition at the atomic scale [138]. Atom probe tomography of MOCVD-grown InGaN has been carried out and found that the indium atom distribution agreed with theoretical binomial distribution. For our study, we also performed atom probe tomography on the InGaN QW samples we used for QD fabrication. One example is shown in Figure 5-1. The variation of indium composition in the nanometer scale is clearly seen, and the histogram reveals that the distribution is indeed binomial. It proves that the indium distribution in our samples can be considered as random alloy, and the distribution of indium atoms is determined solely by the probability.

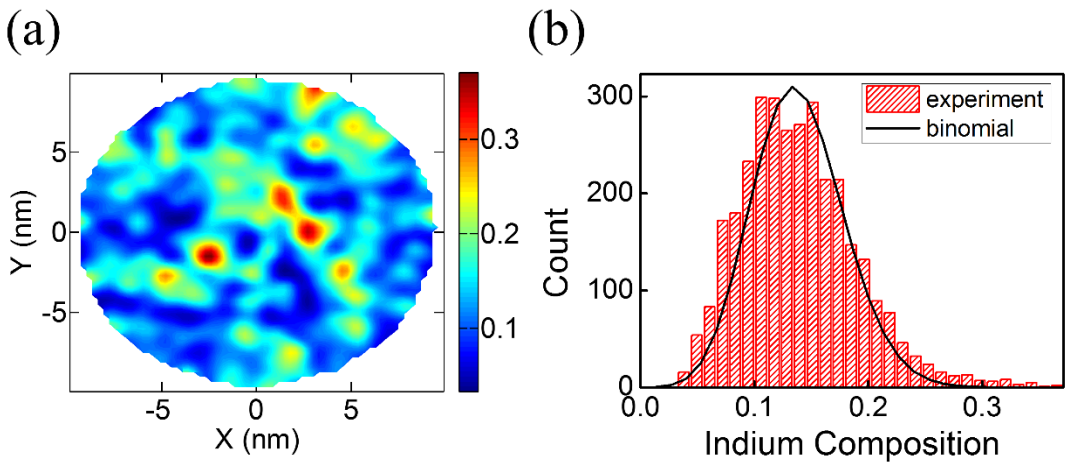

Figure 5-1. (a) Distribution of indium composition in an InGaN QW acquired by atom probe tomography. The bin size is 1.5 nm × 1.5 nm × 0.75 nm, which corresponds to 74 Ga or In atoms. (b) Histogram showing the number of data points having different In compositions. The theoretical binomial distribution with sample size, N=74, is also shown (black curve).

5.2 Well-Width Fluctuation of InGaN QW

Unlike the random alloy fluctuation, which is intrinsic to ternary alloys, well-width fluctuation is determined by the epitaxial growth technique and it can be potentially eliminated if the epitaxy is controlled perfectly. With modern MOCVD technology, 1-ML well-width fluctuation has been observed in MOCVD InGaN QW by atom probe tomography [133]. It has been shown that while the lower InGaN/GaN is flat, the upper interface is not. Plateaus that are 1 ML in height and 5 ~ 10 nm in lateral dimensions were found at the upper interface. Due to the built-in piezoelectric field in wurtzite InGaN QW, QW width significantly affects the photon energy and wavefunction overlap integral. Theoretical work has been performed to look into this issue and revealed that the 1-ML plateaus indeed can help localize electron

wavefunctions and affect the emission spectra [134,135]. Since our InGaN QDs were made from a MOCVD InGaN QW, the well-width fluctuation can also contribute to part of the inhomogeneity.

5.3 Methodology of Numerical Modeling

In this section we introduce the methodology we used to model the random alloy and well-width fluctuation.

5.3.1 Random Alloy Fluctuation

To generate random indium distribution and mimic random alloy fluctuation, we used a random number generator to randomly assign indium atoms to different areas in the QD. First, we constructed a 3-D cubic grid and randomly assign indium atoms to grid points, as illustrated in Figure 5-2(a). The probability of having one indium atom on a grid point was equal to the nominal indium composition. Given that the indium composition was not a step function in the growth direction, the nominal indium composition was assumed to follow Gaussian distribution with $\sigma = 1.5$ nm, one half of the QW width [137]. The Gaussian distribution and the results from random number generator are shown in Figure 5-2(b). The averaged indium composition in the QW was 14% in order to match the photon energy observed in experiments and the indium

composition acquired from APT (Figure 5-1). Secondly, we averaged over 125 grid points to calculate the local indium composition and produce a smoother potential landscape. The as-generated random indium distribution is shown in Figure 5-2(c). Please note that the generated indium distribution had some small sharp features and was not as smooth as the APT data. This is because the APT data underwent a delocalization algorithm to compensate the uncertainty of atom positions, which smoothed out the indium distribution.

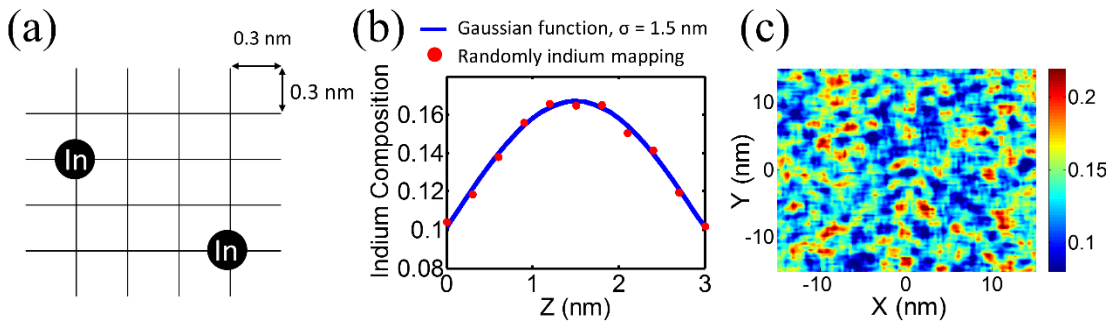

Figure 5-2. (a) Illustration of the grid representing atomic sites and the randomly assigned indium atoms. (b) The Gaussian distribution of indium composition in the 3-nm QW, and the mean indium composition at various Z position based on random number generator. (c) As-generated random indium distribution.

The simulated QD geometry was an axial InGaN nanodisk in a GaN nanowire. Such structure was common for various QD systems [139,140,141,142], and single photon emission has been observed [143,87], The diameter of nanowire used in the simulations was 30 nm, and the thickness of InGaN layer was 3 nm, as illustrated in Figure 5-3(a). The nanowire was surrounded by air to allow strain relaxation via the

sidewall free surface. The wavefunctions and energy states of conduction band and heavy-hole band were solved for 30 different indium distribution scenarios by semiconductor simulation software, nextnano^3, under the effective mass approximation [144]. Strain relaxation and piezoelectric field were included for potential profile calculation, and Coulomb interaction was considered for wavefunction and energy state calculation. Lattice and band parameters are listed in Table 2-1.

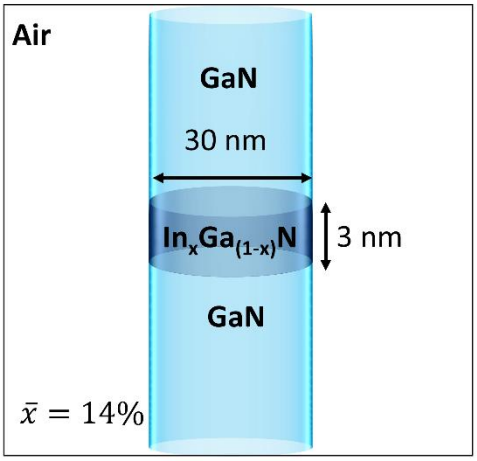

Figure 5-3. InGaN dot-in-wire geometry for numerical simulations.

5.3.2 Well-Width Fluctuation

Separate simulations were performed to investigate different well-width fluctuation configurations. 30 different well-width fluctuation configurations were created in the way similar to that described in 5.3.1. The indium composition was also assumed to be Gaussian in the Z direction and uniform in X and Y directions. We

considered ± 2 ML fluctuation and randomly assigned -2 ML, -1 ML, 0, 1 ML, or 2 ML fluctuation to each grid point at the upper InGaN/GaN interface [133]. We assumed that the fluctuation followed a normal distribution and σ_{WWF} = 2 ML, that is, the probability of 0, ±1 ML, and ±2 ML fluctuation corresponds to 38.2%, 15%, and 15.9% respectively, according to the normal distribution. Figure 5-4(a) shows one example of the randomly generated well-width fluctuation mapping. Experimental observations revealed that at the upper InGaN/GaN interface, the lateral dimension of each plateaus is 5 – 10 nm [133]. To smooth out the fluctuation as seen in Figure 5-4(a) and generate plateaus or recess of similar size, the well-width fluctuation at each grid point was averaged over 5-nm × 5-nm area. The averaging process resulted in a continuously varying values at each grid point, as shown in Figure 5-4(b). Since the well-width fluctuation was discretized and only 0, ±1 ML, and ±2 ML were allowed, the fluctuation values at grid points were sorted and assigned to be 0, ±1, or ±2 by setting proper thresholds so that they still followed the normal distribution. The final result (Figure 5-4(c)) was then used to construct the simulation input.

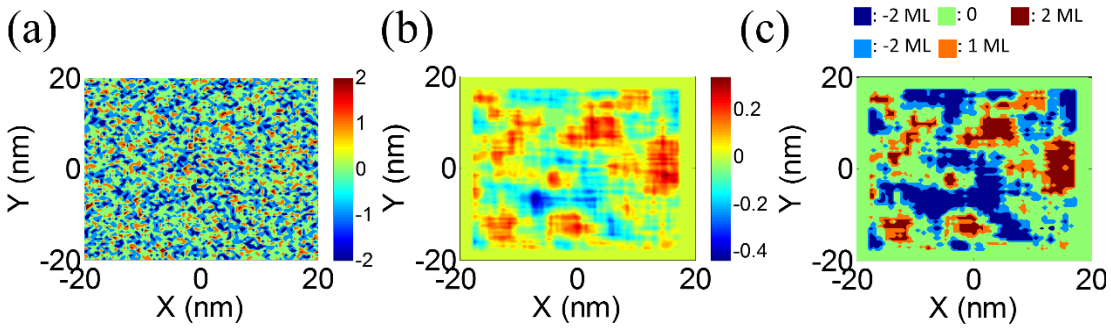

Figure 5-4. (a) Randomly assigned -2, -1, 0, 1, and 2 ML fluctuation to a square grid with grid size 0.5 nm. (b) Moving average of (a) over 5-nm × 5-nm area for each grid point. (c) Final results of the randomly generated well-width fluctuation by re-sorting data in (b) into discrete -2, -1, 0, 1, and 2 ML fluctuations.

5.4 Fundamental Inhomogeneity of Wurtzite InGaN QDs

In this section we discuss the inhomogeneity imposed by the random alloy fluctuation, well-width fluctuation, and possible diameter variation due to process errors. To simplify the discussion, we neglected the global indium fluctuation and well-width nonuniformity. That is, we assumed all QDs have identical mean indium composition and mean well-width. For our top-down QDs, the InGaN layer was grown by MOCVD. Although some concentric nonuniformity was expected across the entire wafer, since the measured single QDs were all made in a 30 μm × 30 μm area, it was reasonable to assume that the mean indium composition and well-width were uniform between the QDs.

5.4.1 Inhomogeneity due to Random Alloy Effects

To statistically study the intrinsic inhomogeneity imposed by random alloy

fluctuation, simulations based on 30 different randomly generated configurations were performed. The 1st electron and hole states were obtained by solving the Schroedinger equations of conduction band and heavy hole band separately under the effective mass approximation. Coulomb interaction between the electron and hole was also considered using the Hartree approximation. Figure 5-5(a) shows the histograms of calculated photon energy and also the experimental data acquired by single QD PL. The random alloy effect leads to $\bar{E}_{RA}$ = 2.8542 eV and ΔE_{RA} = 10.79 meV. The dash line in Figure 5-5(a) represents the photon energy, $\bar{E}_{ideal}$, 2.8682 eV, in the ideal case: the indium composition was uniform in the x-y plane but Gaussian in the z direction for fair comparison. For most cases, the presence of indium rich regions due to random alloy effect created local potential minimums in the QW and, hence, lowered the photon energy. In average, the random alloy effect lowered the photon energy by 14 meV. Only for very few cases, the mean indium composition was much lower than the nominal value 14%, and the photon energy turned out to be slightly higher even with random indium fluctuation. What's more important is the standard deviation, ΔE_{RA}. The random alloy fluctuation induced 10.79-meV variation in photon energy between QDs. It was a result of natural randomness in ternary alloy and the fundamental limit of inhomogeneity for wurtzite InGaN QDs.

In addition to photon energy, another important characteristics is the

recombination rate. According to the Fermi's golden rule, the radiative recombination rate is described by the equation:

$$\gamma_{rad} = \frac{n_{eff} e^2 E_{ex} P_{cv}^2}{2\pi m_0^2 \epsilon_0 \hbar^2 c^3} |\langle \varphi_e | \varphi_h \rangle|^2, \quad (5\text{-}2)$$

where n_{eff} is the effective refractive index and was assumed to be one since the nanopillars were surrounded by air; E_{ex} is the exciton energy; $P_{cv}^2/(2m_0)$ = 16.1 eV is the linear interpolation of the Kane energy of wurtzite GaN and InN [145]; $|\langle \varphi_e | \varphi_h \rangle|^2$ is the wavefunction overlap integral. Using equation 5-2 and the wavefunction overlap integral obtained from simulations, we were able to calculate the radiative recombination rate (Figure 5-6(b)). Moreover, our previous studies confirmed the existence of both radiative and nonradiative recombination for the top-down InGaN QDs even at 10 K [90]. The nonradiative recombination is attributed to the tunneling of exciton from the center of QDs to the sidewall. The tunneling rate is determined by the radial position of exciton, the potential barrier in between the exciton and QD sidewall, and the available recombination sites at the sidewall. Using the Wentzel-Kramers-Brillouin approximation, it can be described by the following equation [90]:

$$\gamma_{rnl} = \frac{c_1}{R} e^{-\frac{2\sqrt{2m}}{\hbar} \int \sqrt{\phi(r)} dr}, \quad (5\text{-}3)$$

where c_1 corresponds to the recombination probability at the sidewall; 1/R accounts for the surface-to-volume ratio; the exponential term represents the tunneling probability, and $\phi(r)$ describes the potential profile. For wurtzite InGaN QDs, strain relaxation

leads to a nonuniform piezoelectric field and a confinement potential in the radial direction, $\phi(r)$, which can be analytically expressed as [68]:

$$\phi(r) = B_m(1 - \mathrm{sech}(\kappa r)). \quad (5\text{-}4)$$

To estimate the the nonradiative recombination rate, we derived the radial position, r_{ex}, of the exciton using $\frac{\overline{r_e}m_e^* + \overline{r_h}m_h^*}{m_e^* + m_h^*}$, where $\bar{r}$ represents the expectation value of radial position. $\overline{r_e}$ and $\overline{r_h}$ are summarized in Figure 5-6(a). Figure 5-6(b) visualizes the distribution of $\overline{r_e}$ and $\overline{r_h}$ inside a 30-nm QD, represented by the blue circle. Plugging r_{ex} and parameters from Reference 90 into Equations 5-3 and 5-4, we calculated the nonradiative and radiative decay rate (Figure 5-6(c)). The total decay rate was the sum of radiative rate and nonradiative rate and compared with the experimental TRPL data in Figure 5-5(c). Despite that few QDs showed much faster decay rate in experiments, most of the experimental data agreed with the simulation results very well, indicating that most of the variation was caused by random alloy effect. Also, compared to uniform indium distribution (dash line in Figure 5-6(c)), random indium fluctuation leads to faster decay rate, meaning that although the piezoelectric field separates the electron and hole in the z-direction, they still tend to stay together in the lateral direction, and random alloy effect helps provide an even stronger confinement.

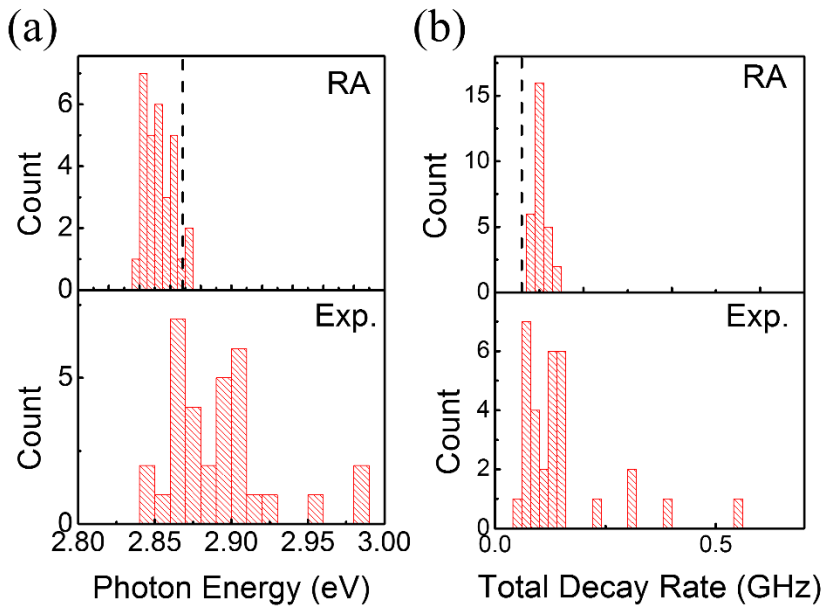

Figure 5-5. (a) Histograms of photon energy from experimentally measured single QDs (lower) and 30 simulated QDs random indium distribution (upper). (b) Histograms of total decay rate from TRPL and simulated random indium distribution. The dash lines represent the photon energy and total decay rate of uniform indium distribution, without random alloy effect.

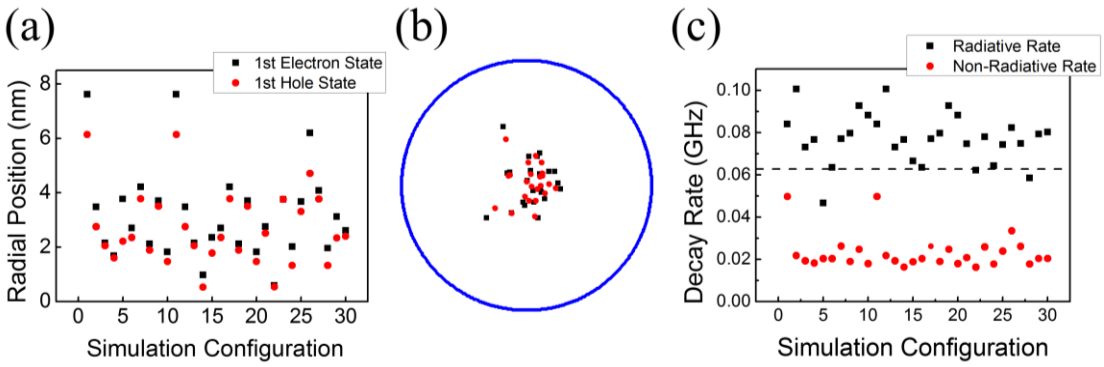

Figure 5-6. (a) Expectation values of the electron and hole radial positions of 30 simulated QDs with different indium fluctuations. (b) Visualization of (a) in a 30-nm QD (the blue circle). (c) The radiative and nonradiative decay rate of the 30 simulations. The dash line represents the radiative rate when the indium composition is uniform.

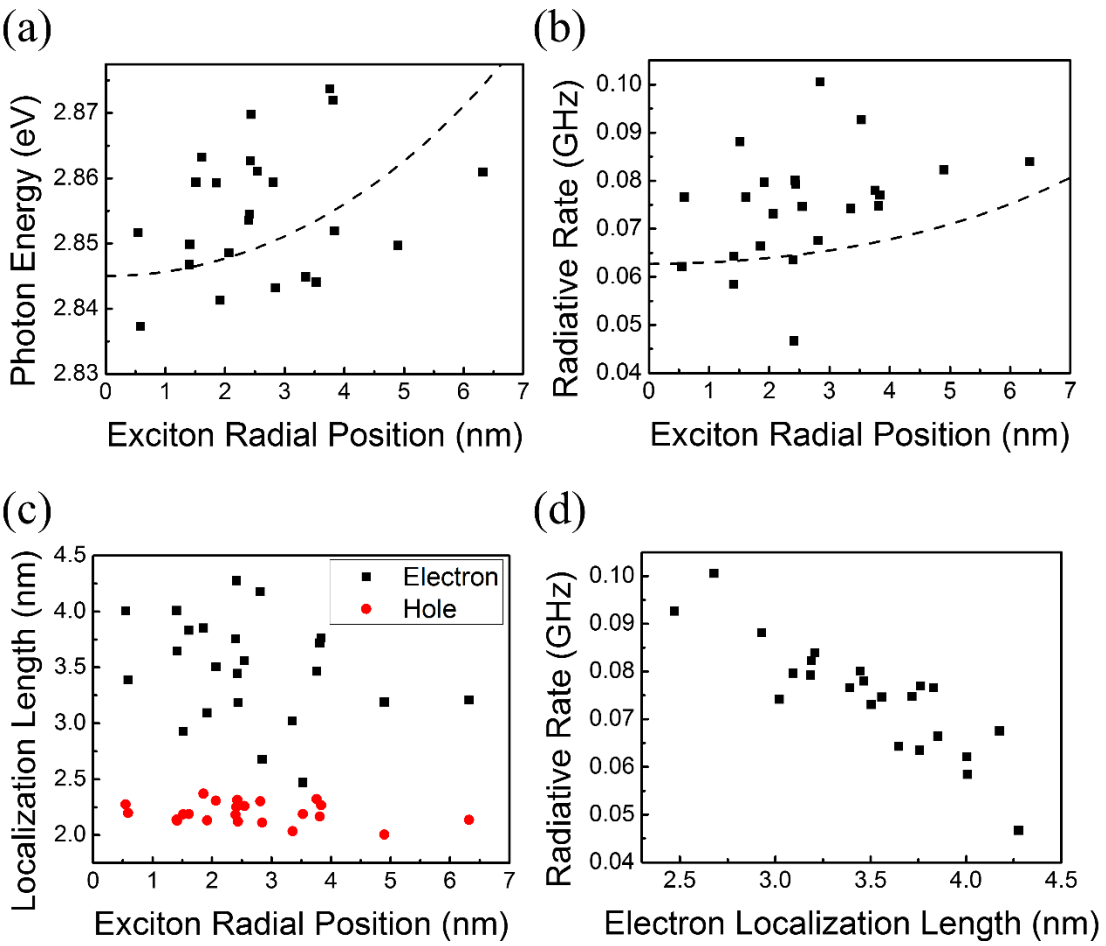

Figure 5-7. (a) and (b) Correlation between radiative decay rate, photon energy, and the radial position of excitons. The dash lines correspond to the photon energy and radiative rate at various radial positions derived based on the strain-induced potential profile. The dash line in (a) is intentionally offset to align with scattered data points for easy comparison. (c) The correlation between the carrier localization length and the radial positions. (d) The correlation between the radiative recombination rate and the localization length of the 1st electron state.

The strong bond between electron and hole can also be seen in Figure 5-6(a). For all simulations, regardless of the indium distribution, $\bar{r_e} - \bar{r_h}$ was found to be smaller than 2 nm because the electron and hole were always bonded. Moreover, since the electron has a smaller effective mass, and the band offset induced by the random alloy effect is larger in the conduction band, the electron is more sensitive to the indium

fluctuation, and the position $\overline{r_e}$ varies more. On the other hand, the hole is less affected by the indium fluctuation and is more likely to stay at the center of the QD. However, the Coulomb force is sufficiently strong that the hole is pulled toward the electron and, hence, $\overline{r_h}$ follows $\overline{r_e}$ as shown by all simulations. Another observation is that, for all 30 simulations $\overline{r_e}$ and $\overline{r_h}$ are less than 8 nm although the QD radius is 15 nm. This is due to the confinement provided by the strain relaxation and nonuniform piezoelectric field [68]. While the random alloy effect creates some indium-rich regions in the QD and modifies the potential landscape, the piezoelectric field at the center is still dominant and keeps the wavefunctions close to the center. It also helps suppress the tunneling assisted nonradiative rate (Figure 5-6(b)) even though the nanopillar sidewall has not been passivated in our experiments.

In addition, we studied the correlation between photon energy, radiative decay rate, and the position of excitons, as shown in Figure 5-7(a) and (b). The correlation between photon energy and exciton positions was the direct consequence of strain-relaxation-induced potential profile: lower (higher) potential at the center (edge) because of larger (smaller) strain and the corresponding piezoelectric field. The radiative decay rate and the exciton positions exhibit a correlation: a large r_{ex} suggests more wavefunction overlap as the piezoelectric field is weaker. The other factor that governs the radiative rate is the extent of the electron wavefunction. The hole wavefunction always shows a

smaller extent because of its heavier mass. When the electron wavefunction is also more localized, the wavefunction overlap integral increases. The degree of localization can be quantified by the localization length, which was calculated as follows:

$$(\Delta r)^2 = \int |(r - \langle r \rangle \psi)|^2 d^3 r, \tag{5-5}$$

where

$$\langle r \rangle = \int r |\psi|^2 d^3 r. \tag{5-6}$$

The calculated localization lengths for the electron (Δr_e) and hole (Δr_h) are presented in Figure 5-7(c). As expected, Δr_h is always smaller than Δr_e. Moreover, Δr_h is not sensitive to r_{ex}, whereas Δr_e tends to decrease as r_{ex} increases. It can be understood as follows: to pull carriers further away from the center, a stronger indium clustering effect is required, and it accompanies stronger localization of electron wavefunctions. The strong dependence of the radiative rate and the electron localization length is confirmed in Figure 5-7(d).

To further illustrate the strong bonding between electron and hole in an exciton and the localization effect, several examples of carrier probability density distribution, $|\langle \varphi_e | \varphi_h \rangle|^2$, are presented here. Figure 5-8 shows the probability density distribution of the 1st electron and hole state for a 30-nm InGaN QD with uniform indium distribution. The wavefunctions are concentrated at the center as expected. With random alloy effect, the wavefunctions are modified, as shown in Figure 5-9. The electron wavefunction is

significantly modified by the random alloy effect as shown by the distorted probability density distribution in Figure 5-9(a) and (b). Moreover, comparing the indium distribution at the upper InGaN/GaN interface (Figure 5-9(d)) and the probability density distribution (blue dash line in Figure 5-9(d)), we found that the electron wavefunction did not localize in a specific indium-rich region (red regions in Figure 5-9(d)). Instead, it is the collective effect of several indium-rich regions that determine the electron wavefunction. As for the hole wavefunction, it does not reside in any indium-rich region, and the distribution is less affected. It agrees with the previous conclusion that the hole wavefunction changes mainly because of Coulomb interaction.

The electron and hole wavefunction also allow us to study the fluctuation in radiative recombination rate. For most cases, the radiative recombination rate was shown to be enhanced by the random alloy effect, but two cases in Figure 5-8(b) actually exhibited slower recombination rates. The enhancement of radiative recombination can be explained by the localization effect. One example is shown in Figure 5-10, where the electron wavefunction is highly localized in a highly indium rich region that is 2~3 nm in size. Such localization results in large wavefunction overlap integral and fast radiative rate, which is 0.125 GHz while the average radiative rate is 0.096 GHz. On the contrary, if the electron wavefunction is more spread out, as in the case shown in Figure 5-11, the electron-hole wavefunction overlap decreases,

and the radiative rate reduces.

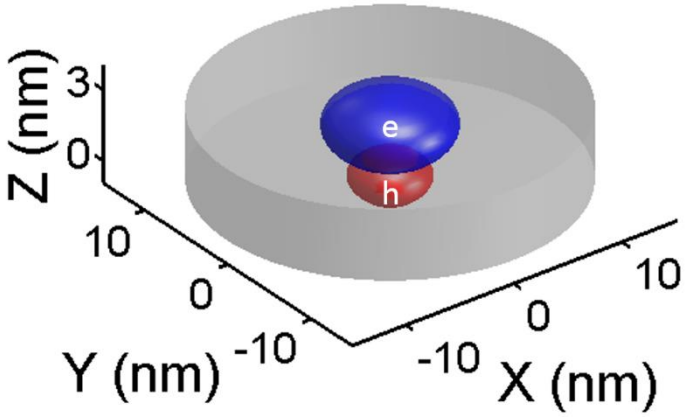

Figure 5-8. Isosurface of the probability density distribution (square of wavefunction) of the 1st electron and hole state for a 30-nm InGaN QD with uniform indium distribution in the x-y direction and Gaussian distribution in the z direction. The isosurface corresponds to one standard deviation.

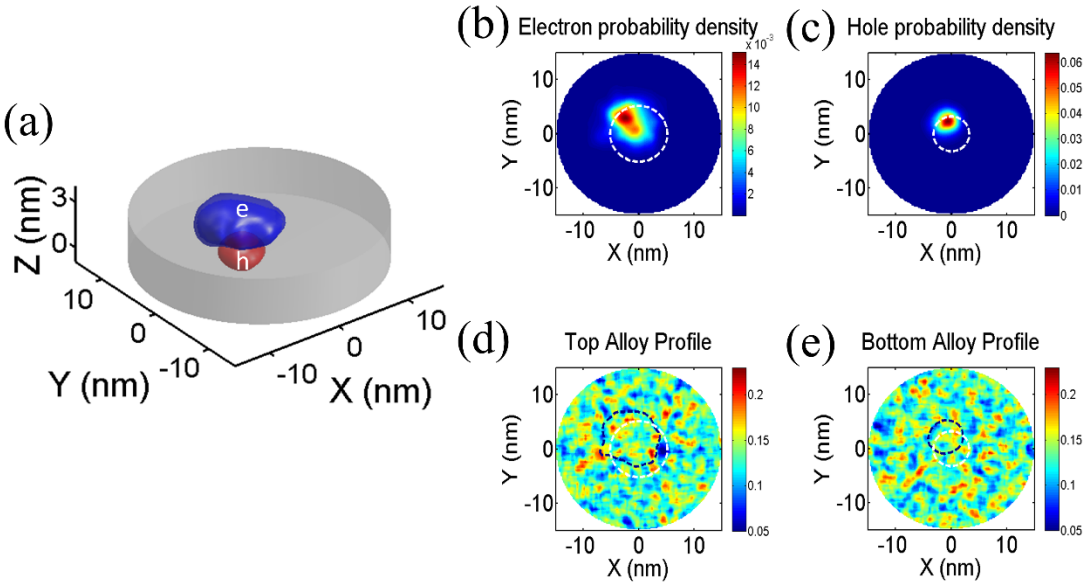

Figure 5-9. (a) One example (configuration #6) of the simulated probability density distribution with random alloy effect. (b) and (c) The contour plot showing the 1st state electron and hole probability density at a constant z slice where the wavefunctions peaked. (d) and (e) The contour plot of indium composition at the upper and lower InGaN/GaN interface. The blue dash line in (d) and (e) correspond to the contour line

of the electron and hole wavefunction at one standard deviation, respectively. The white dash line in (b), (c), (d), and (e) outlines the wavefunctions when the indium distribution is uniform.

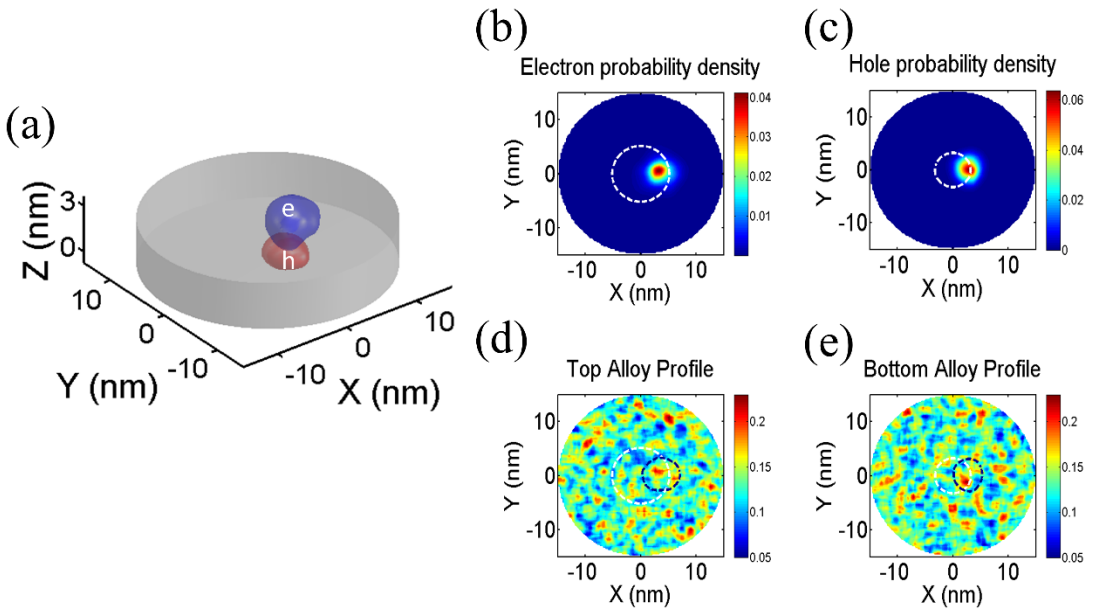

Figure 5-10. Simulated random alloy configuration #2 that showed strong localization effect and faster radiative decay rate. (a) isosurface of the electron and hole probability density distribution. (b) and (c) The contour plot showing the 1st state electron and hole probability density at a constant z slice where the wavefunctions peaked. (d) and (e) The contour plot of indium composition at the upper and lower InGaN/GaN interface. The blue dash line in (d) and (e) correspond to the contour line of the electron and hole wavefunction at one standard deviation, respectively. The white dash line in (b), (c), (d), and (e) outlines the wavefunctions when the indium distribution is uniform.

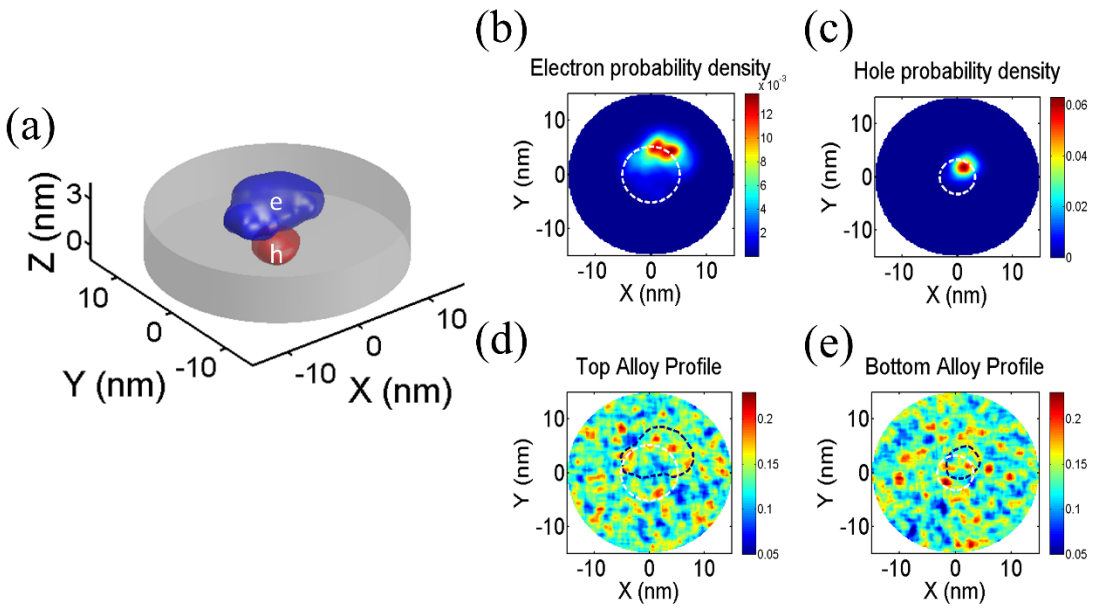

Figure 5-11. One example (configuration #5) of simulated random alloy configuration that showed more spread-out electron wavefunction and slower radiative decay rate. (a) isosurface of the electron and hole probability density distribution. (b) and (c) The contour plot showing the 1st state electron and hole probability density at a constant z slice where the wavefunctions peaked. (d) and (e) The contour plot of indium composition at the upper and lower InGaN/GaN interface. The blue dash line in (d) and (e) correspond to the contour line of the electron and hole wavefunction at one standard deviation, respectively. The white dash line in (b), (c), (d), and (e) outlines the wavefunctions when the indium distribution is uniform.

5.4.2 Inhomogeneity due to Well-Width Fluctuations

Simulations based on 30 different randomly generated well-width fluctuation configurations were performed as well. Figure 5-12(a) shows the histograms of calculated photon energy and also the experimental data acquired by single QD PL. The well-width fluctuation resulted in $\bar{E}_{WWF} = 2.8690$ eV and ΔE_{WWF}= 8.83 meV, based on the assumed 2-ML variation. $\bar{E}_{WWF}$ was almost identical to E_{ideal}, which was 2.8682 eV. ΔE_{WWF} was slightly smaller than ΔE_{RA} and much smaller than ΔE_{exp}

even if we intentionally increased the variation to 2 ML, instead of the experimentally observed 1 ML. As for the decay rate, $\bar{\gamma}_{WWF}$ was almost equal to γ_{ideal} and slower than $\bar{\gamma}_{RA}$. It indicated that the WWF-induced localization effect was not prominent.

In order to further understand the photon energy and recombination rate distribution, we analyzed the electron and hole position and the recombination rate for each simulated configurations in Figure 5-13. In Figure 5-13(a), the electron and hole clearly showed the strong tendency to stay at the center of QDs, thanks to the strain-relaxation induced potential. In other words, only the WWF around the center area matters. Since the probability of having thicker and thinner QW at the center was identical, the averaged photon energy was identical to the ideal case without WWF.

The expectation value of the electron and hole positions and the decay rate are summarized in Figure 5-13. In Figure 5-13(a) and (b), the electron and hole clearly show the strong tendency to stay at the center of QDs as the radial positions are always within 5-nm range around the center. Again, thanks to the good confinement, the radiative recombination rate is much larger than the nonradiative (tunneling) rate in Figure 5-13(c). Also, similar to photon energy, while the radiative rate fluctuated, the mean value is almost the same as $\gamma_{rad,ideal}$ (dash line in Figure 5-13(c)).

Furthermore, we observe a correlation between the radial positions of exciton, the photon energy, and the radiative rate (Figure 5-14(a) and (b)). The correlation can be

explained by the following. When the well-width is thicker at the center, carriers are trapped at the center because of the piezoelectric field. The QCSE red-shifts the photon energy, and the radiative rate is reduced. When the well-width is thinner at the center, the electron wavefunctions are pushed away from the center. As discussed in the previous section, as carriers move away from the center, the photon energy and the radiative rate increase because of the strain relaxation. We also observe that while the electron wavefunctions are pushed away from the center, they are also squeezed toward the hole wavefunctions in the z direction. Therefore, the photon energy and radiative rate increase faster than what is predicted solely by the strain relaxation effect (dash lines in Figure 5-14(a) and (b)). It was verified by calculating the mean QW-width in the regions enclosed by the electron wavefunctions and the strong correlation to the photon energy and the radiative decay rate in Figure 5-14(c) and (d). Figure 5-15 is one example of the simulation results, demonstrating that the electron wavefunction is off-centered because the central well width is thinner.

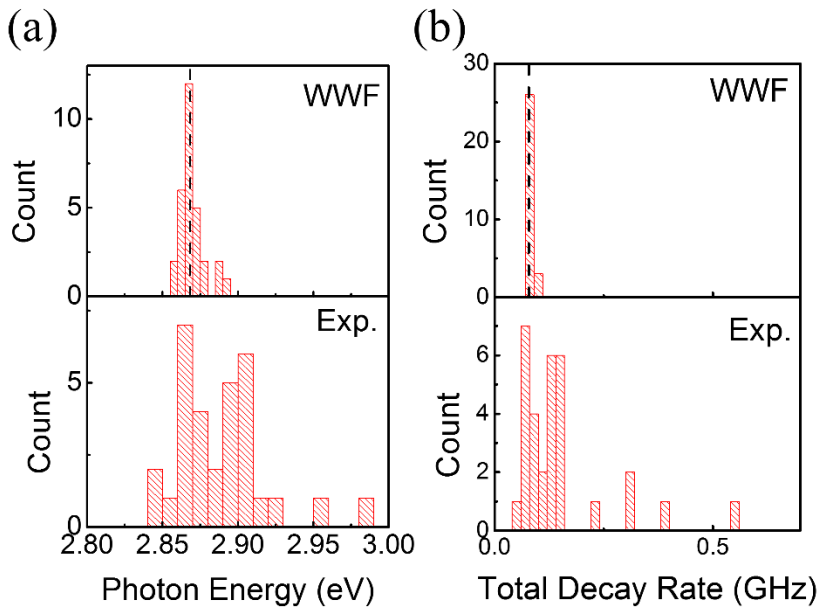

Figure 5-12. Histograms of (a) photon energy and (b) decay rate comparing the experimental data (lower) and the simulation results based on 30 randomly generated WWF configurations.

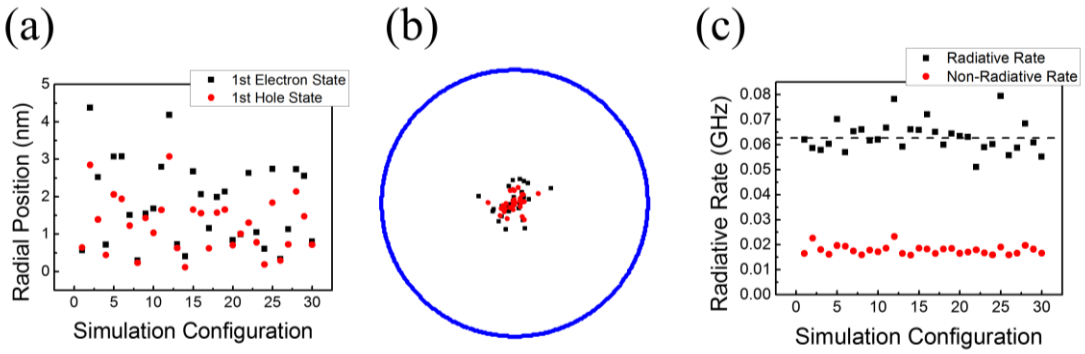

Figure 5-13. (a) Expectation values of the radial positions of 1st electron and hole state for the 30 randomly generated WWF configurations. (b) Visualization of (a) in a 30-nm QD (the blue circle). (c) Radiative and non-radiative recombination rate derived from wavefunction overlap integral and the tunneling model respectively.

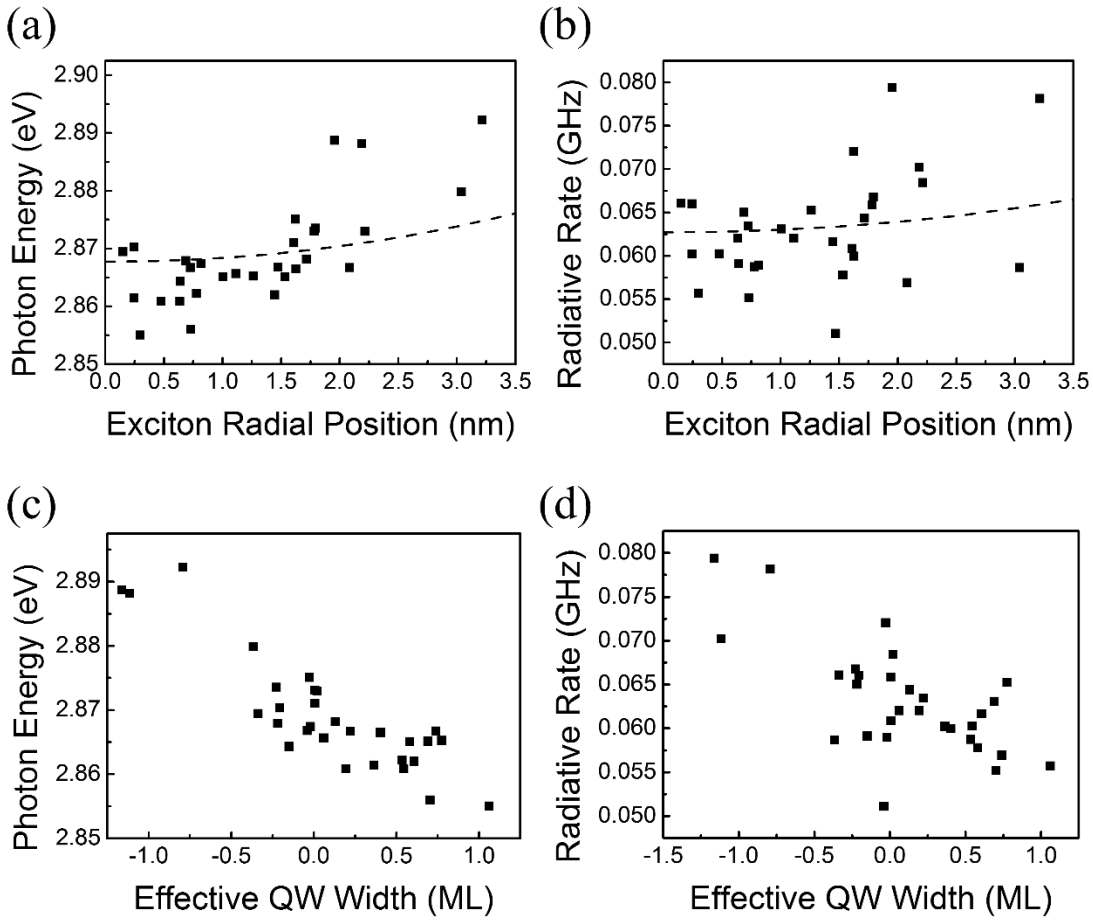

Figure 5-14. (a) Dependence of radiative rate on the exciton radial position. (b) Dependence of photon energy on the exciton radial position. The dash lines in (a) and (b) correspond to the photon energy and radiative rate solved based on the strain and potential at different radial positions. (c) The correlation between the photon energy and the effective QW width, which is the averaged QW width over an area enclosed by the isosurface of $|\psi_e|^2 = 0.1 \times \max(|\psi_e|^2)$. (d) The correlation between the radiative rate and the effective QW width.

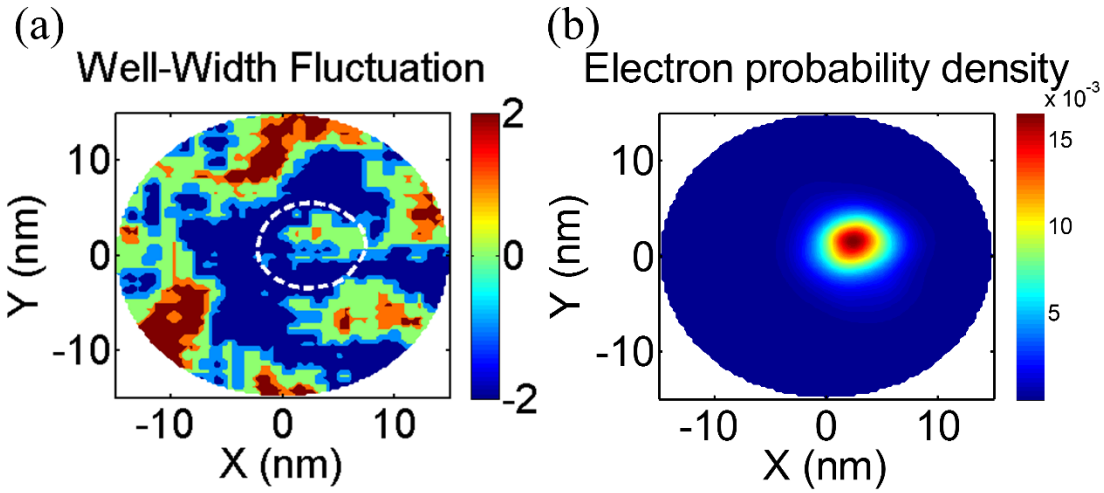

Figure 5-15. (a) Well-width fluctuation at the upper InGaN/GaN interface of simulated WWF configuration #25. The colors in the contour plot represent the variation in well-width in the unit of monolayer. The white dash line corresponds to one standard deviation of the electron probability density. (b) Probability density distribution of the 1st electron state based on the well-width fluctuation in (a).

5.4.3 Inhomogeneity due to Diameter Fluctuation

Diameter fluctuation caused by process errors can also occur among QDs. To study the effect of diameter fluctuation, we carried out simulations of 28-nm, 30-nm, and 32-nm QDs without either the random alloy effect nor the well-width fluctuation. The InGaN QW was assumed to be uniform in the x-y plane and Gaussian in the z direction for fair comparison. The results are shown in Figure 5-16. As expected, the photon energy and decay rate increase as the diameter is reduced. Based on SEM characterizations of 30-nm circular nanopillars, the standard deviation of the nanopillar diameter was found to be 1.7 nm in experiments. Assuming linear dependence of photon energy and decay rate on the diameter, a 1.7-nm diameter fluctuation leads to

ΔE_{DF} = 10.7 meV and $\Delta\gamma_{DF}$ = 0.0123 GHz. ΔE_{DF} was comparable to ΔE_{RA}, but $\Delta\gamma_{DF}$ was much smaller than $\Delta\gamma_{RA}$ as the random alloy effect strongly modifies the wavefunctions.

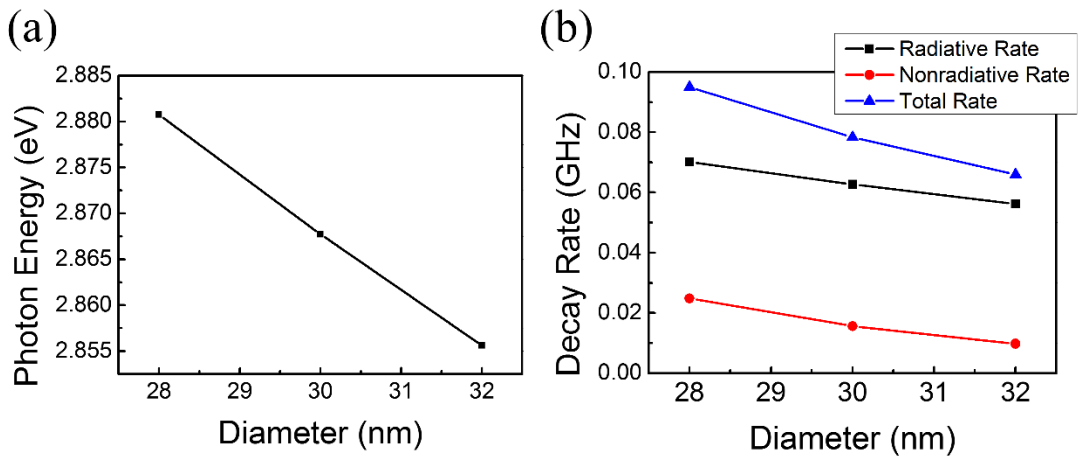

Figure 5-16. Diameter-dependence of (a) Photon energy and (b) decay rate.

5.4.4 Overall Inhomogeneity of Wurtzite InGaN QD

The experimental and theoretical results are summarized in Table 5-1. Considering all three effects (random alloy, well-width fluctuation, and diameter fluctuation), the total variation was calculated by $\Delta = \sqrt{\sigma_{RA}^2 + \sigma_{WWF}^2 + \sigma_{DA}^2}$. Experimentally, we observed much larger variation in photon energy and decay rate. It can be attributed to the global variations that were not taken into account and the nonradiative recombination that was not well-described by the tunneling model, such as defects inside QDs. In the parenthesis are the mean values and standard deviations when the

outliers (E > 2.95 eV and γ > 0.2 GHz) were excluded. The photon energy variation matched with simulations very well, whereas the decay rate variation was still much larger than the estimation by simulation. The discrepancy was ascribed to the lack of precise information on nonradiative recombination.

Table 5-1. Summary of photon energy and decay rate of wurtzite InGaN QDs acquired from PL measurements and simulations.

	E (eV)	ΔE (meV)	γ (GHz)	Δγ (GHz)
Experiment	2.8893	30.4	0.1462	0.1085
	(2.8834)	(20.8)	(0.1241)	(0.036)
Random Alloy	2.8542	10.8	0.1002	0.0162
Well-Width Fluctuation	2.8690	8.8	0.0810	0.0072
Diameter Fluctuation	2.8682	10.7	0.0627	0.0123
Total Variation		17.6		0.0216

5.5 Conclusion

In summary, we developed methodologies to model random alloy effect and well-width fluctuation in InGaN QDs and investigated the resulting inhomogeneity. In terms of photon energy, the random alloy effect, well-width fluctuation, and diameter

fluctuation showed similar contributions (~ 10 meV) to the total variation. As for the recombination rate, the random alloy effect was identified as the main factor for inhomogeneity. The simulation results were in good agreement with experimental data acquired from the PL and TRPL measurements of single QDs. Some outliers were observed from experiments and explained by the global variation of QW width and indium composition that were not considered in the simulation.

Chapter 6

Conclusions and Future Work

6.1 Conclusions

In this work we have demonstrated that InGaN/GaN nanopillar structures are very effective in strain relaxation, and the strain can be engineered by the nanopillar diameter and geometry. The strain engineering provided an additional design parameter and enabled novel functionalities of light emitting device.

First, we developed a top-down approach that combined e-beam lithography, ICP dry etching, and anisotropic KOH wet etching to fabricate vertical GaN nanopillars with embedded InGaN nanodisks. The top-down approach has several advantages over bottom-up or pick-and-place methods including but not limited to low cost, scalability,

optimal control of the positions, dimensions, and shape of the nanopillars. By tailoring the dimension and strain, we showed that top-down wurtzite InGaN/GaN nanopillars made from a planar QW wafer exhibited a wavelength tuning range from 473 nm to 654 nm, covering R-G-B three primary colors. The blue-shift of wavelength as the pillar diameter decreased was a result of strain relaxation and reduced piezoelectric field. To show the feasibility of nanopillar-based devices, we have also developed a planarization and metallization scheme. Despite the large contact resistance and turn-on voltage (6 V), multi-color electroluminescence was observed at room temperature under electrical injection. The electrical characteristics were well described by an equivalent circuit involving a Schottky diode, representing the Schottky contact at p-GaN/metal interface. Furthermore, we investigated the difference between EL properties, such as wavelength, FWHM, and intensity, between nanopillars and μm-pillars and found them in good agreement with the strain relaxation theory. Such multi-color LEDs can be very useful as compact multicolor light sources for applications including microdisplays, integrated light sources for biofluorescence arrays, and lab-on-chip devices.

Secondly, we demonstrated preprogrammed polarization of single photons via strain engineering. The small dimension of nanopillars and the strain-relaxation-induced nonuniform potential allowed strong exciton confinement and single photon emission. On top of that, we intentionally fabricated nanopillars with elliptical cross-

section and utilized the anisotropic strain to manipulate emission polarization. We successfully achieved single photon emission ($g^{(2)}(0) < 0.5$) with orthogonal polarization states from two QDs with orthogonal elliptical geometry. The degree of linear polarization was larger than 0.9. We also provided solid proof of the strong correlation between wurtzite InGaN QD geometry and emission polarization and showed DLP as a function of lateral aspect ratio. The results suggested wurtzite InGaN QD as a promising candidate for quantum light source emitting single photons with definitive polarization states for quantum information applications.

Thirdly, we theoretically studied the QD inhomogeneity. We considered random alloy effect, well-width fluctuation, and diameter fluctuation and found that random alloy effect and diameter fluctuation were the dominant factors of photon energy inhomogeneity. Both contributed ~ 11 meV to the photon energy inhomogeneity. As for inhomogeneity in radiative decay rate, we identified random alloy effect as the main cause because it strongly modified the electron wavefunctions. We also showed that the strain-relaxation-induced potential profile in the x-y directions provided strong confinement and kept carriers close to the center of QDs even when indium clustering and well-width fluctuation were present. This study shed light on the fundamental limit of InGaN QD inhomogeneity imposed by the random alloy effect and how close our QDs were to the fundamental limit given that the well-width and diameter were not

perfectly controlled. In addition, the results suggested that for applications that require an extremely fine control of QD properties, QDs made of single chemical elements or binary alloy materials would be better candidates, or the dynamic tuning of QD properties by mechanical, electrical, or magnetic means would be necessary to compensate the inhomogeneity.

6.2 Future Work

The first part of this thesis regarding multicolor nanopillar LEDs lays the foundation for device fabrication and design. The results enable better prediction and easier design for specific color or wavelength requirement once the original QW emission wavelength and the elastic property ($1/\kappa$) are known. The electrical operation at room temperature serves as a proof-of-concept for practical applications. To advance this technology, further optimization of fabrication processes is required in order to reduce the contact resistance and increase the brightness. Currently the contact resistance is high because the p-GaN was damaged during the etch-back. It makes the turn-on voltage high and limits the injection current. To tackle this issue, some post-etch treatments are needed to recover the p-GaN quality, or a different planarization/etch-back scheme has to be used to avoid the damage. Aside from optimizing the processes, taking the nanoLED technology to a system level is important

and can bring to interesting applications. One obvious future application is microdisplays. Demonstration of a multi-color microdisplay panel that is capable of showing simple images dynamically can greatly increase the application value. Hybrid integrations, such as nanoLEDs for biosensors or near-field imaging systems, are also fast-growing areas worth working on.

In terms of the QD single photon sources, we have showed the strength of the top-down approach for polarization control. But the experiment was done by PL, which limits practical applications. The obvious next step would be electrical operation by adopting the planarization and metallization scheme proposed in Chapter 3. In addition, the capability of generating single photons with predefined polarization states is helpful and valuable for on-chip integrations with polarization sensitive components, e.g. the coupling with polarization sensitive waveguides or cavities [146,147]. Such coupling has been discussed theoretically but hard to achieve in experiments due to the lack of proper quantum light sources or the difficulties in integration. Our QDs can help overcome the obstacles because they provide solutions to on-chip polarized single photon sources that can be easily integrated with cavities or waveguides by top-down approaches.

Finally, the theoretical analysis regarding random alloy and other non-ideal effects suggests that, in order to eliminate the inhomogeneity among QDs , either binary alloys

or the capability of dynamic tuning are required. Possible binary alloys include GaN, InN, and other II-VI QDs. Among these, GaN and ZnO are the most promising for high temperature single photon sources due to their large exciton binding energy [148]. However, from the perspective of electrical operation, GaN has a huge advantage because reliable p-type doping in ZnO has not been found yet [149]. Therefore, top-down GaN/AlN can be worth studying. In terms of dynamically tuning the properties of individual QDs, one easy scheme is to fabricate metal electrodes around single QDs and utilize the Stark effect to manipulate photon energy dynamically [150].

Bibliography

1 Nakamura, Shuji, Takashi Mukai, and Masayuki Senoh. "Candela-class high-brightness InGaN/AlGaN double-heterostructure blue-light-emitting diodes."*Applied Physics Letters* 64, no. 13 (1994): 1687-1689.

2 Nakamura, Shigenari, and Michael R. Krames. "History of gallium–nitride-based light-emitting diodes for illumination." Proceedings of the IEEE 101, no. 10 (2013): 2211-2220.

3 Nakamura, Shuji, Stephen Pearton, and Gerhard Fasol. The blue laser diode: the complete story. Springer Science & Business Media, 2013.

4 Schulz, Heinz, and K. H. Thiemann. "Crystal structure refinement of AlN and GaN." Solid State Communications 23, no. 11 (1977): 815-819.

5 Osamura, Kozo, Shigehisa Naka, and Yotaro Murakami. "Preparation and optical properties of $Ga_{1-x}In_xN$ thin films." Journal of Applied Physics 46, no. 8 (1975): 3432-3437.

6 Monemar, B. "III-V nitrides—important future electronic materials." Journal of Materials Science: Materials in Electronics 10, no. 4 (1999): 227-254.

7 Perry, P. B., and R. F. Rutz. "The optical absorption edge of single-crystal AlN prepared by a close-spaced vapor process." Applied Physics Letters 33, no. 4 (1978): 319-321.

8 Davydov, V. Yu, A. A. Klochikhin, Vadim V. Emtsev, A. V. Sakharov, S. V. Ivanov, V. A. Vekshin, Friedhelm Bechstedt et al. "Bandgap of hexagonal InN and InGaN alloys." In 10th International Symposium on Nanostructures: Physics and Technology, pp. 68-71. International Society for Optics and Photonics, 2002.

9 Wong, W. S., T. Sands, N. W. Cheung, M. Kneissl, D. P. Bour, P. Mei, L. T. Romano, and N. M. Johnson. "Fabrication of thin-film InGaN light-emitting diode membranes by laser lift-off." *Applied physics letters* 75, no. 10 (1999): 1360-1362.

10 Fujii, T., Y. Gao, R. Sharma, E. L. Hu, S. P. DenBaars, and S. Nakamura. "Increase in the extraction efficiency of GaN-based light-emitting diodes via surface roughening." *Applied physics letters* 84, no. 6 (2004): 855-857.

11 Cho, Hyun Kyong, Junho Jang, Jeong-Hyeon Choi, Jaewan Choi, Jongwook Kim, Jeong Soo Lee, Beomseok Lee et al. "Light extraction enhancement from nano-imprinted photonic crystal GaN-based blue light-emitting diodes." *Optics Express*14,

no. 19 (2006): 8654-8660.

12 Wierer, Jonathan J., Aurelien David, and Mischa M. Megens. "III-nitride photonic-crystal light-emitting diodes with high extraction efficiency." *Nature Photonics* 3, no. 3 (2009): 163-169.

13 Zhang, Yun Yan, and Yi An Yin. "Performance enhancement of blue light-emitting diodes with a special designed AlGaN/GaN superlattice electron-blocking layer." *Applied physics letters* 99, no. 22 (2011): 221103.

14 Masui, Hisashi, Shuji Nakamura, Steven P. DenBaars, and Umesh K. Mishra. "Nonpolar and semipolar III-nitride light-emitting diodes: achievements and challenges." *Electron Devices, IEEE Transactions on* 57, no. 1 (2010): 88-100.

15 Jang, Jongjin, Seohwi Woo, Daehong Min, and Okhyun Nam. "Recent Advances in Nonpolar and Semipolar InGaN Light-Emitting Diodes (LEDs)." Journal of Nanoscience and Nanotechnology 15, no. 3 (2015): 1895-1906.

16 El-Ghoroury, Hussein S., and Zahir Y. Alpaslan. "Quantum Photonic Imager (QPI): A New Display Technology and Its Applications." In Invited) Proceedings of The International Display Workshops, vol. 21. 2014.

17 Hwang, Jong-Il, Rei Hashimoto, Shinji Saito, and Shinya Nunoue. "Development of InGaN-based red LED grown on (0001) polar surface." Applied Physics Express 7, no. 7 (2014): 071003.

18 Sekiguchi, Hiroto, Katsumi Kishino, and Akihiko Kikuchi. "Emission color control from blue to red with nanocolumn diameter of InGaN/GaN nanocolumn arrays grown on same substrate." Applied physics letters 96, no. 23 (2010): 231104.

19 Jahangir, S., M. Mandl, M. Strassburg, and P. Bhattacharya. "Molecular beam epitaxial growth and optical properties of red-emitting (λ= 650 nm) InGaN/GaN disks-in-nanowires on silicon." Applied Physics Letters 102, no. 7 (2013): 071101.

20 Albert, S., A. Bengoechea-Encabo, X. Kong, M. A. Sanchez-Garcia, E. Calleja, and A. Trampert. "Monolithic integration of InGaN segments emitting in the blue, green, and red spectral range in single ordered nanocolumns." Applied Physics Letters 102, no. 18 (2013): 181103.

21 Bennett Ch, H., and G. Brassard. "Quantum cryptography: public key distribution and coin tossing Int." In Conf. on Computers, Systems and Signal Processing (Bangalore, India, Dec. 1984), pp. 175-9. 1984.

22 Pooley, M. A., D. J. P. Ellis, R. B. Patel, A. J. Bennett, K. H. A. Chan, I. Farrer, D. A. Ritchie, and A. J. Shields. "Controlled-NOT gate operating with single photons." Applied Physics Letters 100, no. 21 (2012): 211103.

23 Xiao, Min, Ling-An Wu, and H. Jeffrey Kimble. "Precision measurement beyond the shot-noise limit." Physical review letters 59, no. 3 (1987): 278.

24 Rarity, J. G., P. C. M. Owens, and P. R. Tapster. "Quantum random-number generation and key sharing." Journal of Modern Optics 41, no. 12 (1994): 2435-2444.

25 Darquié, Benoit, Matthew PA Jones, Jos Dingjan, Jerome Beugnon, Silvia Bergamini, Yvan Sortais, Gaetan Messin, Antoine Browaeys, and Philippe Grangier. "Controlled single-photon emission from a single trapped two-level atom." Science 309, no. 5733 (2005): 454-456.

26 Lounis, Brahim, and W. E. Moerner. "Single photons on demand from a single molecule at room temperature." Nature 407, no. 6803 (2000): 491-493.

27 Kurtsiefer, Christian, Sonja Mayer, Patrick Zarda, and Harald Weinfurter. "Stable solid-state source of single photons." Physical Review Letters 85, no. 2 (2000): 290.

28 Morfa, Anthony J., Brant C. Gibson, Matthias Karg, Timothy J. Karle, Andrew D. Greentree, Paul Mulvaney, and Snjezana Tomljenovic-Hanic. "Single-photon emission and quantum characterization of zinc oxide defects." Nano letters 12, no. 2 (2012): 949-954.

29 Michler, P., A. Imamoğlu, M. D. Mason, P. J. Carson, G. F. Strouse, and S. K. Buratto. "Quantum correlation among photons from a single quantum dot at room temperature." Nature 406, no. 6799 (2000): 968-970.

30 Shields, Andrew J. "Semiconductor quantum light sources." Nature photonics 1, no. 4 (2007): 215-223.

31 Yuan, Zhiliang, Beata E. Kardynal, R. Mark Stevenson, Andrew J. Shields, Charlene J. Lobo, Ken Cooper, Neil S. Beattie, David A. Ritchie, and Michael Pepper. "Electrically driven single-photon source." Science 295, no. 5552 (2002): 102-105.

32 Yoshie, Tomoyuki, Axel Scherer, J. Hendrickson, G. Khitrova, H. M. Gibbs, G. Rupper, C. Ell, O. B. Shchekin, and D. G. Deppe. "Vacuum Rabi splitting with a single quantum dot in a photonic crystal nanocavity." Nature 432, no. 7014 (2004): 200-203.

33 Hennessy, Kevin, Antonio Badolato, M. Winger, D. Gerace, Mete Atatüre, S. Gulde, S. Fält, Evelyn L. Hu, and A. Imamoğlu. "Quantum nature of a strongly coupled single quantum dot–cavity system." Nature 445, no. 7130 (2007): 896-899.

34 Claudon, Julien, Joël Bleuse, Nitin Singh Malik, Maela Bazin, Périne Jaffrennou, Niels Gregersen, Christophe Sauvan, Philippe Lalanne, and Jean-Michel Gérard. "A highly efficient single-photon source based on a quantum dot in a photonic nanowire." Nature Photonics 4, no. 3 (2010): 174-177.

35 Englund, Dirk, Andrei Faraon, Bingyang Zhang, Yoshihisa Yamamoto, and Jelena Vučković. "Generation and transfer of single photons on a photonic crystal chip." Optics Express 15, no. 9 (2007): 5550-5558.

36 Laucht, A., S. Pütz, T. Günthner, N. Hauke, R. Saive, S. Frédérick, M. Bichler et al. "A waveguide-coupled on-chip single-photon source." Physical Review X 2, no. 1 (2012): 011014.

37 Michler, P., A. Kiraz, C. Becher, W. V. Schoenfeld, P. M. Petroff, Lidong Zhang, E. Hu, and A. Imamoglu. "A quantum dot single-photon turnstile device." Science290, no. 5500 (2000): 2282-2285.

38 Stevenson, R. Mark, Robert J. Young, Paola Atkinson, Ken Cooper, David A. Ritchie, and Andrew J. Shields. "A semiconductor source of triggered entangled photon pairs." Nature 439, no. 7073 (2006): 179-182.

39 Bonadeo, Nicolas H., John Erland, D. Gammon, D. Park, D. S. Katzer, and D. G. Steel. "Coherent optical control of the quantum state of a single quantum dot."Science 282, no. 5393 (1998): 1473-1476.

40 Kako, Satoshi, Charles Santori, Katsuyuki Hoshino, Stephan Götzinger, Yoshihisa Yamamoto, and Yasuhiko Arakawa. "A gallium nitride single-photon source operating at 200 K." Nature materials 5, no. 11 (2006): 887-892.

41 Deshpande, Saniya, and Pallab Bhattacharya. "An electrically driven quantum dot-in-nanowire visible single photon source operating up to 150 K." Applied Physics Letters 103, no. 24 (2013): 241117.

42 Holmes, Mark J., Kihyun Choi, Satoshi Kako, Munetaka Arita, and Yasuhiko Arakawa. "Room-temperature triggered single photon emission from a III-nitride site-controlled nanowire quantum dot." Nano letters 14, no. 2 (2014): 982-986.

43 Takeuchi, Tetsuya, Shigetoshi Sota, Maki Katsuragawa, Miho Komori, Hideo Takeuchi, Hiroshi Amano, and Isamu Akasaki. "Quantum-confined Stark effect due to piezoelectric fields in GaInN strained quantum wells." *Japanese Journal of Applied Physics* 36, no. 4A (1997): L382.

44 Kim, Min-Ho, Martin F. Schubert, Qi Dai, Jong Kyu Kim, E. Fred Schubert, Joachim Piprek, and Yongjo Park. "Origin of efficiency droop in GaN-based light-emitting diodes." *Applied Physics Letters* 91, no. 18 (2007): 183507.

45 Zhang, Zi-Hui, Wei Liu, Zhengang Ju, Swee Tiam Tan, Yun Ji, Zabu Kyaw, Xueliang Zhang, Liancheng Wang, Xiao Wei Sun, and Hilmi Volkan Demir. "InGaN/GaN multiple-quantum-well light-emitting diodes with a grading InN composition suppressing the Auger recombination." *Applied Physics Letters* 105, no. 3 (2014): 033506.

46 Singh, Jasprit. Electronic and optoelectronic properties of semiconductor structures. Cambridge University Press, 2003.

47 Hoshi, T., K. Hazu, K. Ohshita, M. Kagaya, T. Onuma, S. F. Chichibu, K. Fujito, and H. Namita. "Impacts of anisotropic lattice relaxation on crystal mosaicity and luminescence spectra of m-plane $Al_xGa_{1-x}N$ films grown on m-plane freestanding GaN substrates by NH_3 source molecular beam epitaxy." *Applied Physics Letters* 94, no. 7 (2009).

48 Trotta, R., E. Zallo, C. Ortix, P. Atkinson, J. D. Plumhof, J. Van den Brink, A. Rastelli, and O. G. Schmidt. "Universal recovery of the energy-level degeneracy of bright excitons in InGaAs quantum dots without a structure symmetry."*Physical review* letters 109, no. 14 (2012): 147401.

49 Ryu, Bengso, Wael Z. Tawfik, Seo-Jung Bae, Jun Seok Ha, Sang-Wan Ryu, Hee Seok Choi, and June Key Lee. "Uni-axial external stress effect on green InGaN/GaN multi-quantum-well light-emitting diodes." Journal of Physics D: Applied Physics 46, no. 43 (2013): 435103.

50 Böcklin, Christoph, Ratko G. Veprek, Sebastian Steiger, and Bernd Witzigmann. "Computational study of an InGaN/GaN nanocolumn light-emitting diode." Physical Review B 81, no. 15 (2010): 155306.

51 Sacconi, Fabio, Der Maur, Matthias Auf, and Aldo Di Carlo. "Optoelectronic Properties of Nanocolumn InGaN/GaN LEDs." Electron Devices, IEEE Transactions on 59, no. 11 (2012): 2979-2987.

52 Nguyen, Hieu Pham Trung, Shaofei Zhang, Kai Cui, Andreas Korinek, Gianluigi Botton, and Zetian Mi. "High-efficiency InGaN/GaN dot-in-a-wire red light-emitting diodes." Photonics Technology Letters, IEEE 24, no. 4 (2012): 321-323.

53 Jahangir, Shafat, Tilman Schimpke, Martin Strassburg, Kevin Grossklaus, Joanna M. Millunchick, and Pallab Bhattacharya. "Red-Emitting (nm) In 0.51 Ga 0.49 N/GaN Disk-in-Nanowire Light Emitting Diodes on Silicon." Quantum Electronics, IEEE Journal of 50, no. 7 (2014): 530-537.

54 Jiang, H. X., S. X. Jin, J. Li, J. Shakya, and J. Y. Lin. "III-nitride blue microdisplays." Applied Physics Letters 78, no. 9 (2001): 1303-1305.

55 McKendry, Jonathan JD, Bruce R. Rae, Zheng Gong, Keith R. Muir, Benoit Guilhabert, David Massoubre, Erdan Gu, David Renshaw, Martin D. Dawson, and Robert K. Henderson. "Individually addressable AlInGaN micro-LED arrays with CMOS control and subnanosecond output pulses." Photonics Technology Letters, IEEE 21, no. 12 (2009): 811-813.

56 Day, Jacob, J. Li, D. Y. C. Lie, Charles Bradford, J. Y. Lin, and H. X. Jiang. "III-Nitride full-scale high-resolution microdisplays." Applied Physics Letters 99, no. 3

(2011): 031116.

57 Heliotis, G., E. Gu, C. Griffin, C. W. Jeon, P. N. Stavrinou, M. D. Dawson, and D. D. C. Bradley. "Wavelength-tunable and white-light emission from polymer-converted micropixellated InGaN ultraviolet light-emitting diodes." Journal of Optics A: Pure and Applied Optics 8, no. 7 (2006): S445.

58 Goßler, Christian, Colin Bierbrauer, Rüdiger Moser, Michael Kunzer, Katarzyna Holc, Wilfried Pletschen, Klaus Köhler et al. "GaN-based micro-LED arrays on flexible substrates for optical cochlear implants." Journal of Physics D: Applied Physics 47, no. 20 (2014): 205401.

59 Xu, H., J. Zhang, K. M. Davitt, Y. K. Song, and A. V. Nurmikko. "Application of blue–green and ultraviolet micro-LEDs to biological imaging and detection." Journal of Physics D: Applied Physics 41, no. 9 (2008): 094013.

60 Kim, Tae-Ho, Kyung-Sang Cho, Eun Kyung Lee, Sang Jin Lee, Jungseok Chae, Jung Woo Kim, Do Hwan Kim et al. "Full-colour quantum dot displays fabricated by transfer printing." Nature Photonics 5, no. 3 (2011): 176-182.

61 Cich, Michael J., Rafael I. Aldaz, Arpan Chakraborty, Aurelien David, Michael J. Grundmann, Anurag Tyagi, Meng Zhang, Frank M. Steranka, and Michael R. Krames. "Bulk GaN based violet light-emitting diodes with high efficiency at very high current density." *Applied Physics Letters* 101, no. 22 (2012): 223509.

62 Chang, Moon-Hwan, Diganta Das, P. V. Varde, and Michael Pecht. "Light emitting diodes reliability review." *Microelectronics Reliability* 52, no. 5 (2012): 762-782.

63 Kishino, Katsumi, Kazuya Nagashima, and Kouji Yamano. "Monolithic integration of InGaN-based nanocolumn light-emitting diodes with different emission colors." Applied Physics Express 6, no. 1 (2013): 012101.

64 Wang, Renjie, Hieu Nguyen, Ashfiqua T. Connie, J. Lee, Ishiang Shih, and Zetian Mi. "Color-tunable, phosphor-free InGaN nanowire light-emitting diode arrays monolithically integrated on silicon." Optics express 22, no. 107 (2014): A1768-A1775.

65 Ramesh, V., Akihiko Kikuchi, Katsumi Kishino, Mitsuru Funato, and Yoichi Kawakami. "Strain relaxation effect by nanotexturing InGaN/GaN multiple quantum well." Journal of Applied Physics 107, no. 11 (2010): 114303.

66 Kawakami, Y., A. Kaneta, L. Su, Y. Zhu, K. Okamoto, M. Funato, A. Kikuchi, and K. Kishino. "Optical properties of InGaN/GaN nanopillars fabricated by postgrowth chemically assisted ion beam etching." Journal of Applied Physics 107, no. 2 (2010): 023522.

67 Wu, Yuh-Renn, Chinghua Chiu, Cheng-Yu Chang, Peichen Yu, and Hao-Chung Kuo. "Size-dependent strain relaxation and optical characteristics of InGaN/GaN nanorod

LEDs." Selected Topics in Quantum Electronics, IEEE Journal of 15, no. 4 (2009): 1226-1233.

68 Zhang, Lei, Leung-Kway Lee, Chu-Hsiang Teng, Tyler A. Hill, Pei-Cheng Ku, and Hui Deng. "How much better are InGaN/GaN nanodisks than quantum wells—Oscillator strength enhancement and changes in optical properties." Applied Physics Letters 104, no. 5 (2014): 051116.

69 Romanov, A. E., T. J. Baker, S. Nakamura, and J. S. Speck. "Strain-induced polarization in wurtzite III-nitride semipolar layers." Journal of Applied Physics 100, no. 2 (2006).

70 Stocker, D. A., E. F. Schubert, and J. M. Redwing. "Crystallographic wet chemical etching of GaN." Applied Physics Letters 73, no. 18 (1998): 2654-2656.

71 Yu, Peichen, C. H. Chiu, Yuh-Renn Wu, H. H. Yen, J. R. Chen, C. C. Kao, Han-Wei Yang et al. "Strain relaxation induced microphotoluminescence characteristics of a single InGaN-based nanopillar fabricated by focused ion beam milling." Applied Physics Letters 93, no. 8 (2008).

72 Song, June O., Jun-Seok Ha, and Tae-Yeon Seong. "Ohmic-contact technology for GaN-based light-emitting diodes: role of P-type contact." Electron Devices, IEEE Transactions on 57, no. 1 (2010): 42-59.

73 Sheu, J. K., Yan-Kuin Su, Gou-Chung Chi, P. L. Koh, M. J. Jou, C. M. Chang, C. C. Liu, and W. C. Hung. "High-transparency Ni/Au ohmic contact to p-type GaN." Applied physics letters 74, no. 16 (1999): 2340-2342.

74 Miller, D. A. B., D. S. Chemla, T. C. Damen, A. C. Gossard, W. Wiegmann, T. H. Wood, and C. A. Burrus. "Electric field dependence of optical absorption near the band gap of quantum-well structures." Physical Review B 32, no. 2 (1985): 1043.

75 Chen, Jeng-Hung, Zhe-Chuan Feng, Hung-Ling Tsai, Jer-Ren Yang, P. Li, C. Wetzel, T. Detchprohm, and J. Nelson. "Optical and structural properties of InGaN/GaN multiple quantum well structure grown by metalorganic chemical vapor deposition." Thin Solid Films 498, no. 1 (2006): 123-127.

76 Xu, Jiuru, Martin F. Schubert, Ahmed N. Noemaun, Di Zhu, Jong Kyu Kim, E. Fred Schubert, Min Ho Kim et al. "Reduction in efficiency droop, forward voltage, ideality factor, and wavelength shift in polarization-matched GaInN/GaInN multi-quantum-well light-emitting diodes." Applied Physics Letters 94, no. 1 (2009): 011113.

77 Guo, Wei, Meng Zhang, Animesh Banerjee, and Pallab Bhattacharya. "Catalyst-free InGaN/GaN nanowire light emitting diodes grown on (001) silicon by molecular beam epitaxy." Nano letters 10, no. 9 (2010): 3355-3359.

78 Lin, Hon-Way, Yu-Jung Lu, Hung-Ying Chen, Hong-Mao Lee, and Shangjr Gwo.

"InGaN/GaN nanorod array white light-emitting diode." Applied Physics Letters 97, no. 7 (2010): 073101.

79 Zhang, Lei, Tyler A. Hill, Chu-Hsiang Teng, Brandon Demory, Pei-Cheng Ku, and Hui Deng. "Carrier dynamics in site-and structure-controlled InGaN/GaN quantum dots." Physical Review B 90, no. 24 (2014): 245311.

80 Nakamura, Shuji. "The roles of structural imperfections in InGaN-based blue light-emitting diodes and laser diodes." Science 281, no. 5379 (1998): 956-961.

81 Dumin, D. J., and G. L. Pearson. "Properties of gallium arsenide diodes between 4.2 and 300 K." Journal of Applied Physics 36, no. 11 (1965): 3418-3426.

82 Eliseev, Petr G., Piotr Perlin, Julien Furioli, Philippe Sartori, Jian Mu, and Marek Osiński. "Tunneling current and electroluminescence in InGaN: Zn, Si/AlGaN/GaN blue light emitting diodes." Journal of electronic materials 26, no. 3 (1997): 311-319.

83 Fedison, J. B., T. P. Chow, H. Lu, and I. B. Bhat. "Electrical characteristics of magnesium-doped gallium nitride junction diodes." Applied physics letters 72, no. 22 (1998): 2841-2843.

84 Meneghini, M., N. Trivellin, M. Pavesi, M. Manfredi, U. Zehnder, B. Hahn, G. Meneghesso, and E. Zanoni. "Leakage current and reverse-bias luminescence in InGaN-based light-emitting diodes." Applied Physics Letters 95, no. 17 (2009): 173507.

85 Padovani, F. A., and R. Stratton. "Field and thermionic-field emission in Schottky barriers." Solid-State Electronics 9, no. 7 (1966): 695-707.

86 Lee, L. K., Lei Zhang, Hui Deng, and P-C. Ku. "Room-temperature quantum-dot-like luminescence from site-controlled InGaN quantum disks." Applied Physics Letters 99, no. 26 (2011): 263105.

87 Zhang, Lei, Chu-Hsiang Teng, Tyler A. Hill, Leung-Kway Lee, Pei-Cheng Ku, and Hui Deng. "Single photon emission from site-controlled InGaN/GaN quantum dots." Applied Physics Letters 103, no. 19 (2013): 192114.

88 Robinett, R. W. "Visualizing the solutions for the circular infinite well in quantum and classical mechanics." American Journal of Physics 64, no. 4 (1996): 440-445.

89 Amloy, Supaluck, K. H. Yu, K. F. Karlsson, Rashid Farivar, T. G. Andersson, and Per-Olof Holtz. "Size dependent biexciton binding energies in GaN quantum dots." Applied Physics Letters 99, no. 25 (2011): 251903.

90 Zhang, Lei, Tyler A. Hill, Chu-Hsiang Teng, Brandon Demory, Pei-Cheng Ku, and Hui Deng. "Carrier dynamics in site-and structure-controlled InGaN/GaN quantum dots." Physical Review B 90, no. 24 (2014): 245311.

91 Santori, Charles, David Fattal, and Yoshihisa Yamamoto. Single-photon devices and applications. John Wiley & Sons, 2010.

92 Deshpande, Saniya, Thomas Frost, Arnab Hazari, and Pallab Bhattacharya. "Electrically pumped single-photon emission at room temperature from a single InGaN/GaN quantum dot." Applied Physics Letters 105, no. 14 (2014): 141109.

93 Brouri, Rosa, Alexios Beveratos, Jean-Philippe Poizat, and Philippe Grangier. "Photon antibunching in the fluorescence of individual color centers in diamond." Optics letters 25, no. 17 (2000): 1294-1296.

94 Lochmann, A., E. Stock, J. A. Töfflinger, W. Unrau, A. Toropov, A. Bakarov, V. Haisler, and D. Bimberg. "Electrically pumped, micro-cavity based single photon source driven at 1 GHz." Electronics Letters 45, no. 11 (2009): 566-567.

95 Bounouar, Samir, Miryam Elouneg-Jamroz, M. den Hertog, C. Morchutt, E. Bellet-Amalric, Régis André, Catherine Bougerol et al. "Ultrafast room temperature single-photon source from nanowire-quantum Dots." Nano letters 12, no. 6 (2012): 2977-2981.

96 Hargart, F., C. A. Kessler, T. Schwarzbäck, E. Koroknay, S. Weidenfeld, M. Jetter, and P. Michler. "Electrically driven quantum dot single-photon source at 2 GHz excitation repetition rate with ultra-low emission time jitter." Applied Physics Letters 102, no. 1 (2013): 011126.

97 Ates, S., S. M. Ulrich, S. Reitzenstein, A. Löffler, A. Forchel, and P. Michler. "Post-selected indistinguishable photons from the resonance fluorescence of a single quantum dot in a microcavity." Physical Review Letters 103, no. 16 (2009): 167402.

98 Mizuochi, N., T. Makino, H. Kato, D. Takeuchi, M. Ogura, H. Okushi, M. Nothaft et al. "Electrically driven single-photon source at room temperature in diamond." Nature photonics 6, no. 5 (2012): 299-303.

99 Strauf, Stefan, Nick G. Stoltz, Matthew T. Rakher, Larry A. Coldren, Pierre M. Petroff, and Dirk Bouwmeester. "High-frequency single-photon source with polarization control." Nature photonics 1, no. 12 (2007): 704-708.

100 Muller, Antoine, J. Breguet, and N. Gisin. "Experimental demonstration of quantum cryptography using polarized photons in optical fibre over more than 1 km." EPL (Europhysics Letters) 23, no. 6 (1993): 383.

101 Unitt, D. C., A. J. Bennett, P. Atkinson, D. A. Ritchie, and A. J. Shields. "Polarization control of quantum dot single-photon sources via a dipole-dependent Purcell effect." Physical Review B 72, no. 3 (2005): 033318.

102 Whittaker, D. M., P. S. S. Guimaraes, D. Sanvitto, H. Vinck, S. Lam, A. Daraei, J.

A. Timpson et al. "High Q modes in elliptical microcavity pillars." Applied physics letters 90, no. 16 (2007): 1105.

103 Oulton, R., B. D. Jones, S. Lam, A. R. A. Chalcraft, D. Szymanski, D. O'Brien, T. F. Krauss et al. "Polarized quantum dot emission from photonic crystal nanocavities studied under moderesonant enhanced excitation." Optics express 15, no. 25 (2007): 17221-17230.

104 Chen, Wei, Guang-Yin Chen, and Yueh-Nan Chen. "Coherent transport of nanowire surface plasmons coupled to quantum dots." Optics express 18, no. 10 (2010): 10360-10368.

105 Gonzalez-Tudela, A., Diego Martin-Cano, Esteban Moreno, Luis Martin-Moreno, C. Tejedor, and Francisco J. Garcia-Vidal. "Entanglement of two qubits mediated by one-dimensional plasmonic waveguides." arXiv preprint arXiv:1010.5048 (2010).

106 Chuang, Shun Lien. Physics of photonic devices. Vol. 80. John Wiley & Sons, 2012.

107 Gammon, D., E. S. Snow, B. V. Shanabrook, D. S. Katzer, and D. Park. "Fine structure splitting in the optical spectra of single GaAs quantum dots." Physical review letters 76, no. 16 (1996): 3005.

108 Sugisaki, Mitsuru, Hong-Wen Ren, Selvakumar V. Nair, Kenichi Nishi, Shigeo Sugou, Tsuyoshi Okuno, and Yasuaki Masumoto. "Optical anisotropy in self-assembled InP quantum dots." Physical review B 59, no. 8 (1999): R5300.

109 Poem, E., J. Shemesh, I. Marderfeld, D. Galushko, N. Akopian, D. Gershoni, B. D. Gerardot, A. Badolato, and P. M. Petroff. "Polarization sensitive spectroscopy of charged quantum dots." arXiv preprint arXiv:0706.1288 (2007).

110 Kahl, Matthias, Tim Thomay, Verena Kohnle, Katja Beha, Jörg Merlein, Matthias Hagner, Andreas Halm et al. "Colloidal quantum dots in all-dielectric high-Q pillar microcavities." Nano letters 7, no. 9 (2007): 2897-2900.

111 Rakher, M. T., N. G. Stoltz, L. A. Coldren, P. M. Petroff, and D. Bouwmeester. "Polarization-switchable single photon source using the Stark effect." Applied Physics Letters 93, no. 9 (2008): 091118.

112 Lundskog, Anders, Chih-Wei Hsu, K. Fredrik Karlsson, Supaluck Amloy, Daniel Nilsson, Urban Forsberg, Per Olof Holtz, and Erik Janzén. "Direct generation of linearly polarized photon emission with designated orientations from site-controlled InGaN quantum dots." Light: Science & Applications 3, no. 1 (2014): e139.

113 Jemsson, Tomas, Houssaine Machhadani, K. Fredrik Karlsson, Chih-Wei Hsu, and

Per-Olof Holtz. "Linearly polarized single photon antibunching from a site-controlled InGaN quantum dot." Applied Physics Letters 105, no. 8 (2014): 081901.

114 Bardoux, Richard, Thierry Guillet, B. Gil, P. Lefebvre, T. Bretagnon, T. Taliercio, Sébastien Rousset, and F. Semond. "Polarized emission from GaN/AlN quantum dots: Single-dot spectroscopy and symmetry-based theory." Physical Review B 77, no. 23 (2008): 235315.

115 Winkelnkemper, Momme, Robert Seguin, Sven Rodt, Andrei Schliwa, Lars Reissmann, Andre Strittmatter, Axel Hoffmann, and Dieter Bimberg. "Polarized emission lines from A-and B-type excitonic complexes in single InGaN/GaN quantum dots." Journal of applied physics 101, no. 11 (2007): 113708.

116 Kindel, C., S. Kako, T. Kawano, H. Oishi, Y. Arakawa, G. Hönig, M. Winkelnkemper, A. Schliwa, A. Hoffmann, and D. Bimberg. "Exciton fine-structure splitting in GaN/AlN quantum dots." Physical Review B 81, no. 24 (2010): 241309.

117 Amloy, Supaluck, Y. T. Chen, K. F. Karlsson, K. H. Chen, H. C. Hsu, C. L. Hsiao, L. C. Chen, and Per-Olof Holtz. "Polarization-resolved fine-structure splitting of zero-dimensional In x Ga 1− x N excitons." Physical Review B 83, no. 20 (2011): 201307.

118 Amloy, Supaluck, K. F. Karlsson, T. G. Andersson, and Per-Olof Holtz. "On the polarized emission from exciton complexes in GaN quantum dots." Applied Physics Letters 100, no. 2 (2012): 021901.

119 Kremling, Stefan, Christian Tessarek, Heiko Dartsch, Stephan Figge, Sven Höfling, Lukas Worschech, Carsten Kruse, Detlef Hommel, and Alfred Forchel. "Single photon emission from InGaN/GaN quantum dots up to 50 K." Applied Physics Letters 100, no. 6 (2012): 061115.

120 Lee, Leung Kway, and P-C. Ku. "Fabrication of site-controlled InGaN quantum dots using reactive-ion etching." physica status solidi (c) 9, no. 3-4 (2012): 609-612.

121 C.-H. Teng, L. Zhang, L. Yan, J. Millunchick, H. Deng, and P.-C. Ku, Fundamental limits of InGaN/GaN quantum dot inhomogeneity. Manuscript under preparation.

122 Schlager, John B., Kris A. Bertness, Paul T. Blanchard, Lawrence H. Robins, Alexana Roshko, and Norman A. Sanford. "Steady-state and time-resolved photoluminescence from relaxed and strained GaN nanowires grown by catalyst-free molecular-beam epitaxy." Journal of applied physics 103, no. 12 (2008): 124309.

123 Birner, Stefan, Tobias Zibold, Till Andlauer, Tillmann Kubis, Matthias Sabathil, Alex Trellakis, and Peter Vogl. "Nextnano: general purpose 3-D simulations." Electron Devices, IEEE Transactions on 54, no. 9 (2007): 2137-2142.

124 Rossi, Fausto. Theory of semiconductor quantum devices: microscopic modeling

and simulation strategies. Springer Science & Business Media, 2011.

125 Vurgaftman, I., and J. R. Meyer. "Band parameters for nitrogen-containing semiconductors." Journal of Applied Physics 94, no. 6 (2003): 3675-3696.

126 Vurgaftman, I., J. R. Meyer, and L. R. Ram-Mohan. "Band parameters for III–V compound semiconductors and their alloys." Journal of applied physics 89, no. 11 (2001): 5815-5875.

127 Shan, W., J. J. Song, H. Luo, and J. K. Furdyna. "Determination of the fundamental and split-off band gaps in zinc-blende cdse by photomodulation spectroscopy." Physical Review B 50, no. 11 (1994): 8012.

128 Piprek, Joachim. Semiconductor optoelectronic devices: introduction to physics and simulation. Academic Press, 2003.

129 Lee, S. J., J. O. Kim, S. K. Noh, and K-S. Lee. "Formation and characteristics of self-assembled InGaN/GaN quantum-dot structure grown by using plasma-assisted molecular beam epitaxy." Journal of the Korean Physical Society 51, no. 3 (2007): 1027-1031.

130 Amloy, Supaluck, K. Fredrik Karlsson, Martin O. Eriksson, Justinas Palisaitis, Y. T. Chen, K. H. Chen, H. C. Hsu, C. L. Hsiao, L. C. Chen, and Per-Olof Holtz. "Excitons and biexcitons in InGaN quantum dot like localization centers." Nanotechnology 25, no. 49 (2014): 495702.

131 Zhang, Lei, Chu-Hsiang Teng, Pei Cheng Ku, and Hui Deng. "Electrically driven single-photon emission from site-controlled InGaN/GaN quantum dots." In CLEO: QELS_Fundamental Science, pp. JTh5B-6. Optical Society of America, 2014.

132 Galtrey, Mark J., Rachel A. Oliver, Menno J. Kappers, Colin J. Humphreys, Debbie J. Stokes, Peter H. Clifton, and Alfred Cerezo. "Three-dimensional atom probe studies of an $In_xGa_{1-x}N$/GaN multiple quantum well structure: Assessment of possible indium clustering." *Applied Physics Letters* 90, no. 6 (2007): 1903.

133 Galtrey, M. J., R. A. Oliver, M. J. Kappers, C. J. Humphreys, P. H. Clifton, D. Larson, D. W. Saxey, and A. Cerezo. "Three-dimensional atom probe analysis of green- and blue-emitting $In_xGa_{1-x}N$/ GaN multiple quantum well structures."*Journal of Applied Physics* 104, no. 1 (2008): 013524.

134 Watson-Parris, D., M. J. Godfrey, P. Dawson, R. A. Oliver, M. J. Galtrey, M. J. Kappers, and C. J. Humphreys. "Carrier localization mechanisms in In x Ga 1− x N/GaN quantum wells." *Physical Review B* 83, no. 11 (2011): 115321.

135 Schulz, Stefan, Miguel A. Caro, Conor Coughlan, and Eoin P. O'Reilly. "Atomistic analysis of the impact of alloy and well-width fluctuations on the electronic and optical properties of InGaN/GaN quantum wells." *Physical Review B* 91, no. 3 (2015): 035439.

136 Wu, Yuh-Renn, Ravi Shivaraman, Kuang-Chung Wang, and James S. Speck. "Analyzing the physical properties of InGaN multiple quantum well light emitting diodes from nano scale structure." *Applied Physics Letters* 101, no. 8 (2012): 083505.

137 Yang, Tsung-Jui, Ravi Shivaraman, James S. Speck, and Yuh-Renn Wu. "The influence of random indium alloy fluctuations in indium gallium nitride quantum wells on the device behavior." *Journal of Applied Physics* 116, no. 11 (2014): 113104.

138 Kelly, Thomas F., and Michael K. Miller. "Atom probe tomography." *Review of Scientific Instruments* 78, no. 3 (2007): 031101.

139 Borgström, Magnus T., Valery Zwiller, Elisabeth Müller, and Atac Imamoglu. "Optically bright quantum dots in single nanowires." *Nano letters* 5, no. 7 (2005): 1439-1443.

140 van Weert, M. H. M., N. Akopian, F. Kelkensberg, U. Perinetti, M. P. van Kouwen, J. Gómez Rivas, M. T. Borgström et al. "Polarization Properties of Single Quantum Dots in Nanowires." *arXiv preprint arXiv:0808.2908* (2008).

141 Watanabe, Y., S. Bhunia, S. Fujikawa, T. Kawamura, H. Nakashima, K. Furukawa, and K. Torimitsu. "Heteroepitaxial metalorganic vapor phase epitaxial growth of InP nanowires on GaP (111) B." *Thin solid films* 464 (2004): 248-250.

142 Tchernycheva, M., J. C. Harmand, G. Patriarche, L. Travers, and Ge E. Cirlin. "Temperature conditions for GaAs nanowire formation by Au-assisted molecular beam epitaxy." *Nanotechnology* 17, no. 16 (2006): 4025.

143 Deshpande, Saniya, Junseok Heo, Ayan Das, and Pallab Bhattacharya. "Electrically driven polarized single-photon emission from an InGaN quantum dot in a GaN nanowire." *Nature communications* 4 (2013): 1675.

144 Birner, Stefan, S. Hackenbuchner, M. Sabathil, G. Zandler, J. A. Majewski, T. Andlauer, T. Zibold, R. Morschl, A. Trellakis, and P. Vogl. "Modeling of semiconductor nanostructures with nextnano3." (2006).

145 Rinke, Patrick, Momme Winkelnkemper, Abdallah Qteish, Dieter Bimberg, Jörg Neugebauer, and Matthias Scheffler. "Consistent set of band parameters for the group-III nitrides AlN, GaN, and InN." Physical Review B 77, no. 7 (2008): 075202.

146 Chen, Wei, Guang-Yin Chen, and Yueh-Nan Chen. "Coherent transport of nanowire surface plasmons coupled to quantum dots." Optics express 18, no. 10 (2010): 10360-10368.

147 Gruber, Christian, Andreas Trügler, Andreas Hohenau, Ulrich Hohenester, and Joachim R. Krenn. "Spectral modifications and polarization dependent coupling in tailored assemblies of quantum dots and plasmonic nanowires." Nano letters 13, no. 9 (2013): 4257-4262.

148 Faure, Stéphane, T. Guillet, P. Lefebvre, T. Bretagnon, and B. Gil. "Comparison of strong coupling regimes in bulk GaAs, GaN, and ZnO semiconductor microcavities." Physical Review B 78, no. 23 (2008): 235323.

149 Özgür, Ümit, Daniel Hofstetter, and Hadis Morkoç. "ZnO devices and applications: a review of current status and future prospects." Proceedings of the IEEE 98, no. 7 (2010): 1255-1268.

150 Robinson, James W., James H. Rice, Kwan H. Lee, Jong H. Na, Robert A. Taylor, David G. Hasko, Rachel A. Oliver, Menno J. Kappers, Colin J. Humphreys, and G. Andrew D. Briggs. "Quantum-confined Stark effect in a single InGaN quantum dot under a lateral electric field." Applied Physics Letters 86, no. 21 (2005): 213103.